CRANFIELD UNIVERSITY

LUN MA

AERODYNAMIC ANALYSIS OF LARGE WIND FARMS USING TWO-SCALE COUPLED MODELLING APPROACHES

SATM
EngD in Renewable Energy Marine Structures (REMS)

EngD
Academic Year: 2016 - 2021

Supervisor: Dr Panagiotis Tsoutsanis
Associate Supervisor: Dr Antonis Antoniadis
August 2021

CRANFIELD UNIVERSITY

SATM
EngD In Renewable Energy Marine Structures (REMS)

EngD

Academic Year 2016 - 2021

LUN MA

Aerodynamic Analysis of Large Wind Farms Using Two-scale Coupled Modelling Approaches

Supervisor: Dr Panagiotis Tsoutsanis
Associate Supervisor: Dr Antonis Antoniadis
August 2021

This thesis is submitted in partial fulfilment of the requirements for the degree of EngD

ABSTRACT

The effects of turbine aerodynamics and response characteristics of the atmospheric boundary layer on the overall wind farm efficiency are investigated in this research. Various wind farm modelling strategies, which include a theoretical and several CFD models, are presented. This study consists of three main parts: (i) improve and validate an existing theoretical wind farm model, (ii) infinitely large wind farm modelling with actuator-disc and fully-resolved turbine models, and (iii) finite-size wind farm modelling with a numerical weather prediction model.

In the first part, an extended theoretical model based on a two-scale coupled momentum balance method is proposed to estimate aerodynamic effects of wind turbine towers on the performance of large wind farms. The modified theoretical model predicts that the optimal turbine spacing should increase with the value of normalised support-structure drag, as well as additional parameters describing the response characteristics of the atmospheric boundary layer to the total farm drag. The Detached-Eddy simulations of a periodic array of fully staggered actuator discs (AD) show a reasonably good agreement (within 10% in the prediction of power) with the modified theoretical model.

In the second part, a fully resolved (FR) NREL 5MW turbine model is employed in two URANS simulations (with and without the turbine tower) of a fully developed wind farm boundary layer. The FR-URANS results show stronger tower effects than both AD-RANS and theoretical model predictions, which is a strong indication of the necessity of considering turbine support structure within large wind farm models. The possibility of performing DDES is also investigated with the same FR turbine model and periodic domain setup. The results show complex turbulent flow characteristics within a large wind farm, where typical hairpin and hub vortices have been clearly captured. In addition, the computational cost of DDES has been found to be similar to URANS (for a given number of rotations), which is a positive sign for conducting DDES in future studies.

In the third part, a numerical weather prediction model is used as a realistic farm-scale flow model to investigate how the streamwise pressure gradient, Coriolis force and acceleration/deceleration terms in the farm-scale momentum balance equation tend to change in time. The results suggest that the streamwise pressure gradient may be enhanced substantially by the resistance caused by the wind farm, whereas its influence on the other two terms appears to be relatively minor. These results suggest the importance of modelling the farm-induced pressure gradient accurately for various weather conditions in future studies of large wind farms.

Keywords:

ABL, Actuator disc, CFD, DES, Full-resolved turbine, LES, Numerical weather prediction model, Support structure, Theoretical model, URANS, Wind energy, Wind farm, Wind turbine

ACKNOWLEDGEMENTS

I would like to take this opportunity to express my gratitude to my supervisor Dr Panagiotis Tsoutsanis. For the last two years of my EngD study, he has given me tremendous support and guidance. Especially during the unprecedented and unsettling year of 2020, his has guided me with extreme patience to finish the last bit of journey of my EngD. I would also like to thank my co-supervisor Dr Antonis Antoniadis, who was also my supervisor during the third year of my EngD. He has always been very direct with my mistakes and weaknesses, and that has led to some of the most critical improvement of my research. Prof. Athanasios Kolios who was my co-supervisor during the first and second year of my EngD. He is the one who initiated my interests in academic research, and most importantly he recruited me to become a member of the REMS-CDT family. Without him none of this would not have existed. Dr Takafumi Nishino (西野貴文), my first supervisor of my EngD, my mentor, my role model and a dear friend. He continued to help me all the way until the end, even after he had left Cranfield and no longer had any obligation of a supervisor. The foundation of this research is based on his knowledge and theories. It would not have been possible for me to finish my work without him. I used to tell people that he is the best teacher I have ever had, but now I think this is an understatement. From the bottom of my heart, I am honoured to have him as my first supervisor, and I am sincerely grateful for all of his contributions.

I want to thank my friends and colleagues in the REMS-CDT and, for the countless laughter and unforgettable talks we had together. To my old friends back home in China, who have always been there for me and given me confidence and determinations to go through tough times. Last but not least, to my parents for always having believed in me. I have been studying abroad for 12 years, they have given me the warmest and strongest support one could ever ask for.

TABLE OF CONTENTS

LIST OF FIGURES

LIST OF TABLES

LIST OF EQUATIONS

LIST OF ABBREVIATIONS

ABL	Atmospheric Boundary Layer
AD	Actuator Disk
AL	Actuator Line
BEM	Blade Element Momentum
CFD	Computational Fluid Dynamics
CV	Control Volume
DDES	Delayed Detached-Eddy Simulation
DES	Detached-Eddy Simulation
FR	Fully Resolved
HPC	High-Performance Computing
LES	Large-Eddy Simulation
MEXICO	Model Experiments in Controlled Conditions
NREL	National Renewable Energy Laboratory
NS	Navier-Stokes equations
NWM	Numerical Weather Prediction
RANS	Reynolds-Averaged Navier-Stokes equations
SGS	Sub-Gird Scale
SST	Shear-Stress Transport
TSR	Tip Speed Ratio
URANS	Unsteady Reynolds-Averaged Navier-Stokes equations
WALE	Wall-Adapting Local Eddy-Viscosity
WMLES	Algebraic Wall-Modeled LES model

1 Introduction

1.1 History of Wind Energy

Renewable energy was in fact the only energy form during early civilisation. Fossil fuel only started to be used at large-scale a few centuries ago, not to mention nuclear power was only became available in the 1950s. The earliest use of wind energy was for sail ships; it all started about 5500 years ago in the Mediterranean region. It is believed that the Persians were the first to use windmills in A.D. 500 [1].

Figure 1-1 Sixteenth century windmill for mining [2].

Even though, Netherland is rather famous for their windmills (Figure 1-1), the fact is that the main development of wind turbine for electricity production was performed in the USA in the 19th century. In 1888, the first wind powered generator was built in Ohio (Figure 1-2), with a rated power output of 12kW. The real expansion of wind energy happened after the oil crisis of 1973, when the US government decided that more renewable energy solutions should be developed. There were more than 16000 wind turbines with different sizes installed in California in the 1980s [3].

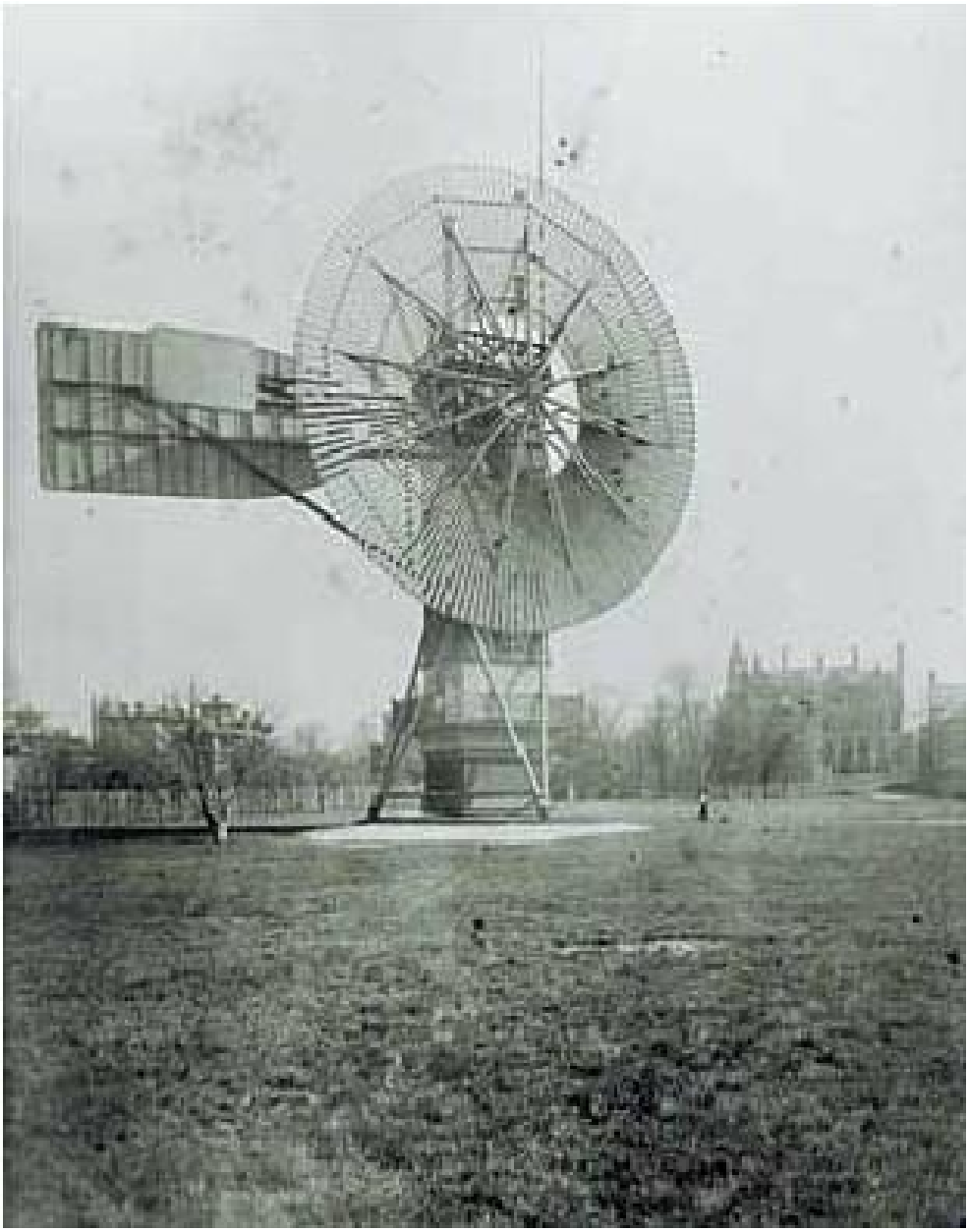

Figure 1-2 First wind turbine, built in 1888 [4].

Later on, the first offshore wind turbine was built in Sweden in 1990. It was located 350m away from the coast, which had a tripod structure foundation and the rated power output was 220kW. Shortly after, the first offshore wind farm, Vindeby, was constructed in Denmark, which contains 11 turbines with rated power output of 5MW combined [5]. These turbines were primarily based on onshore turbine design, they had concrete foundations and only deployed in shallow water. Even though, this small wind farm was far from the industry standard, it proved the feasibility of offshore wind farms and provided valuable knowledge for future projects and studies (Figure 1-3). There are several reasons for the initiation of offshore wind industry. Limited land space for onshore wind farms is a common issue for most of European countries. On the other hand, it is believed that offshore wind farms have relatively smaller general environmental impact, compared to onshore wind farms. In particular, Denmark and the UK have a rather significant public opposition towards onshore wind farms. In addition, government support is another essential factor [6].

Figure 1-3 Vindeby wind farm in Denmark [5]

1.2 Mordent Wind Industry

The development for this technology was rather slow at the beginning, only 2000MW of offshore capacity had been installed up until 2009. However, since then there has been a rapid growth. At this moment, there are 34367MW offshore wind power capacity installed worldwide, 24920MW which is more than 70% of the global value, are installed in Europe [7]. Furthermore, nearly half of

that capacity (10383MW) is installed in the UK, making UK the largest offshore wind energy country in the world [8]. On the other hand, China as one of the new members of offshore wind industry, has the fastest development pace among them. They already have 8990MW of offshore energy capacity by mid-2021 which came second in the world [7].

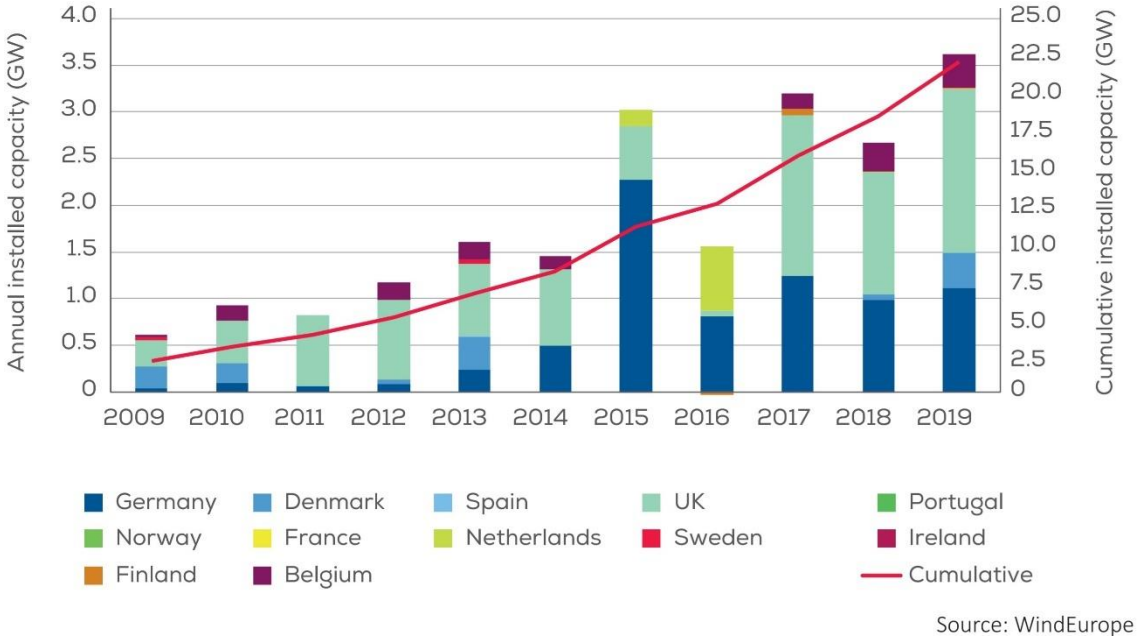

Figure 1-4 Annual and cumulative capacity of offshore wind installations by country (in Europe only) [8].

Inevitably, large wind turbines as well as enormous wind farms are becoming common approaches, in order to cope with the rapid growth of offshore wind developments. The average rated capacity of newly installed wind turbines in 2018 was around 7MW, which nearly doubled the average turbine size in 2014 (Figure 1-5). Most recently, Siemens Gamesa (SG 14-222 DD) [9], General Electric Co. (Haliade-X) [10], Vestas (V236-15.0 MW) [11] and Mingyang Smart Energy (MySE 16.0-242) [12] have all announced their latest large offshore wind turbine development. Currently, the Mingyang Smart Energy is holding the world largest turbine record, with rated capacity of 16MW and rotor diameter of 242m [12]. As shown in Figure 1-6, the offshore wind farm size seems to be increasing even more dramatically than wind turbine size. Most newly announced offshore wind farm plans have rated capacities close to or over one

GWs [7]. The Hornsea projects, as a well-known offshore wind farms in both academia and industry. There are four stages within the Hornsea projects, the total rated capacity is designed up to 6GW, up on full completion the entire wind farm group could contain approximately 750 turbines [13]. The Dogger Bank Wind Farm is another newly developed offshore wind farm project in the UK. The installed capacity is aimed at 3.6GW, and it will primarily use the 14MW version of the Haliade-X turbine developed by General Electric Co. [14].

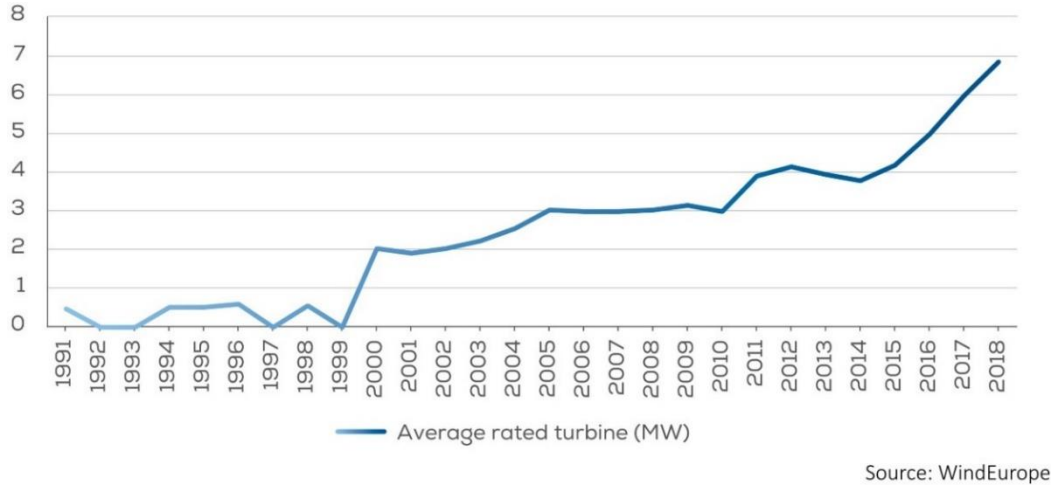

Figure 1-5 Yearly average of newly installed offshore wind turbine size (MW) [8].

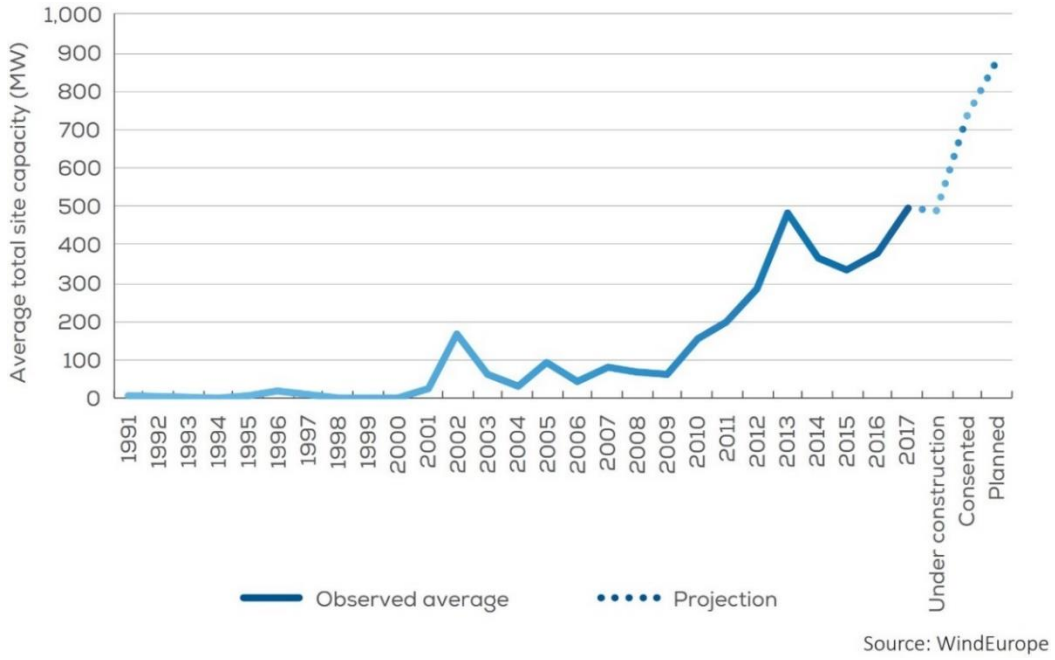

Figure 1-6 Number of turbines and average turbine rated capacities at wind farms under construction in 2019 [15].

1.3 The challenge of Wind Farm efficiency prediction

Since wind farm development is a highly complex and multidisciplinary subject, there are many knowledge gaps that need to be understood, and difficult issues to be solved. Predicting wind farm performance is a key challenge in design optimisation, operation, control as well as grid integration, because of the complex multiscale two-way interactions between turbulent atmospheric boundary layer (ABL) and wind farms. The atmospheric boundary layer is inherently unsteady, that adds complications in the ABL and wind farm interactions. For instance, synoptic-forcing variability and diurnal cycle can cause changes in local pressure gradient and ununiform wind speeds [16]. In addition, the high Reynolds number (in terms of wind farm scale) of the ABL flow and the heterogeneity of terrain or ocean surface conditions (various wave amplitudes and wavelengths), are some of the key factors for the high turbulent and non-stationary nature of the ABL flows [17].

In terms of turbine-scale studies, Betz and Lanchester [18] [19] have made significant research efforts in the field of wind turbine aerodynamics in 1920. Later on, Glauert [20] formulated the blade element momentum (BEM) theory in 1935. Their works have laid the foundation of modern turbine rotor design and modelling strategies; these theories can reasonably predict turbine efficiencies, if the incoming flow is known a priori. On the other hand, due to the unsteady nature of wind flow, predicting the wind turbine and wind farm efficiencies under real life scenarios is still a highly demanding task. Furthermore, the turbulent wake flows inside wind farms create considerable power losses, because of wind speed deficit in the wakes. In addition, large-scale meteorological phenomena are responsible for the flow uncertainty in the free atmosphere. The acceleration/deceleration of wind speed, Coriolis forces and changes of pressure gradients are some of the key deciding factors of the ABL characteristics inside and around wind farms [21]. Modelling the ABL flow and its two-way interaction with wind farms is especially challenging, due to the multi-scale nature of this subject.

It is essential to improve our understanding and prediction of the interaction between ABL flow and wind farms, in order to increase wind farm performance and improve the economic feasibility of wind energy.

1.4 Aim and Objectives of This Research

In this research we attempt to develop a simplified theoretical wind farm model (initially developed by Nishino in 2016 [22]), that is relatively easy and quick to adopt in both academic studies and industry projects. In addition, the effects of turbine support structure and environmental parameters (such as pressure gradient and Coriolis forces) on wind farm efficiency are investigated. We use high fidelity CFD models to validate any modifications to the original theoretical model. The detailed objectives are listed below.

- To improve and validate the two-scale-coupled momentum model by Nishino.

  - Tower effects on wind farm efficiency.
    The wind turbine support structure drag effect is added to the theoretical model, we study the differences of entire wind farm efficiency with and without modelling turbine support structure.

  - Environmental parameters.
    First step is to add basic steady atmospheric parameter (variation of pressure gradient) to the theoretical model. The next step is to include more complex and unsteady atmospheric parameters, which are the wind acceleration/deceleration, Coriolis force and pressure gradient.

- Actuator disc and fully-resolved turbine CFD wind farm modelling.
  We primarily use AD and FR CFD model to confirm and evaluate the turbine tower effect on wind farm efficiencies. The CFD data is analysed in association with the modified theoretical model, in order to validate the theoretical predictions.

- Wind farm modelling with realistic atmospheric boundary layer model (Met Office UM model).

  The UM model is designed for weather prediction by the Met Office of the UK. This model is capable of modelling the realistic ABL at large scale. It is designed as a global ABL flow model, however, in this case we only use a limited-are configuration at N768 resolution (~20km Δx). This is ideal for validating the added environmental parameters to the theoretical model.

1.5 Thesis Contributions

An extended theoretical wind farm model has been developed during this study. This model is based on the two-scale momentum theory, it takes into account the wind turbine support structure effects, which have shown noticeable impact on large wind farm efficiency. High fidelity CFD simulations of fully developed wind farm boundary layer flow have been conducted. The simulations involved fully periodic domain, multiple turbines setup, fully-resolved turbine model and both URANS and (D)DES technics. The CFD results are in good agreement with the modified theoretical model, they capture the phenomenon flow velocity reduction caused by turbine tower, and thus impacting the overall wind farm efficiency. For the first time in wind farm modelling research, we have adopted the state-of-the-art numerical weather prediction model from the UK Met Office. This investigation has demonstrated the mechanisms of wind farm blockage effect by analysing momentum balance in realistic atmospheric flow over an idealised large offshore wind farm. In addition, it has shown the significance of three different terms in the farm-scale momentum balance, namely the streamwise pressure gradient, Coriolis force and acceleration/deceleration terms.

1.6 Publications

Several journal and refereed conference articles have been published during this study. In addition, the analysis in Chapter 4 is in preparation for another journal paper.

List of publications:

- L. Ma and T. Nishino, "Preliminary estimate of the impact of support structures on the aerodynamic performance of very large wind farms," *J. Phys. Conf. Ser.*, vol. 1037, no. 072036, 2018. Peer-reviewed.

- L. Ma, T. Nishino and A. Antoniadis, "Prediction of the impact of support structures on the aerodynamic performance of large wind farms," *J. Renew. Sustain. Energy*, vol. 11, 063306, 2019. Featured article of that month.

- L. Ma, T. D. Dunstan and T. Nishino, “Analysing momentum balance over a large wind farm using a numerical weather prediction model,” *J. Phys. Conf. Ser.*, vol 1618 (6), no. 062010, 2020. Peer-reviewed.

The first two articles are included in Chapter 3 and the last article is in Chapter 5.

2 Literature Review

2.1 Betz' Limit

Lanchester [18] and Betz [19] each defined expressions that connects wind turbine thrust and power coefficients with the axial wind velocity reduction rate. A wind turbine rotor is simplified as an actuator disk in their theories and, a theoretical upper limit of the rotor efficiency is determined. This is more well-known as the "Betz' limit", although, Lanchester's discovery in fact predates Betz' statement [23], this is not a focus point of this study, therefore, "Betz' limit" will be used in the rest of the content.

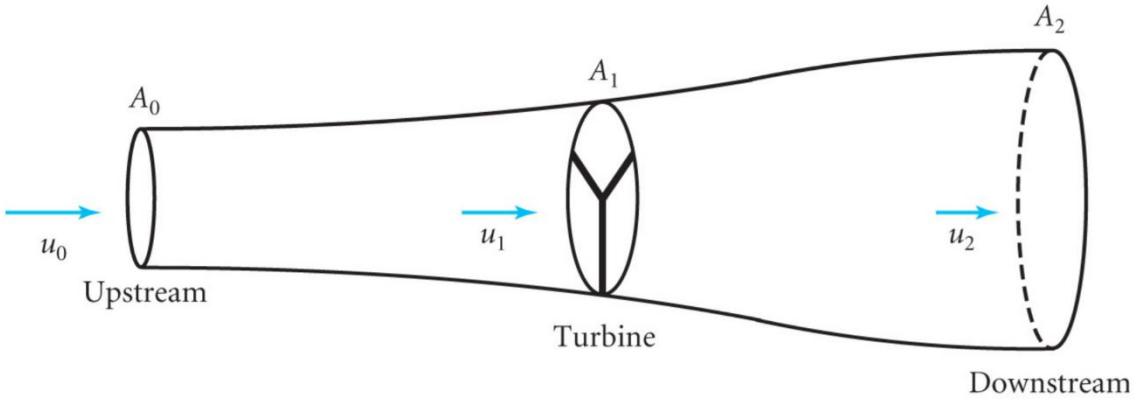

Figure 2-1 Illustration of Betz control volume.

The power output P for a single turbine at a given axial wind speed u can be expressed as:

Equation 2-1

$$P = \frac{1}{2} A \rho u^3$$

where A is the swept area of the turbine rotor and ρ is air density. Wind turbine thrust T is essentially the rate of change of momentum, therefore:

Equation 2-2

$$T = \dot{m}(u_0 - u_2)$$

where $\dot{m}$ is the air mass flow rate through the control volume (Figure 2-1) and u_0 and u_2 are wind velocity upstream and downstream respectively. Furthermore, turbine power P can also be described as:

Equation 2-3

$$P = Tu_1 = \dot{m}(u_0 - u_2)u_1$$

and

Equation 2-4

$$P = \frac{1}{2}\dot{m}(u_0^2 - u_2^2),$$

by combining these two equations above we can obtain:

$$(u_0 - u_2)u_1 = \frac{1}{2}(u_0^2 - u_2^2) = \frac{1}{2}(u_0 - u_2)(u_0 + u_2),$$

hence, $u_1 = \frac{1}{2}(u_0 + u_2)$ and $u_2 = \frac{1}{2}(2u_0 - u_2)$. The main idea of this derivation process is looking for a theoretical limit, under inviscid incompressible condition with perfect mass and momentum conservation, i.e., pressure changes are negligible and density is constant, therefore, $\dot{m} = \rho u_1 A_1$. By substituting the 'new' expression of u_2 and $\dot{m}$ into Equation 2-3 we have $P = 2\rho u_1^2 A_1(u_0 - u_1)$. The induction factor α is a very useful parameter that can be applied to describe the relationship between upstream and downstream wind velocities associated to a wind turbine (or wind farm), in this case $u_1 = (1 - \alpha)u_0$. In addition, the power coefficient C_P is the fraction of power in the wind flow that is extracted by the turbine, based on the expressions above we have:

Equation 2-5

$$C_P = \frac{P}{\frac{1}{2}\rho u_0^3 A_1} = 4\alpha(1 - \alpha)^2$$

The maximum power output is achieved when dC_P/dt equals to zero, this gives $\alpha = 1/3$, therefore, the maximum C_P value of a wind turbine is $16/27$ which is approximately 59.3%, the so called Betz' limit.

2.2 Blockage Effect

Since the nature of the Betz's limit is entirely based on an ideal and entirely isolated environment, there are many assumptions in this theory, which may not be perfectly applicable to real-world scenarios.

In 2007, Garret and Cummins [24] developed a one-dimensional analysis that explored the idea of 'blockage ratio' in a tidal turbine(s) operating environment. They have found that an isolated turbine is more effective in a channel than in an unbounded flow, the power extraction limit (Betz' limit states this is a constant) is proportional to $(1 - A/A_C)^{-2}$, where A_C is the cross-sectional area of the channel. One year later, Antheaume, Maître and Achard [25] performed steady RANS (standard k-ε turbulence model) simulations, and they have also confirmed efficiency increase under various blocked conditions.

In 2012, Nishino and Willden started to investigate this 'blockage effect' using 3D CFD model as well as developing new theoretical models [26] [27].

2.3 Theoretical Wind Farm Models

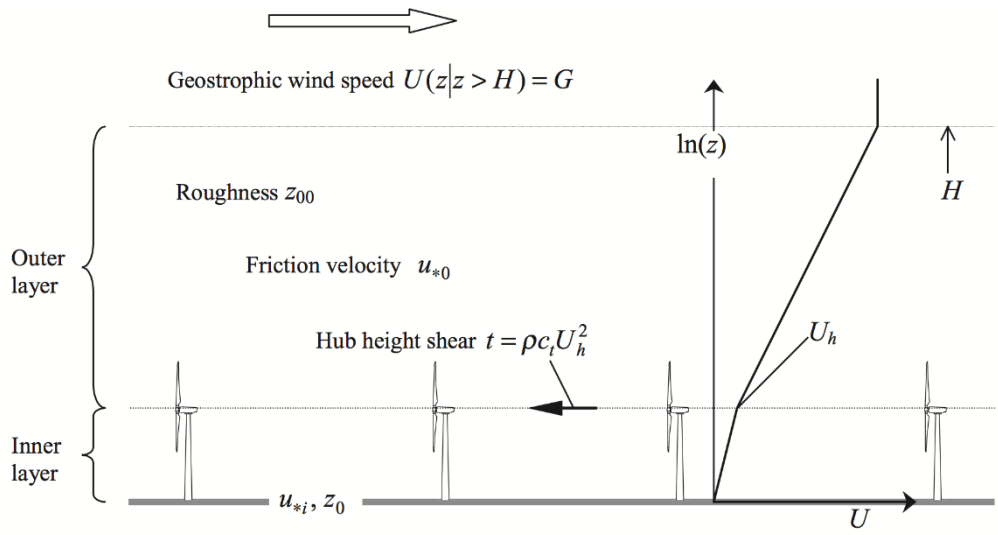

Figure 2-2 Frandsen top-down model [28].

In 1992, Frandsen first introduced a so called 'top-down' model [28]. The overall wind profile had been split into two parts, the outer layer and the inner layer. A constant stress was assumed within each layer. The inflection point was

assumed at the hub height h (Figure 2-2). The characteristic friction velocity is represented as u_{*0} for the outer layer, whereas for the inner layer it is u_{*i}. These constant stresses can also be considered as momentum fluxes; therefore, the difference between them can be explained as momentum loss caused by the turbines. The turbine centre is the hub height, so as the layer inflection point. From this theoretical model, an effective roughness can be deduced, which is $z_{00} = h$. The entire wind farm can be simplified as a rough surface with increased momentum flux and kinetic energy losses. This can be considered as one of the earliest interaction models between wind farm and atmospheric boundary layer (ABL) [28].

An enhanced top-down model was later introduced in 2010 by Calaf et al. [29]. Using detailed large eddy simulation (LES), the existence of the two layers in the vertical direction had been confirmed, for uniform hub height turbines. In addition, the LES results also discovered that due to the significant effect of wake structure created by wind turbines, a specific finite region should be added in order to take this effect into account [29]. Therefore, there are three layers in this new wake-enhanced model, which are the two log-law regions above and below the turbine and the wake layer, based on the horizontal mean velocity distributions. The effective roughness length is $z_{0,hi}$ for this model. In addition, it was able to predict realistic effective roughness length of the large wind farm, comparing with LES results. Optimising wind turbine spacing was also introduced in this study. Pressure gradient and actuator disc were the two main approximations used during this study [29].

Meneveau further improved the theoretical top-down model in 2012 [30]. He combined wind farm entrance effect and internal boundary layer development into the previous model. The new model could then predict the power degradation in wind turbine downstream. The results were compared with actual measured data to validate. Underlying surface roughness was another essential factor, which had been added into the new model. In this way, this model could explore the structure of turbulent boundary layer flow in large wind farms [30].

Most recently, Nishino proposed a new 'two-scale-coupled' momentum model [22]. This model was designed to evaluate a practical efficiency upper limit of a very large wind farm. The atmospheric boundary layer (ABL) was assumed to be driven by a constant pressure gradient and neglecting the Coriolis force, as with Calaf et al. [17]. Then a momentum balance equation can be derived by considering two different ABL's: one is the 'undisturbed' ABL before the wind farm construction, and the other is the 'disturbed' ABL after construction [22]:

Equation 2-6

$$\langle \tau_W \rangle S + T = \tau_{W0} S = const.$$

where S is the constant horizontal area allocated to each wind turbine, $\langle \tau_W \rangle$ is the average shear stress across S, T is single turbine thrust and τ_{W0} is 'natural' shear stress.

The artificial wind farm layer H_F is considered within the overall ABL, where the air flow is strongly affected by the turbines. The assumed height order is $H_T < H_F \ll \delta_{ABL}$, where H_T is turbine hub height and δ_{ABL} is the ABL thickness. The H_F is then defined as the volume-averaged wind speed over the wind farm (U_{F0}), and is equal to the area-averaged wind speed over the swept area of a turbine (U_{T0}). Furthermore, with the effect of wind farm, the new wind speeds are then defined as U_F and U_T, which are not identical this time. Then the local axial induction factor can be defined as $\alpha = U_T/U_F$ and the wind speed ratio $\beta = U_F/U_{F0}$ which indicates the wind velocity reduction from its natural state. In addition, the local and overall thrust and power coefficients can be expressed as:

Equation 2-7

$$C_T^* = \alpha(1-\alpha) \; and \; C_T = \beta^2 \cdot 4a(1-\alpha)$$

Equation 2-8

$$C_P^* = 4\alpha^2(1-\alpha) \; and \; C_P = \beta^3 \cdot 4\alpha^2(1-\alpha)$$

where "*" represents local value, the full equation derivations can be found in the original paper [22]. A simplified wall shear ratio was also presented in this study [22], which is:

Equation 2-9

$$\frac{\langle \tau_W \rangle}{\tau_{W0}} = \beta^{\gamma} = \left(\frac{U_F}{U_{F0}}\right)^{\gamma}$$

The empirical parameter γ describes how ground shear stress varies in relation to the changes of the average wind speed through the farm layer, which is caused by, for example, farm layout modifications. This parameter is assumed close to but less than 2 in Nishino's model. This is based on the assumption that the 'effective' friction coefficient ($C_f^* = \tau_W / \frac{1}{2}\rho U_F^2$) would not change significantly, however, may somewhat increase (turbines tend to increase the turbulence intensity within the wind farm) from the natural fiction coefficient ($C_{f0} = \tau_{W0} / \frac{1}{2}\rho U_{F0}^2$). Since $\beta = U_F / U_{F0} \leq 1$, $\gamma \leq 2$ is required to satisfy $C_f^* \geq C_{f0}$. By introducing γ, α and β can be described in this following momentum conservation equation:

Equation 2-10

$$1 - \beta^{\gamma} = \Lambda \cdot \frac{1}{C_{f0}} \cdot \beta^2 \cdot 4\alpha(1 - \alpha)$$

where Λ is area ratio A/S (A is swept area of a turbine).

2.4 CFD Wind Farm Modelling

2.4.1 Navier–Stokes equations

The viscous fluid motion was first described by Sir Isaac Newton in 1687 [31], where he investigated the dynamic behaviour of fluids under constant viscosity. The Euler's inviscid equations were later derived by Bernoulli (1738) and Euler (1755) [32]. During late 1820s, there were studies for exploring the mathematical model of fluid flow by Claude-Louis Navier (1827), Augustin-Louis Cauchy (1828), Siméon Denis Poisson (1829), and Adhémar St.Venant (1843),

however, the viscous force of fluid was mostly overlooked [32]. Until 1845, Sir George Stoke derived the final form of the famous Navier-Stokes (NS) Equations, which included the Newtonian viscous terms [32] [33].

In this research we only focus on unsteady, three-dimensional, incompressible viscous flow. Compressible flow might be more appropriate for high-speed flow around turbine blade tip under certain conditions, however, we primarily focus on the large-scale flow properties of the entire wind farm in this study, rather than detailed turbine scale (or even blade scale) flow.

The Navier-Stokes equations consist of three fundamental physical principles, which are conservation of mass (continuity), conservation of momentum (Newton's Second Law) and conservation of energy [34]. Since thermo activity is not considered in this study, the energy equations are not discussed here.

Mass conservation equation:

Equation 2-11

$$\frac{\partial u_i}{\partial x_i} = 0$$

where u is velocity.

Momentum conservation equation:

Equation 2-12

$$\frac{\partial u_i}{\partial t} + \frac{\partial u_i u_j}{\partial x_i} = F_i - \frac{1}{\rho}\frac{\partial p}{\partial x_i} + \frac{\partial}{\partial x_j}\left(\upsilon \frac{\partial u_i}{\partial x_i}\right)$$

where p is statice pressure, ρ is density and υ is kinematic viscosity ($\upsilon = \mu/\rho$, μ is dynamic viscosity) and F_i represents external forces introduced to the equations.

2.4.2 Reynolds Averaged Navier-Stokes equations

From a pure mathematical point of view, by coupling these non-linear partial differential equations, it is possible to solve and describe any incompressible flow. Although, to numerically solve the Navier-Stokes equations (also known as

Directly Numerical Simulations (DNS)), where the entire range of spatial and temporal scales of the turbulence are resolved, is still a daunting task for complex flow conditions. Osborne Reynolds (1895) [35] developed a new set of equations, the fundamental idea was to define any scalar instantaneous quantity (such as pressure and velocity) as the sum of its time-averaged mean and fluctuations. Therefore, they are known as Reynolds-Averaged Navier-Stokes (RANS) equations. Using velocity as an example:

Equation 2-13

$$u_i = \overline{u_i} + u_i'$$

where the $\overline{u_i}$ is the time-averaged component and u_i' is the fluctuating component. The final form of the RANS equations is (full derivation can be found in [36]):

Equation 2-14

$$\frac{\partial \overline{u_i}}{\partial x_i} = 0$$

and

$$\frac{\partial \overline{u_i}}{\partial t} + \frac{\partial \overline{u_i u_j}}{\partial x_i} = \overline{F_i} - \frac{1}{\rho}\frac{\partial \overline{p}}{\partial x_i} + \frac{\partial}{\partial x_j}\left(\upsilon \frac{\partial \overline{u_i}}{\partial x_i} - \overline{u_i' u_j'}\right)$$

Even though, the RANS equations have given us a new approach to solve the original NS equations, they have also created new unknowns ($\overline{u_i' u_j'}$ is known as the Reynolds-stress) in the problem. In addition, there is no additional equation for solving the added Reynolds-stress term. In order to tackle this problem, various turbulence models have been proposed, a few of them, that are related to this research, are discussed below.

2.4.3 One-equation turbulence model

The Spalart-Allmaras (S-A) model was proposed by Spalart and Allmaras in 1992 [37], which is a one-equation turbulence model that solves a modelled transport equation for the kinematic eddy turbulent viscosity. This is essentially

a low Reynolds number model, that originally designed for aerodynamic applications [37] [38]. This model can generate satisfactory results for a wide range of engineering applications, especially for aerofoil and turbine blade models [38]. The S-A model is often used to obtain initial solutions for more complex models (two-equation models for instance); even though, it is also applicable as the main turbulence model in engineering studies. Mittal et al. carried out a wind energy study that involved blade resolved CFD simulations in 2016 [39]. They showed detailed comparison between different turbulence models, the CFD results were also validated by wind tunnel test data. Their results show good agreement for the wake profile between S-A model and a two-equation model ($k-\omega$ SST). In addition, the S-A model predicted similar turbine thus and power coefficients to other models as well as experimental data.

2.4.4 Two-equation turbulence models

Two-equation models were in fact developed prior to the relatively simpler one-equation model. The $k-\omega$ and $k-\varepsilon$ models are perhaps two of the most popular two-equation turbulence models in engineering applications. Launder and Spalding in 1972 [40] [41] developed the standard $k-\varepsilon$ model, which solves two transport equations for the turbulence kinetic energy (k) and its dissipation rate (ε). On the other hand, the standard $k-\omega$ model was initially formulated by Wilcox in 1988 [42], similar to the $k-\varepsilon$ model it also solves two transport equations, one for turbulence kinetic energy (k) and the other is for specific dissipation rate (ω). This model was then improved by Wilcox in 2006 [38] [43], in terms of low-Reynolds number effects, compressibility, and shear flow spreading, this version is currently adopted in modern CFD software [44].

There are a few different versions of each of these two turbulence models, three of them are involved in this study, which are the standard $k-\varepsilon$, the $k-\varepsilon$ Realisable and the $k-\omega$ SST (Shear-Stress Transport) models.

The $k-\varepsilon$ Realisable model was the work of Shi et al. in 1995 [45]. The idea was to improve the standard version with flow conditions such as strong

adverse pressure gradients, streamwise curvature, separation and recirculation zones. The two key differences are:

- The modified version uses an alternative formulation for the turbulent viscosity.
- The turbulent kinetic energy dissipation rate (ε) is modified, which is based on the dynamic equation of the mean-square vorticity fluctuation [44].

The $k-\omega$ SST was proposed by Menter in 1993 initially [46] [47], to improve the strong sensitivity of free-stream conditions issue from the standard model. This modified version differs from the standard one in two key points:

- It combines both the standard $k-\omega$ and $k-\varepsilon$ models, the near-wall region is modelled by standard $k-\omega$ and the free-stream is covered by the standard $k-\varepsilon$. This method was also used in the Baseline (BSL) $k-\omega$ model [47].
- It takes into account the transport of the turbulence shear stress in the definition of the turbulent viscosity [44].

These additional features allow the $k-\omega$ SST model to deliver relatively more accurate predictions and can be applied to a wider range of flow conditions, such as adverse pressure gradient flows and aerofoils [44] [47]. Even though, certain disadvantages of the $k-\omega$ SST model should also be pointed out here. For instance, this model tents to produce large turbulence levels in places with large normal strains or strong acceleration [48] [49], whereas this tendency is less significant with the $k-\varepsilon$ model.

Since we chose $k-\omega$ SST turbulence model for the majority of the URANS cases in this study (turbulence model analysis is demonstrated in later chapters), previous wind energy studies that also utilise the $k-\omega$ SST model are disused below.

In 1998, Sørensen and Hansen [50] were the first study group who applied blade resolved modelling approach for wind turbine research. They utilised an incompressible Reynolds Averaged Navier-Stokes (RANS) solver, where the

boundary layer turbulence was modelled by $k-\omega$ SST model. A single blade and a three-blade turbine (NKT 500/41 wind turbine) had been modelled in their study, both using rotating reference frame method. The results were promising when the wind speed was below 10m/s, however, as the wind speed increased the model started to underpredict the power output. In addition, the flow separation around the blade was also not captured accurately. The author stated the main issues were the lack of mesh refinement and limitation of the turbulence model. Although, considering the low computational power at that time and more recent works, it is believed that the crucial problem is the mesh resolution, whereas the $k-\omega$ SST has been proved as one of the most popular turbulence models for similar studies. Therefore, appropriate meshing strategy is essential in order to generate accurate results.

Dose et al. [51] performed a fluid-structure modelling study using the NREL 5MW wind turbine in 2018. Even though, the structure properties of the turbine are not within the scope of this current project, the fluid dynamic part of their study is still highly useful. Their model contained an isolated wind turbine rotor (no support structure in this case), siting within a large far field domain (H: $10D$, W: $10D$ and D: $30D$, where D=126m). They used OpenFOAM to perform the fluid dynamic calculation, that solved the incompressible Unsteady RANS (URANS) equations, the choice of turbulence model was also $k-\omega$ SST, and the sliding mesh method was adopted for the rotating motion. The time step setting was $\Delta t = 0.01s$, which was approximately 0.5° of rotation angle each time step. Moreover, after a grid dependency study, their choice of fully structured mesh resolution was 36.38×10^6 number of cells in total, where the rotor section had 7.23×10^6 number of cells. On the whole, their results had shown reasonable agreement with the original estimation [52]. This proves with sufficient mesh resolution the $k-\omega$ SST turbulence model is suitable for this type of research.

2.4.5 LES

One thing should be pointed out here is that RANS models that based on the Boussinesq approximation [53] [54] are often referred as isotropic RANS

models, such as the aforementioned S-A, $k-\omega$ and $k-\varepsilon$ models. The Boussinesq approximation essentially describes the eddy viscosity concept, that assumes the anisotropic part of the Reynolds stress tensor is linearly proportional to the time-averaged strain rate tensor [55]. This is one of the key limitations of the RANS models.

As we have mentioned earlier, with current computing technology it is still not possible to directly resolve the entire spectrum of turbulent scales (DNS). Turbulent flows can be characterised by eddies of different length and time scales. According to Kolmogorov's (1941) theory, the largest eddies are typically comparable in size to the characteristic length of the mean flow, on the other hand, the smallest ones are responsible for turbulence kinetic energy dissipation [56] [57]. An alternative solution called Large-Eddy Simulation (LES) was proposed initially by Smagorinsky in 1963 [58]. Unlike RANS (or URANS) that uses time-averaging technics and additional turbulence models, large eddies (or large-scale motions of turbulent flow) are numerically resolved in LES, only small (sub-grid scale (SGS)) eddies are modelled (this is also known as filtering). Large eddies carry most of the turbulent energy and represent the majority of the momentum transfer and turbulent mixing [57], and LES is able to capture large eddies in full details directly. Moreover, small eddies are considered to be more isotropic and homogeneous than large ones (tend to be anisotropic) [57], therefore, it would be easier and relatively more accurate to model the SGS motions only, compared to using a single turbulence model to capture all scales. There are several SGS models exist and wildly adopted in modern CFD software [44], for instance the Smagorinsky-Lilly model [58], Wall-Adapting Local Eddy-Viscosity (WALE) model [59] and the Algebraic Wall-Modeled LES model (WMLES) [60].

2.4.6 DES

Even though, LES is already much less computationally intensive than DNS, it is still too expensive for complex academic projects and industrial simulations. Therefore, it is necessary to find another approach to further reduce computational power requirements while maintaining reasonably high accuracy.

Spalart et al. first introduced the idea of 'Detached-Eddy Simulations' (DES) in 1997 [61], which basically is a hybrid simulation strategy that combines the one equation Spalart-Allmaras turbulence model with Large-Eddy simulations. The main motivation was to reduce the cost of LES and remove the grid dependence of LES in some regions. This strategy offers unsteady RANS in the thin boundary layer region and LES after massive separation. The eddies that are internal to the boundary layer are considered as 'attached eddies', which will be modelled, whereas the 'detached eddies' are resolved. In addition, since it is URANS that covers the near-wall region essentially, it is possible to replace the S-A model with more complex models, such as $k-\varepsilon$ Realisable and the $k-\omega$ SST [44].

Moreover, the original DES can encounter an incorrect behaviour in thick boundary layers and shallow separation regions. The resulted phenomenon is that LES will not replace the URANS model after the supposed separation, which means the entire domain is then undergoing URANS simulation. Therefore, a new 'Delayed DES' (DDES) was proposed by Spalart in 2006 [62]. By re-defining the DES length scale $\tilde{d}$, it is now not only depending on the grid, but also the eddy-viscosity field [44].

2.4.7 Turbine modelling

In this study, we utilise both actuator disc and fully resolved methods to model wind turbine for CFD simulations. Two additional approaches (BEM and vortex model) are also listed here, in order to have a better understanding of different mechanisms of turbine modelling strategies. Specific previous study examples for using actuator disc and fully resolved models are included in the corresponding chapters.

2.4.7.1 Actuator disc (Porous media)

The actuator disc concept is essentially based on the traditional momentum theory, which was initially introduced by Rankine in 1865 [63] and further improved by Froude in 1889 [64]. This method considers the aerodynamic behaviour of wind turbines without any specific turbine design, only taking into

account the energy extraction process (Figure 2-3) [65]. The momentum theory itself is rather simple, when air passes through the disc undergoes an overall change in velocity due to pressure difference, therefore the rate of change of momentum equal to the mass flow rate times change of velocity.

Even though, actuator disc is not the most up to date neither the most sophisticated method, it is still largely applied on many complex research due to its low computational cost. Joukowsky (1918) adopted this method to predict the performance of a hovering helicopter rotor [66]. The Betz' limit (1920), that discussed earlier in this chapter, was based on the classic actuator disc theory [19]. The generalised actuator disc model was first applied to wind turbine by Sørensen in 1992, using finite difference method [67].

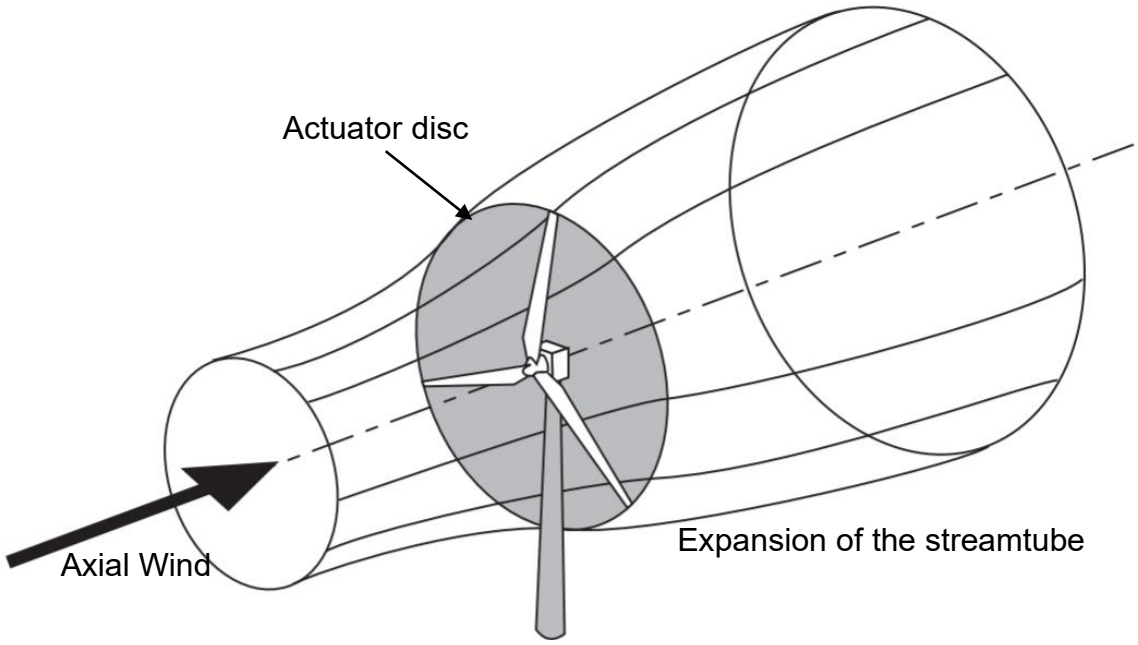

Figure 2-3 Simple illustration of actuator disc theory [65].

The AD turbine modelling approach can be implemented as the 'porous-jump' boundary condition in FLUENT [44]. This thin porous medium has a finite thickness over which the pressure change is defined by coupling Darcy's Law and additional inertial loss term [44]:

Equation 2-15

$$\Delta p = -\left(\frac{\mu}{\alpha} v + K \frac{1}{2} \rho v^2\right) \Delta m$$

where α is the permeability of the medium, K is the pressure-jump coefficient and Δm is the thickness of the medium. In this research we only manipulate the pressure-jump coefficient in order to model different turbine thrust values, the permeability of the medium is left as default value ($1 \times 10^{10} m^2$) and the medium thickness is always 1m.

2.4.7.2 Blade element momentum theory (Actuator line)

In 1978 R. T. Griffiths and M. G. Woollard performed a design and optimisation process using Blade Element Momentum Theory (BEMT). They were able to successfully carry out a computer analysis, which was made of the aerodynamic performance of a wind turbine designed to give maximum power coefficient at a tip speed ratio of 5. However, there was no sufficient experimental data for suitable aerofoil sections over a wide range of incidence and Reynolds number, and the BEMT is in fact based on many assumptions. Even though, they still managed to obtain information on the nature of the flow, the power, torque and thrust developed and the effects of varying the pitch angle of the blades [68].

Initially the use of blade element momentum theory was mainly for marine and aviation propellers but was later applied to wind turbines. It is mostly applied for analysing the aerodynamic or hydrodynamic performance of wind or tidal turbines [69]. BEMT is a combination of three separate theories, which are one-dimensional momentum theory, rotational momentum and blade element theory. Steady loads on a turbine blade can be calculated based on BEMT using a stream tube model. Then the thrust and power of the rotor for different flow velocities, rotational speeds and pitch angle can be calculated. In addition, chord and pitch angle distributions along the span of the blade for a given set of input parameters can also be defined and optimised. This method has been developed from single streamtube model to multiple stream tube model, and the latest double multiple streamtube model (DMST) [70].

The multiple streamtube model was first developed by J. Strickland in 1974, which represents the steady loads on a turbine blade using multiple streamtube instead of single one [70]. Moreover, in 1988 I. Paraschivoiu proposed an analytical modelling method, which is the double multiple stream tube method. The model presented has two major advantages. First of all, it requires much less computing power than three-dimensional vortex model. Secondly, it can predict aerodynamic blade loads more accurately than multiple-stream tube models [71].

In DMST method, modelling the flow through the rotor is achieved by analysing the flow through several stream tubes. Moreover, assuming the hydrodynamic forces on the turbine rotor is equal to the rate of change in momentum through the rotor, the flow disturbance produced by the rotor can be determined. One of the advantages of DMST model is that it is able to rather accurately evaluate the local value of the velocity at the instantaneous blade load, by investigating the interference between the wake of downwind blade and the upwind blade. Velocities differ in both the upstream and downstream regions of the stream tube in this model, different stream tube also has various velocities. Series of elementary stream tubes are used to model the turbine rotor in DMST, and two actuator discs are used to model each stream tube (Figure 2-4). The pressure will drop once crossing the actuator disc, and this is corresponding to the stream wise force divided by the area of the actuator disc [72].

During a recent study, Dr Andrew Shires at Cranfield university developed an aerodynamic performance modelling tool specifically for a novel V-shaped vertical axis wind turbine (VAWT), which based on double multiple streamtube method. Three-dimensional consideration for tip lift losses, induced and junction drag and tower losses are all included in this tool. Experimental data was measured form five medium to large conventional vertical axis wind turbines, and compared with the analytical results from the tool, good agreement was shown. However, the dynamic stall model in this tool still require further modification, regarding to neglect dynamic flow effects for negative pitch rates [73].

Even though, the series of methods, which use streamtube concept, can be imprecise due to rough estimate wake effects or complex three-dimensional flows. Furthermore, BEMT does not take into account secondary effects from three-dimensional flows such as tip vortices and radial flow induced by the rotation of the blade system. Nevertheless, this method is still used today due to its lesser computational requirements, often applied together with computational fluid dynamic method. [74] [75].

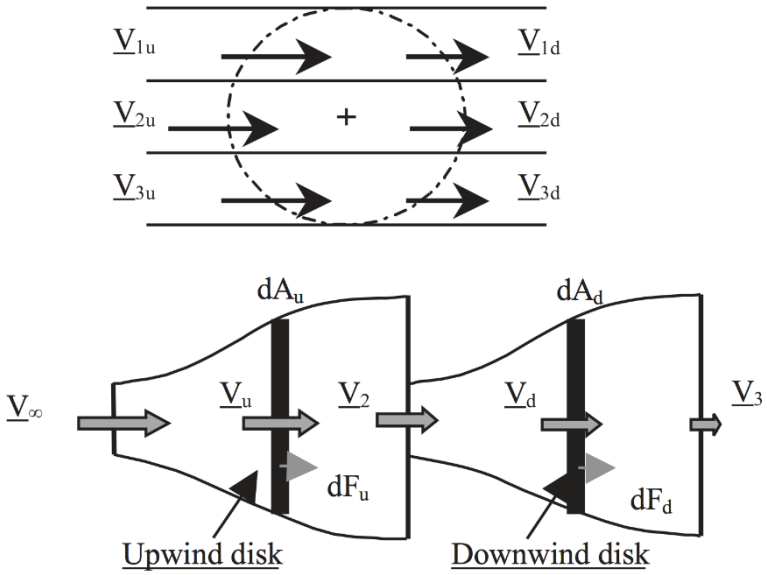

Figure 2-4 Double multiple stream tube model [72].

2.4.7.3 Vortex model

In 1987, D. Vandenberghe and E. Dick modelled a straight blade vertical axis wind turbine using a free vortex model. They were able to show close agreement between experimental and numerical results, by modelling both wake and dynamic stall effects. Furthermore, the multi grid technique was applied in order to reduce computing time to be acceptable at that time, which made the FVT simulation technique could be used for parametric optimisation of vertical axis wind turbines and, particularly, for the optimisation of the pitch control [76].

The free vortex model is especially useful for modelling vertical axis turbines. A bound vortex filament named lifting line, which the strength will change as a

function of azimuthal position, is used to replace the aerofoil blade. To simplify the two dimensional vortex, a single bound vortex is used to represent the aerofoil. In addition, the flow field is modelled by a single bound vortex, which is adequate enough at distances greater than approximately one chord length from the aerofoil (Figure 2-5).

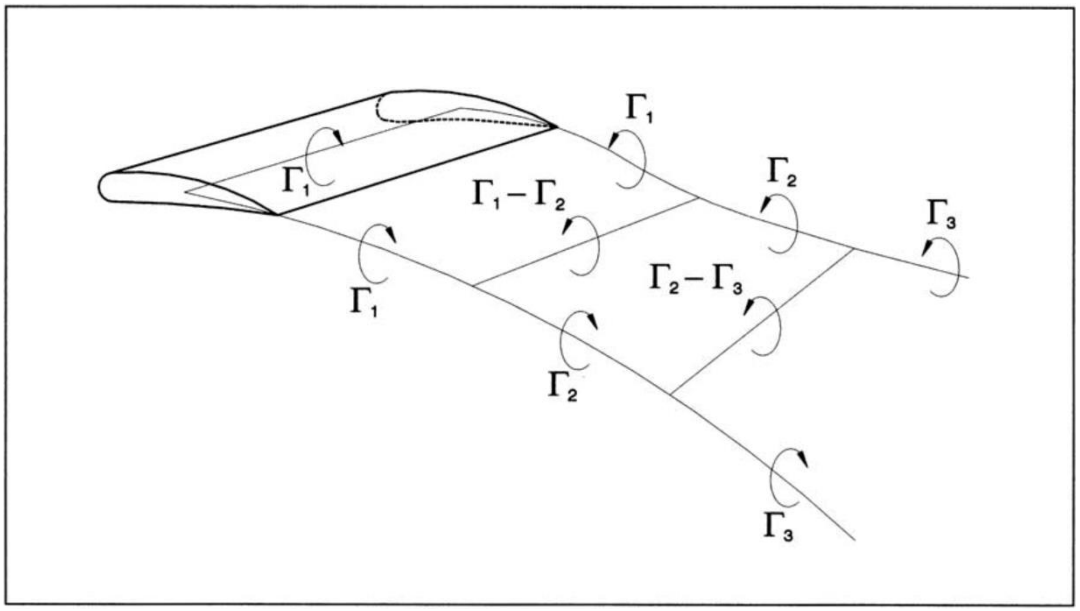

Figure 2-5 Vortex structure for a blade element [76].

The vortices were shed on span wise and, their strengths are equal to the change in the bound vortex strength, this is due to bound vortex variation. Therefore, a discrete set of free vortex filaments shed from each blade end are used to model wakes.

Three-dimensional analysis may be applied on a curve-bladed rotor. In this case, the blade is divided into number of segments along the span. Each blade element is represented by a straight bound vortex line. During this modelling process, the elemental vortex line is assumed to remain straight, and the end of the line is convected at its respective local fluid velocities. Consequently, the elemental vortex line can be stretched, translated and rotated as a function of time. As a result of the Helmholtz theorem of vortices, a trailing vortex is shed at the end of each blade element. Therefore, a quadrilateral mesh vortex system is shed, with concentrated vortices of equal strength along each side. During any given time period, span wise and trailing vortices can be related to the change

in bound vortices, with respect to time and position along the blade. Biot-Savart law is used to calculate the velocity induced at any point by each finite length vortex line in three-dimensions [77].

A computational code called CACTUS (Code for Axial and Cross-flow Turbine Simulation) was developed by J. C. Murray and M. Barone. This code is capable to calculate the blade aerodynamic (hydrodynamic) forces, detailed wake vortex trajectories and turbine performance. The code validation procedure was carried out by comparing the measured data from three different type and scale VAWT with the analytical results from CACTUS. Promising agreement was shown in all three cases [78].

2.4.7.4 Fully resolved

The fully resolved approach is perhaps the most straightforward to understand, among all the turbine modelling methods, since there is no complex numerical estimation involved, however, it is also the most demanding turbine modelling strategy. The entire turbine 3D geometry is modelled in detail with this approach. All aerodynamic properties of the turbine are directly presented in the model, therefore, the fully resolved turbine model is highly accurate and realistic.

On the other hand, this method requires extra attention when building the 3D CAD model and the associated mesh. Rigorous CFD simulations need precise 3D turbine model and high mesh quality, otherwise the results could be inaccurate or even invalid. In addition, the mesh size (in terms of number of element) of fully resolved turbine model is generally much larger than AD and BEM models, therefore, it is considerably more computationally expensive to run this type of simulations [79] [80] [81].

3 Tower Effect with Actuator Disc Approach

3.1 Introduction

Wind farm development is one of the most challenging multidisciplinary businesses today; nevertheless, wind energy industry is rapidly expanding with no sign of stopping [8] [17]. Due to the advantage of vast open sea, unconventionally large offshore wind farms are currently under construction. The well-known Hornsea offshore wind projects, for instance, plan to install more than 300 large multi-megawatt wind turbines across a total area of 869 km^2 [82]. It seems clear that the size of future offshore wind farm is going to be enormous. Not only the size of the wind farm is increasingly large, but also the size of the industrial wind turbines. The rotor diameter of the latest wind turbines varies between 160 and 200m. In order to be able to support these gigantic rotors in the harsh offshore environment, the support structures are also becoming extra-large and strong. The majority of existing wind farms employ monopiles for the support structures; therefore, we consider the effects of such support structures in this study.

3.1.1 Previous studies

There are several studies about wind turbine support structures, in terms of structural integrity, manufacturing, transport and some others; however, the effects of support structures on wind farm's aerodynamic performance have been less investigated to date. Due to the complexity of modelling, support structures are often excluded in farm-scale Computational Fluid Dynamics (CFD) studies [83] [84]. For example, recent large-eddy simulation (LES) studies performed by Chatterjee and Peet [85] and Zhang et al. [86] both look into the potentials of 'vertically staggered' wind farms but without modelling turbine support structures. On the other hand, single turbine researches often consider modelling the entire wind turbine including the support structure. For example, Wu and Porté-Agel [87] have carefully implemented and investigated the support structure aerodynamic effects in both wind tunnel tests and LES, where the wake of the tower has been clearly seen. On the other hand, the support structure effect has already been recognised in the tidal energy

industry. Mason-Jones et al. [88] have particularly studied the influence of the support structure on a single tidal stream turbine performance. Furthermore, there are also tidal farm studies [89] [90] [91] which have specifically described the overall farm efficiency impact from support structures.

The existing well-known theoretical large wind farm models [92] [29] [30], however, have not included the impact of support structures explicitly. This study, which is an extension of an earlier conference paper by the authors [93], investigates the effect of support structures on the aerodynamic performance of large wind farms using the theoretical two-scale momentum model of Nishino [22] (see also Nishino and Hunter [94]). This model combines a farm-scale momentum balance equation with the classic actuator disc theory, thereby predicting the power of an ideal large wind farm in a simple quasi-1D manner. Instead of modelling the wind profile explicitly, the Nishino model focuses on the change of the average wind velocity across the wind farm. This quasi-1D approach is a reasonable and robust approach when considering real 'complex' (non-logarithmic) background wind profiles that may be caused due to various meteorological reasons [95]. The original Nishino model has been shown to agree reasonably well with several different types of numerical simulations of a periodic actuator disc array [95] [96] [97] [98]. The model was originally only for an ideal, infinitely large wind farm, but has recently been extended for a large finite-size wind farm as well [21]. Therefore, in this study, we further extend this quasi-1D model by taking into account the aerodynamic impact of turbine support structures (towers). Using the extended model we investigate how the support-structure drag may affect the optimal design of future large wind farms. In addition, a series of CFD simulations are conducted to validate this extended theoretical model.

3.2 Theoretical Model Modifications

The original two-scale momentum model [22] (see [94] for a full description of the model) has been designed to predict the performance of ideal 'infinitely large' wind farms. A constant streamwise pressure gradient is assumed as the only driving force of the atmospheric boundary layer (ABL). Two different steady

ABLs are compared to each other: one is the ‘unperturbed’ or ‘natural’ ABL observed before farm construction, and the other is the ‘perturbed’ ABL observed after farm construction; thereby a farm-scale momentum balance equation is derived. The new modification proposed in this study is to add the drag force due to turbine support structures, *D*, into the momentum balance equation as follows:

Equation 3-1

$$\langle \tau_w \rangle S + T + D = \tau_{w0} S$$

where $\langle \tau_w \rangle$ is the bottom shear stress (wind-induced shear stress on the land or sea surface, depending on whether the farm is onshore or offshore) averaged across the area *S*, which is the average land/sea surface area per each turbine, *T* is the thrust on each rotor, *D* is the drag due to its support structure (tower) and τ_{w0} is the ‘natural’ bottom shear stress, i.e. the shear stress on the land/sea surface at the construction site before constructing the farm. The rotor thrust T and tower drag D are then represented using ‘local’ thrust and drag coefficients C_T^* and C_D^* (i.e. based on a locally-averaged wind speed) as

Equation 3-2

$$\langle \tau_w \rangle S + T + D = \tau_{w0} S$$

Equation 3-3

$$D = \frac{1}{2} \rho U_F^2 A_s \cdot C_D^*$$

where ρ is air density, A and A_S are the rotor swept area and support-structure frontal projected area, respectively, and U_F is the average wind speed across the wind farm layer introduced in [22]. This layer is typically two to three times as high as the turbine hub height; see [94] for further details.

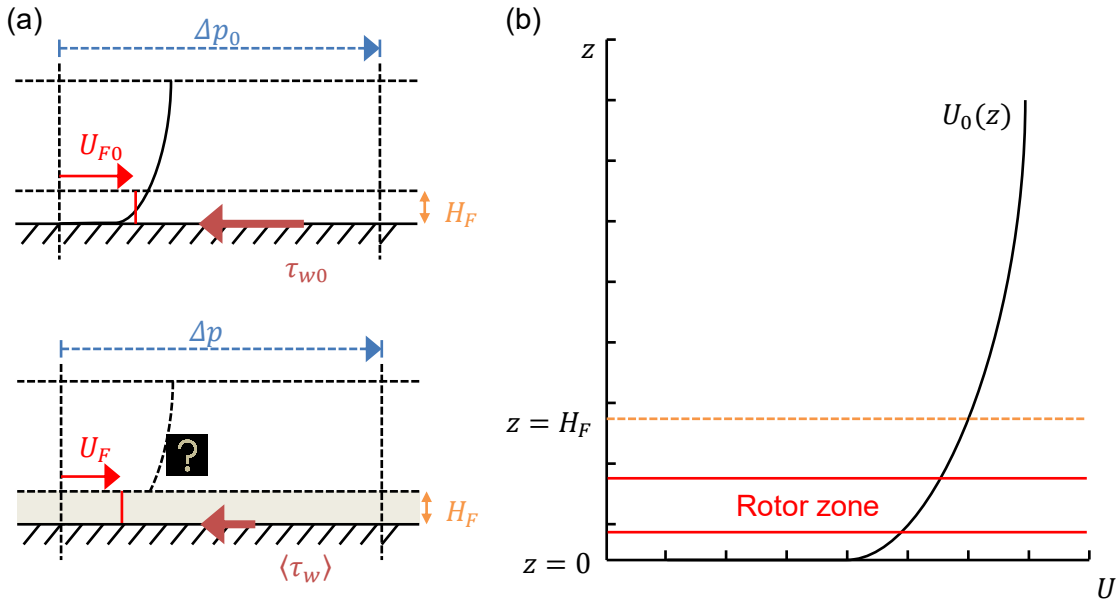

Figure 3-1 Schematic of the two-scale momentum model: (a) fully developed boundary layer before and after farm construction, (b) nominal farm-layer height, H_F (the rotor zone position regarding to the ground is not representative to any real wind farm design). Reproduced from [22] with minor modifications.

Figure 3-1 shows a schematic of the flow scenarios considered in the theoretical model, reproduced (with minor modifications) from [22]. It should be noted that, for the case of an infinitely large wind farm, the driving force observed after farm construction, Δp, is assumed equal to that observed before farm construction, Δp_0 (based on the assumption that the size of the atmospheric system creating a pressure gradient is also infinitely large), yielding the simple momentum balance Equation 3-1 given earlier. For the case of a large finite-size wind farm to be discussed in the next subsection, this assumption will be removed.

Following the original two-scale momentum model [22], C_T^* is modelled using the classical actuator disc theory. This may appear to be a strong simplification but tends to yield a good agreement with 3D numerical simulations of a fully staggered array of actuator discs with a wide range of inter-turbine spacing from $6d \times 6d$ to $14d \times 14d$ [96] [97], where d is the rotor diameter. Note, however, that this simple representation of C_T^* may need to be replaced by a more advanced model, such as the one proposed recently in [99] if an even smaller

turbine spacing is of interest. Eventually, the momentum balance Equation 3-1 is transformed into the following non-dimensional form:

Equation 3-4

$$\left(4\alpha(1-\alpha)+\frac{A_s}{A}C_D^*\right)\frac{\Lambda}{C_{f0}}\beta^2+\beta^\gamma-1=0$$

where $\alpha = U_T/U_F$ (U_T is the average wind speed across A), $\beta = U_F/U_{F0}$ (U_{F0} is the natural farm-layer wind speed observed before farm construction), $\Lambda = A/S$ is the farm density, $C_{f0} = \tau_{w0}/\frac{1}{2}\rho U_{F0}^2$ is a natural friction coefficient and $\gamma = \log_\beta\left(\frac{\langle\tau_w\rangle}{\tau_{w0}}\right)$ is an empirical parameter to model the wall shear stress ratio $\frac{\langle\tau_w\rangle}{\tau_{w0}}$. The value of γ is typically between 1.5 and 2 [96] [97], but in the present study we assume γ = 2 as this value is expected for an ideal case [22]. Since Eq. (4) can be solved to obtain β as a function of α (for a given set of model inputs: γ, $\frac{\Lambda}{C_{f0}}$ and $(A_s/A)C_D^*$), we can calculate the power coefficient of a turbine in the farm:

Equation 3-5

$$C_P=\frac{\text{Power}}{\frac{1}{2}\rho U_{F0}^3 A}=\frac{TU_T}{\frac{1}{2}\rho U_{F0}^3 A}=\frac{U_F^2 U_T}{U_{F0}^3}\cdot 4\alpha(1-\alpha)=\beta^3\cdot 4\alpha^2(1-\alpha)$$

In addition, the normalised power density, η, can be defined [22] as an alternative representation of the farm performance:

Equation 3-6

$$\eta=\frac{\text{Power}}{\tau_{w0}U_{F0}S}=\frac{\frac{1}{2}\rho U_{F0}^3 A\cdot C_P}{\tau_{w0}U_{F0}S}=\Lambda\cdot\frac{1}{C_{f0}}\cdot C_P$$

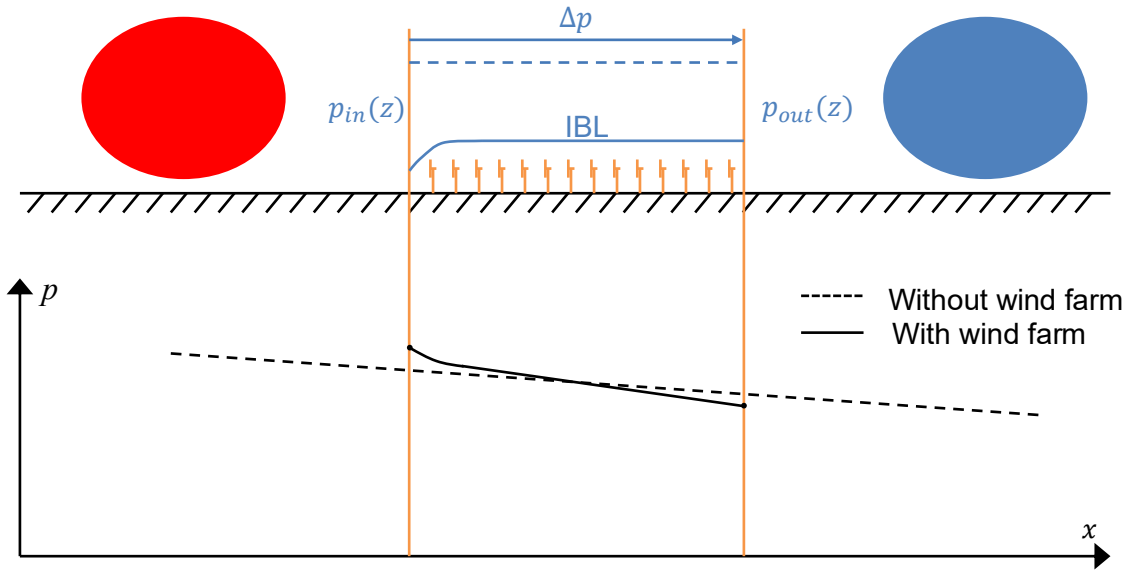

Figure 3-2 Schematic of an additional pressure gradient induced by a large finite-size wind farm. Reproduced from [21] with modifications.

A simple yet effective extension of the original two-scale coupled momentum model has recently been proposed by Nishino [21]. The main purpose of this extension was to overcome a major assumption in the original model, which was that the streamwise pressure gradient (given as the only driving force of the flow over the farm site) was the same before and after wind farm construction. This assumption seems reasonable when considering an ideal, infinitely large wind farm, but may not be appropriate for a large finite-size wind farm, where the reduction of wind speed may occur even upstream of the entire farm [100] and hence the farm may experience a larger streamwise pressure gradient than that observed before farm construction [21] [94]. Figure 3-2 shows a schematic of this additional pressure gradient induced by a large finite-size wind farm, where $p_{in}(z)$ and $p_{out}(z)$ are the pressure (as a function of the height, z) at the inlet and outlet of the farm site, respectively. If we consider a large control volume containing the entire farm and the internal boundary layer (IBL) developing over it, and assume that the momentum exchange through the top surface of this control volume is negligibly small, then we may still consider the (vertically averaged) pressure difference, Δp, as the only driving force of the flow over the farm. Therefore, by considering the (steady) momentum balance

before and after farm construction separately and then combining the two, we obtain the following farm-scale momentum equation:

Equation 3-7

$$\langle \tau_w \rangle S + T + D = \frac{\Delta p}{\Delta p_0} \tau_{w0} S$$

Comparing to Equation 3-1, it can be seen that the pressure ratio, $\Delta p_0/\Delta p$, has been added to the right-hand side to take into account the change of the driving force before and after farm construction. Note that, in reality, the momentum exchange at the top of the control volume in Figure 3-2 may not be negligibly small, but this effect can also be added to the right hand side of Equation 3-7 in a similar manner if necessary. It should also be noted that an implicit assumption here is that the IBL develops immediately at the entrance of the farm (i.e. the farm entrance effect is ignored) so that all turbines in the farm experience the same flow conditions; in reality, the IBL may or may not reach a fully developed state depending on atmospheric stability conditions [101]. Following the same procedure as the infinitely large farm case presented earlier, Equation 3-4 is now rewritten for the finite-size farm case as:

Equation 3-8

$$\left(4\alpha(1-\alpha) + \frac{A_s}{A} C_D^*\right) \frac{\Lambda}{C_{f0}} \beta^2 + \beta^\gamma - 1 = \frac{(\Delta p - \Delta p_0)}{\Delta p_0}$$

The right hand side of Equation 3-8, namely the farm-induced pressure term [21], depends on various environmental conditions, such as geographical characteristics of the farm site, atmospheric conditions and the ratio of the farm size to the size of the relevant atmospheric system driving the flow. However, for a given environment, this term should primarily depend on the farm-scale flow reduction factor β. In fact, the CFD results presented in [21] show that the farm-induced pressure term tends to increase approximately linearly with the farm-scale flow induction factor $(1-\beta)$, making it possible to model this term as:

Equation 3-9

$$\frac{(\Delta p - \Delta p_0)}{\Delta p_0} = \zeta(1-\beta)$$

where ζ is an 'environment-dependent' parameter, which requires an empirical estimation for a given wind farm. The estimation of this parameter ζ is outside the scope of this chapter; however, in chapter 5 we use a numerical weather prediction model with a single volume of momentum sink (representing an entire wind farm rather than individual turbines) to determine this parameter. In short, this parameter depends on how easily or not easily the flow approaching a large wind farm is deflected by the farm itself, and is therefore closely related to the so-called wind farm blockage effect [102].

3.3 Methodology

All calculations are conducted using the commercial CFD solver 'ANSYS FLUENT 17.2' [44]. Apart from certain model validation (single turbine) cases, majority of the simulations are performed as DES. The original version of the Detached-Eddy Simulations (DES) approach using the Spalart-Allmaras model (often referred to as DES97) is employed as a mean to conduct simple WMLES [103] [62], i.e. the flow in the vicinity of the bottom boundary is treated as in RANS and the rest of the domain is treated as in LES. The reason for employing DES97, instead of more advanced DES approaches, is that the thickness of the RANS layer can be fixed and controlled explicitly by adjusting near-wall mesh resolutions. As will be described later, we employ a uniform horizontal mesh resolution of 10m near the bottom boundary for the entire domain; hence, the thickness of the RANS layer is 6.5m in this study (as the DES model coefficient $C_{DES} = 0.65$ in DES97). In addition, similarly to the previous RANS study [96], the effect of bottom roughness is modelled using a modified wall function for 'fully rough' walls available in FLUENT [44] as follows:

Equation 3-10

$$\frac{U_p u^*}{\tau_w/\rho} = \frac{1}{\kappa}\ln\left(E\frac{\rho u^* y_p}{\mu}\right) - \Delta B$$

Equation 3-11 (a, b)

$$u^* = C_\mu^{0.25} k^{0.5},\ \Delta B = \frac{1}{\kappa}\ln(1 + C_S k_S^+)$$

Equation 3-12 (a, b)

$$k_S^+ = \frac{\rho k_S u^*}{u_\tau},\ u_\tau = \sqrt{\frac{\tau_w}{\rho}}$$

where U_p is the velocity at the centroid of the wall-adjacent cell (i.e. $y = y_p$). The two roughness parameters, namely the nominal 'sand-grain' type roughness height k_s and the roughness constant C_s, are set to be 1m and 0.5, respectively (this corresponds to an aerodynamic roughness length of $z_0 = 0.051$m since $k_s = (E/C_s)z_0$ [104], where $E = 9.793$ is an empirical value used in FLUENT [44]). The density and viscosity of the working fluid (air) are constant in this study: $\rho = 1.225$kg/m^3 and $\mu = 1.789 \times 10^{-5}$kg/m-s, respectively.

The effects of both turbine rotors and support structures are modelled as streamwise momentum losses, i.e. both rotors and support structures are modelled as stationary permeable (or porous) surfaces of zero thickness with a momentum loss factor (K for the rotors and K_s for the support structures), by which their resistance can be changed. Specifically, the instantaneous momentum loss is calculated as

Equation 3-13

$$M_x = K_{(s)} \cdot \frac{1}{2}\rho u^2$$

where u is the instantaneous streamwise velocity. Since the time-averaged rotor thrust and support-structure drag can be obtained as $T = \overline{\int M_x \,\mathrm{d}A}$ and $D = \overline{\int M_x \,\mathrm{d}A_s}$, it is possible to calculate the 'local' rotor thrust coefficient C_T^* and 'local' support-structure drag coefficient C_D^* as

Equation 3-14

$$C_T^* = \frac{T}{\frac{1}{2}\rho U_F^2 A} = K\frac{\overline{\int u^2 \mathrm{d}A}}{U_F^2 A}$$

Equation 3-15

$$C_D^* = \frac{D}{\frac{1}{2}\rho U_F^2 A_s} = K_s \frac{\overline{\int u^2 \mathrm{d}A_s}}{U_F^2 A_s}$$

However, for the purpose of comparison with the theoretical model, which is essentially for the time-averaged flow field and does not consider any velocity fluctuations in time, here we calculate C_T^* and C_D^* directly from the time-averaged flow field, i.e.

Equation 3-16

$$C_T^* = K \frac{U_T^2}{U_F^2}$$

Equation 3-17

$$C_D^* = K_s \frac{U_s^2}{U_F^2}$$

where U_T and U_s are the spatial- and time-averaged streamwise velocity over the rotor area A and the support-structure area A_s, respectively. Note that the values of C_T^* and C_D^* calculated from Equation 3-16 and Equation 3-17 are a little different from those from Equation 3-14 and Equation 3-15 since in general $\overline{u^2} > \bar{u}^2$; however, we ignore this small difference in this study. Similarly, since the time-averaged rotor power can be obtained as $P = \overline{\int M_x u \, \mathrm{d}A}$, it is possible to calculate the rotor power coefficient C_P as

Equation 3-18

$$C_P = \frac{P}{\frac{1}{2}\rho U_{F0}^3 A} = K \frac{\overline{\int u^3 \mathrm{d}A}}{U_{F0}^3 A}$$

but again, for the purpose of comparison with the steady theoretical model, here we calculate C_P as

Equation 3-19

$$C_P = K\frac{U_T^3}{U_{F0}^3} = K\alpha^3\beta^3$$

3.3.1 Turbine modelling method validation

3.3.1.1 RANS tests

Betz limit [19] tests were the first simulations that had been carried out using RANS in this study. Using enlarged domain with simple inlet-outlet boundary conditions. The main purpose was to test the functionality of the mesh, some of the boundary condition setup and RANS turbulence model comparison. The second step was to run 'empty box' simulations, to calculate the constant pressure gradient. Finally, the results from empty box simulations were applied to farm simulations (actuator disc simulations).

The current wind farm geometry is identical to Zapata's previous study [96], one of his staggered cases (Figure 3-3) has been used as a reference as well as a starting point. The horizontal size of outer domain is 7D by 7D (L_x=L_y=7D), where D is the diameter of one turbine rotor, and D in this case is 100m.

The shifted distance Δy is 0.5L_y and the ground clearance of the rotor is 0.5D. The rotor is modelled as an actuator disc for this simulation. The height of the domain is L_z =10D; this corresponds to the atmospheric boundary layer thickness. Periodic conditions are applied on both stream wise and lateral directions, in order to create an infinitely large wind farm. The centre of the coordinate is at the rotor centre (0,0,0).

The initial mesh created was much less refined than the previous study by Zapata [96], with approximately 960k elements compared to 1.8m elements. Moreover, a slightly different blocking strategy was used as well. The reasons are to have quick results and keep good level of accuracy. In addition, based on the mesh sensitivity study from the previous project, it is possible to use an even coarser mesh [105].

The local mesh refinement at the disc area is shown in Figure 3-4. Another important point is that the smallest mesh size near the ground is 1m, which is sufficient as the wall function approach is employed in this study.

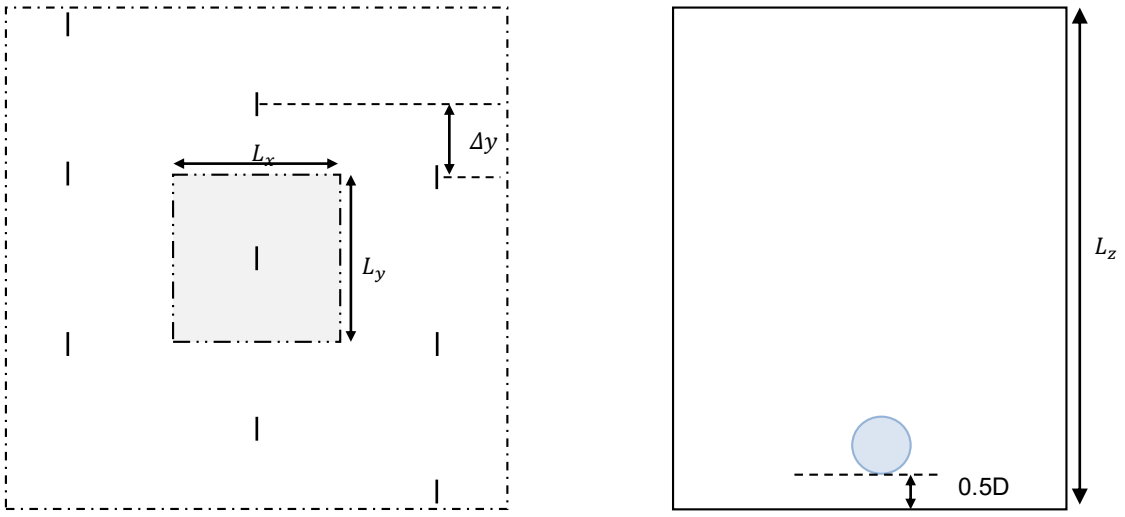

Figure 3-3 staggered turbine array, right: rotor position.

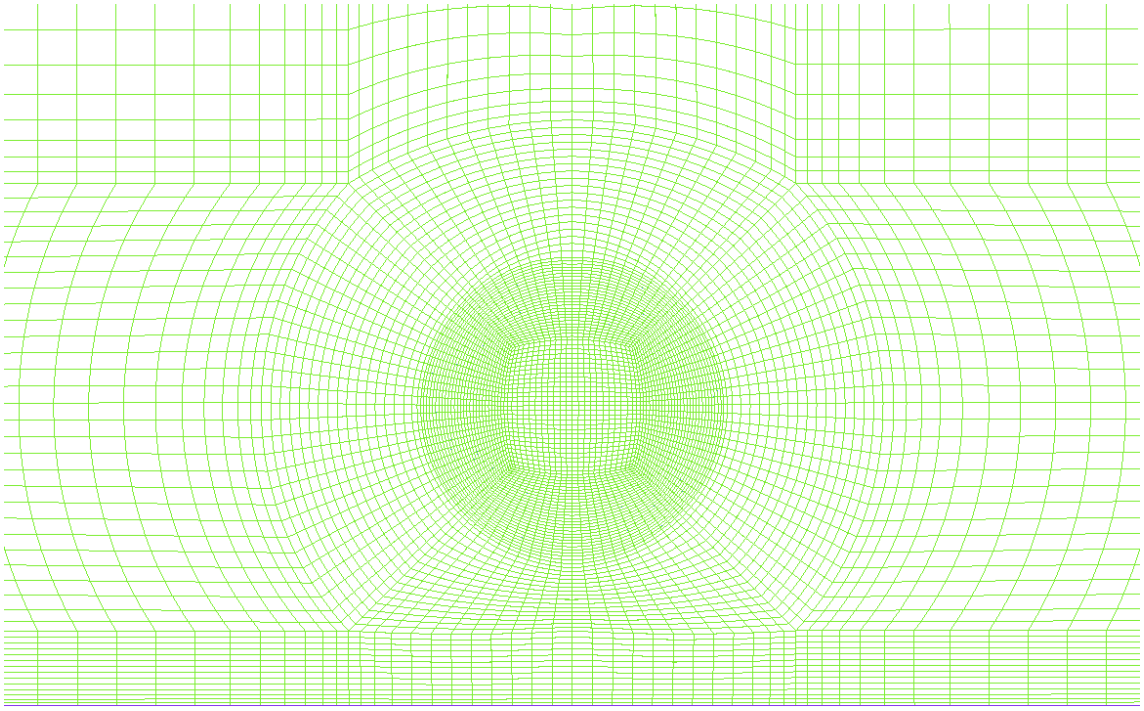

Figure 3-4 Disc mesh.

Three cases had been carried out in the Betz limit test step, with a single turbine in an extended domain (L_x=L_y=20D, the height L_z has been kept as 10D (Figure 3-5)) setup. Constant 10m/s inlet velocity with no ground roughness is

the initial condition for all cases. Inviscid, $k-\omega$ SST and $k-\varepsilon$ Realisable turbulence models had been applied to each case respectively, while keeping the boundary conditions the same. The idea is to eliminate any possible physical limitation from the domain size and numerical uncertainty from various turbulence models.

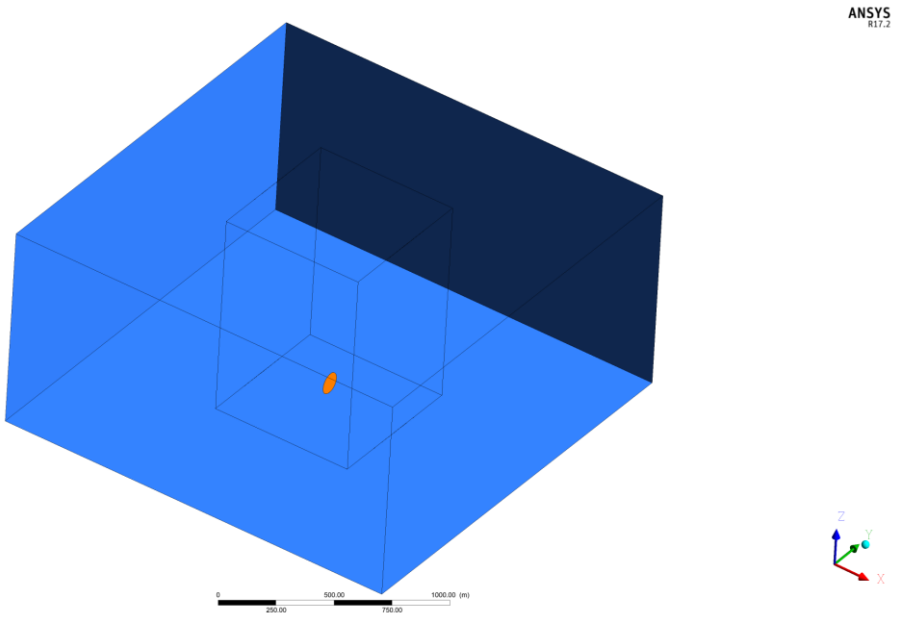

Figure 3-5 Extended domain.

The calculated C_p values have shown good agreement with Betz limit, with only an averaged 2.7% difference (Table 3-1), which can be explained as the local (partial) blockage effect due to the proximity of the bottom boundary [106].

Table 3-1 Betz limit tests.

	C_p	vs. Betz
Inviscid	0.608556	2.62%
k- ω SST	0.609425	2.77%
k- ε R	0.609425	2.77%
Betz limit	0.593	0.00%

As it has been stated in the 'two-scale momentum coupled' model, the atmospheric boundary layer should be driven by a constant pressure gradient [22]. To obtain this value, the so called 'empty box' calculations are required,

this method was suggested by previous studies [96] [107]. The actuator disc is assigned as 'interior' (that has no impact on the air flow) in this case, so that the domain is now an empty space [44]. Periodic conditions were applied in both stream wise and lateral direction representing infinitely large area, ground roughness was set as $K_s = 1m$ for this empty box simulation. Although the pressure gradient was unknown at this stage, the mass flow rate could be calculated based on domain size and inlet flow velocity in a simplified way. The calculation is:

Equation 3-20

$$Q = \rho(L_y \times L_z)V_{in}$$

Where air density ρ is 1.225kg/m^3, L_y is 700m, L_z is 1000m and V_{in} is 10m/s. This gives the mass flow rate as 8.58x10^{6}kg/s. Using this current mesh with $k-\omega$ SST turbulence model (suggested in previous study [107]), the calculated pressure gradient was 2.51x10^{-4}Pa/m, which is in good agreement with 2.60x10^{-4}Pa/m from the previous study by Zapata [96].

The following step was to further reduce the number of element in the model. The strategy was to significantly stretch the elements around the disc and slightly reduced element number within the disc keeping good continuity (Figure 3-6). The near ground region had been kept the same, so that the previously calculated pressure gradient cloud still be used. The stream wise element distribution was the same as previously, with a concentrated layer around the disc. The total number of element was approximately 460k.

A test case had been conducted using steady RANS ($k-\omega$ SST) simulation, with constant pressure driven inflow. The boundary conditions for this case are identical to Zapata's study [96]. Moreover, this case was a disc simulation, which means the actuator disc had been switched back to 'porous jump' condition. The wind profile at X=Y=0 (Figure 3-7) shown a good agreement between current mesh and Zapata's model around the most critical disc region. Although, there is a slight separation between the results at higher region of the domain, which could be due to significantly stretched cells. Since the area is

less essential and the difference is relatively small, therefore this separation has been considered as acceptable.

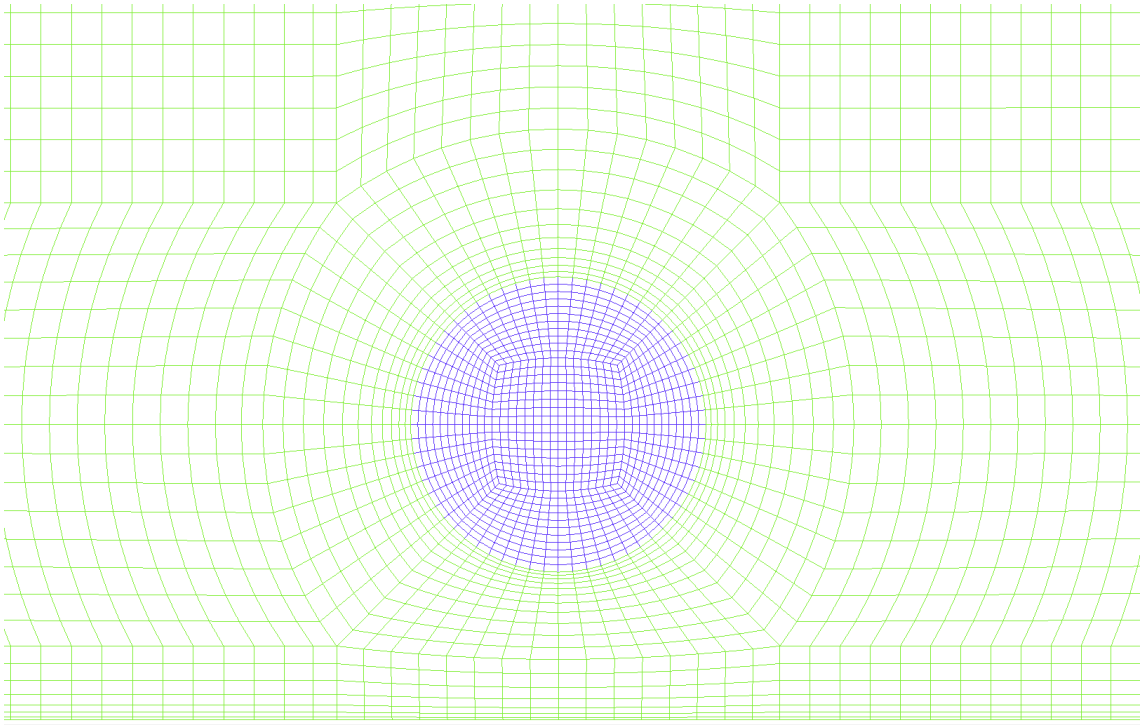

Figure 3-6 Coarse mesh.

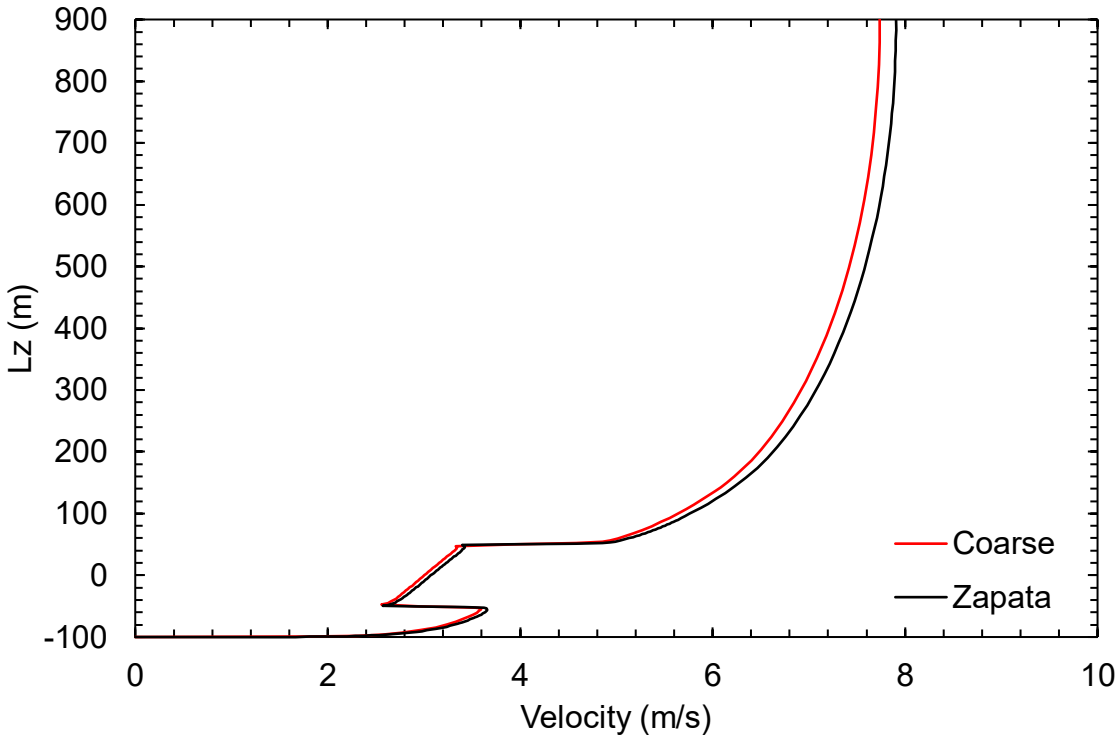

Figure 3-7 Vertical wind profile at X=Y=0.

3.3.1.2 DES tests

In order to perform DES, the mesh has been modified again to reduce the maximum cell aspect ratio to 1:1:2, the total element number now has also been reduced down to 360k (Figure 3-8). In addition, the ground region mesh has still been kept the same.

Following the RANS cases, empty box calculations are the initial step for DES too. However, DES was designed on the basis of aerospace problems, which means that thin boundary layer and obvious separations are assumed at the beginning. On the other hand, the entire domain is part of atmospheric boundary layer, which means that DES should be used as a wall-modelled LES approach [108], otherwise the DES empty box simulation would only have RANS modelling the entire domain.

The fundamental issue is that only a steady flow is introduced into the domain at the initial state of the simulation, which does not have large enough eddy-viscosity to trigger LES. To overcome this problem, a disc simulation is used as the starting simulation. The idea is using the actuator disc to disturb the flow field, thereby triggering the LES. After 100000 time steps (0.1s and 10 iterations for each time step), the flow is largely disturbed in the domain, this flow is then used as the initial flow for empty box simulation. The empty box takes another 100000 time step to finalise, then 300000 time steps are applied for the actuator disc calculation and further 50000 time steps with result sampling function to obtain the 16 final (time-averaged) results. It takes approximately 24 hours to run 50000 time steps using 128 CPUs. This is the general simulation strategy for all DES cases in this study.

Some preliminary testing cases have been conducted with the 460k mesh, instead of using just the calculated pressure gradient, the actual disc simulations are carried on from the empty box simulation. This strategy has shown promising physical response so far with all testing cases, reasonable flow field has been obtained in the domain.

Although there are some expected disagreements between DES and RANS cases in some respects, such as ground shear stress and farm layer average wind speed, based on the nature of DES and RANS, it is believed that the DES results are closer to reality. As can be seen from Table 3-2, the mesh sensitivity analysis has rather promising results, the differences are around 4%~5%. One thing should be

noted, the key simulations in this study are performed using multiple turbines, even though a few hundred thousands elements might not seem a big size for a single turbine mesh, the mesh size increases dramatically once we start increasing turbine numbers in the simulation. Therefore, the following study will be mostly carried out using the 360k mesh strategy. One thing should be noted, since there is no specific guideline for the grid size and number of elements for this type of DES model, therefore, this mesh sensitivity analysis is purely an engineering practice.

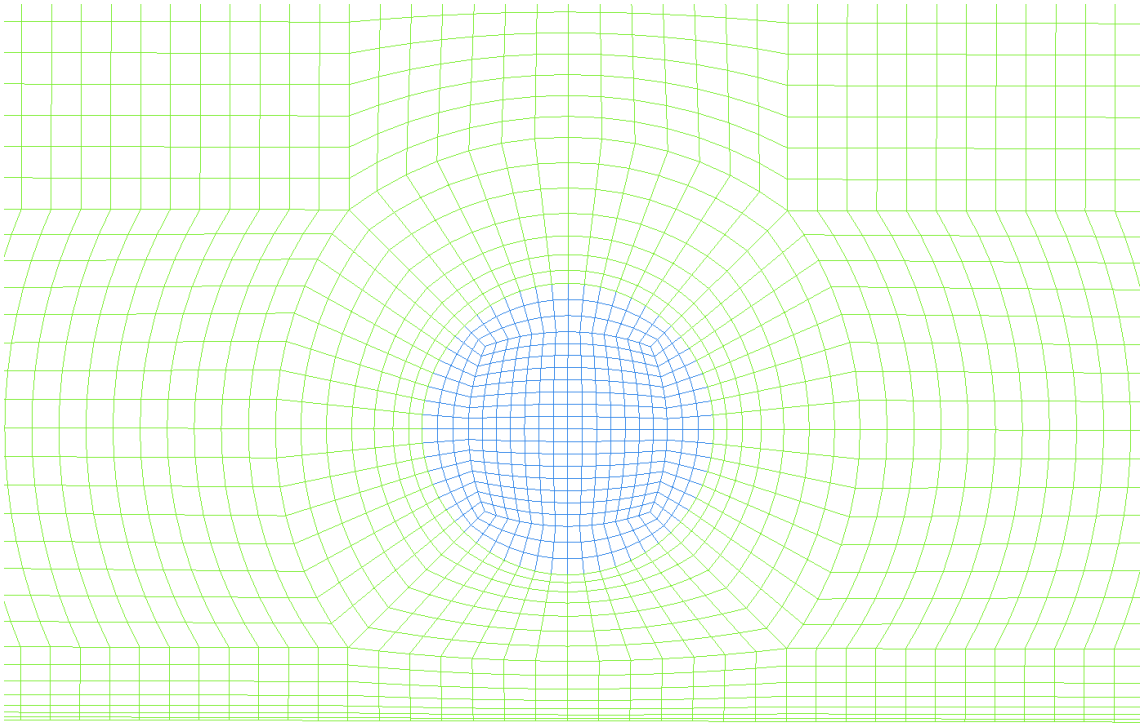

Figure 3-8 DES mesh.

Table 3-2 DES mesh sensitivity

	U_{f0}	U_f	U_t	α	β	τ_{w0}/τ_w	γ
460k	8.22	4.07	2.81	0.690418	0.495134	0.292	1.75125
360k	8.15	3.95	2.62	0.663291	0.484663	0.277	1.772378
Diff.	0.85%	2.95%	6.76%	3.93%	2.11%	5.14%	1.21%

3.3.2 Case studies, multiple turbines with support structure

In order to simulate the support-structure drag in a simplified manner, we consider that the support structure is located only below each rotor disc (as shown later in Figure 3-10). The areas of the rotor disc and support structure

are fixed for all cases in this study (with a ratio of A_s/A = 0.119), which means only the value of K_s needs to be modified to vary the support-structure drag. Here we consider seven different K_s values as summarised in Table 3-3. Two of the K_s values (0.542 and 1.716) were selected based on our initial speculation that these two values would result in C_D^* = 0.42 and 0.84 (and hence $(A_s/A)C_D^*$ = 0.05 and 0.1) if a theoretical relationship $C_D^* = K_s\left(\frac{4}{4+K_s}\right)^2$ (following the actuator disc theory) was satisfied; however, we eventually found that the actual C_D^* values obtained from the simulations were smaller than these initial speculations, as can be seen from Table 3-3. The difference could be due to the coarse mesh resolution for the tower as well as to the effects of the surroundings (ground and rotor disc) that are not considered in the actuator disc theory. Nevertheless, this is not a major issue in this study since the aim here is to make a comparison of wind farm performance between CFD and the theoretical model for a given $(A_s/A)C_D^*$ (and not for a given K_s or for a given tower design). In other words, the present approach (using a porous plate model with a coarse mesh) may not be sufficient to predict C_D^* accurately for a given K_s or for a given tower design but this is not the main concern of this study.

Table 3-3 Summary of support structure characteristics. Using different momentum loss factor K_s to mimic various tower drag effect.

Case	K_s	C_D^*	$(A_s/A)C_D^*$
1	0	0	0
2	0.542	0.270	0.0321
3	1.129	0.448	0.0533
4	1.422	0.505	0.0600
5	1.716	0.537	0.0640
6	4	0.739	0.0879
7	5	0.774	0.0921

The numerical methods employed are nominally second-order accurate in space and time, using a bounded central difference scheme for spatial discretisation of the momentum equations and a second-order implicit scheme for temporal discretisation. The SIMPLE algorithm is used for pressure-velocity coupling. A constant time step size of 0.1s is adopted with 10 iterations at each time step. Each farm simulation has been run for 600,000 time steps initially, followed by another 100,000 time steps to calculate the time-averaged results. Figure 3-9 shows an example of the time history of the streamwise velocity averaged over the four discs, showing that the simulation has been run long enough to obtain reliable time-averaged results. We have run for an additional 100,000 time steps (from 70000s to 80000s) to take another time-average of the velocity and confirmed that the difference from the original time-average value is about 2.03%.

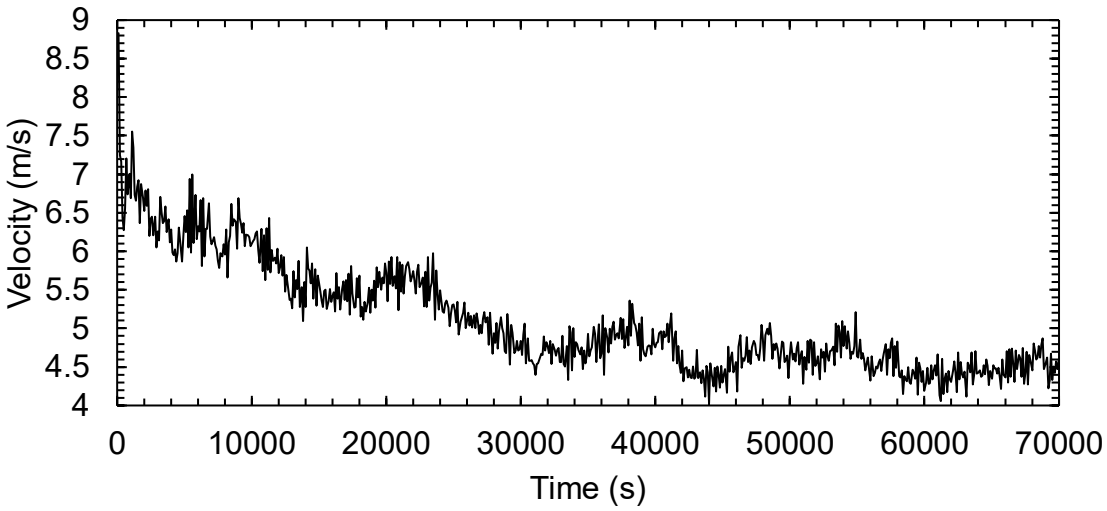

Figure 3-9 Example of the time history of streamwise velocity averaged over four discs (sampling rate is every 100s).

Multi-block structured meshes are employed in this study. A 2D mesh for a cross-sectional (y - z) plane is generated first and then extruded to the streamwise direction (x) to form the 3D mesh with hexahedral cells. An 'O-grid' mesh topology is used inside and around the rotor disc, to distribute cells along the edge of the disc. The smallest mesh spacing is 1m, which is for the first

cells above the bottom surface in the vertical (z) direction. For the horizontal (x and y) directions, however, a constant spacing of 10m is employed for the entire domain (Figure 3-10). The total number of cells is 1.3×10^6.

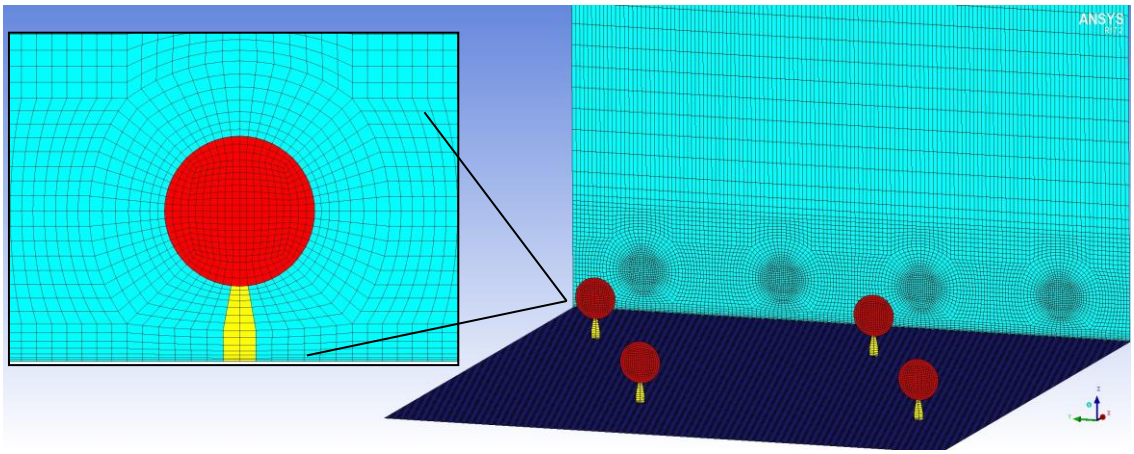

Figure 3-10 Cross-sectional mesh for the rotor disc (red), tower (yellow) and surrounding area (light blue).

3.4 Results and Discussions

3.4.1 Theoretical model results

3.4.1.1 Non-generalised

Some example solutions are presented below to show how the model predicts the effect of support structures on the farm performance, and then an optimal farm density to maximise the performance. Traditional turbine spacing for offshore wind farms is around 7*D* and could potentially be as large as 15*D* [109]. Furthermore, for an average wind speed of 10m/s, for example, the natural friction coefficient of the sea surface can be assumed to be around 0.002 (depending on various wind-wave interaction parameters) [110]. Therefore, we presume that a typical range for the effective farm density (Λ/C_{f0}) of offshore wind farms should be around 2 to 8, assuming an inter-turbine distance of around *7d* to *14d*. It is also worth noting that some recent studies suggest that an even shorter inter-turbine distance may be beneficial for a wind farm with wake control, e.g. [111]. Hence, in the example below, we consider a wider range of 0 to 10 for the effective farm density.

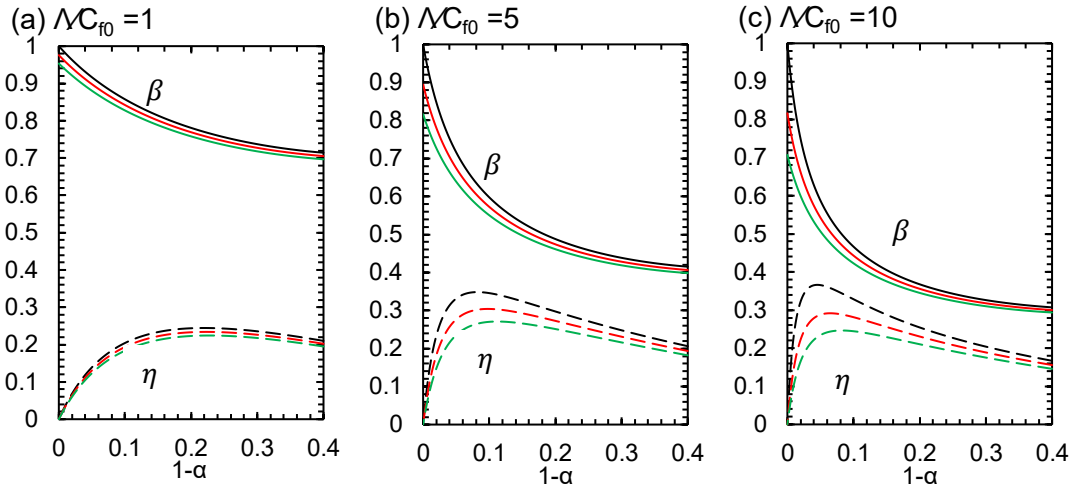

Figure 3-11 Effects of support-structure drag on the performance of infinitely large wind farms: solid and dashed lines show β and η, respectively, and $(1-\alpha)$ is the local axial induction factor of each rotor. Black: $(A_s/A)C_D^* = 0$; red: $(A_s/A)C_D^* = 0.05$; and green: $(A_s/A)C_D^* = 0.1$. As the farm density increases, the support-structure effect becomes more obvious.

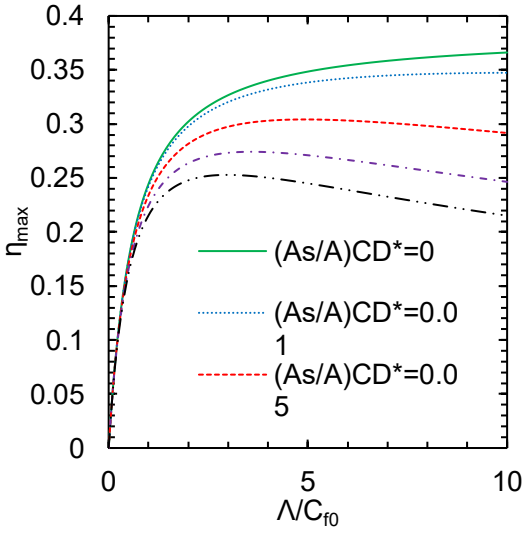

Figure 3-12 The maximum normalised power density η_{max} (for infinitely large wind farms) against the effective farm density Λ/C_{f0} for various normalised support-structure drag $(A_s/A)C_D^*$.

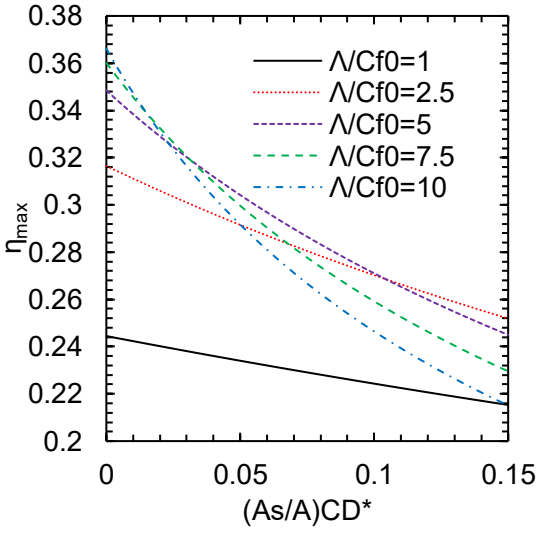

Figure 3-13 The maximum normalised power density η_{max} (for infinitely large wind farms) against the normalised support-structure drag $(A_s/A)C_D^*$ for various effective farm density Λ/C_{f0}.

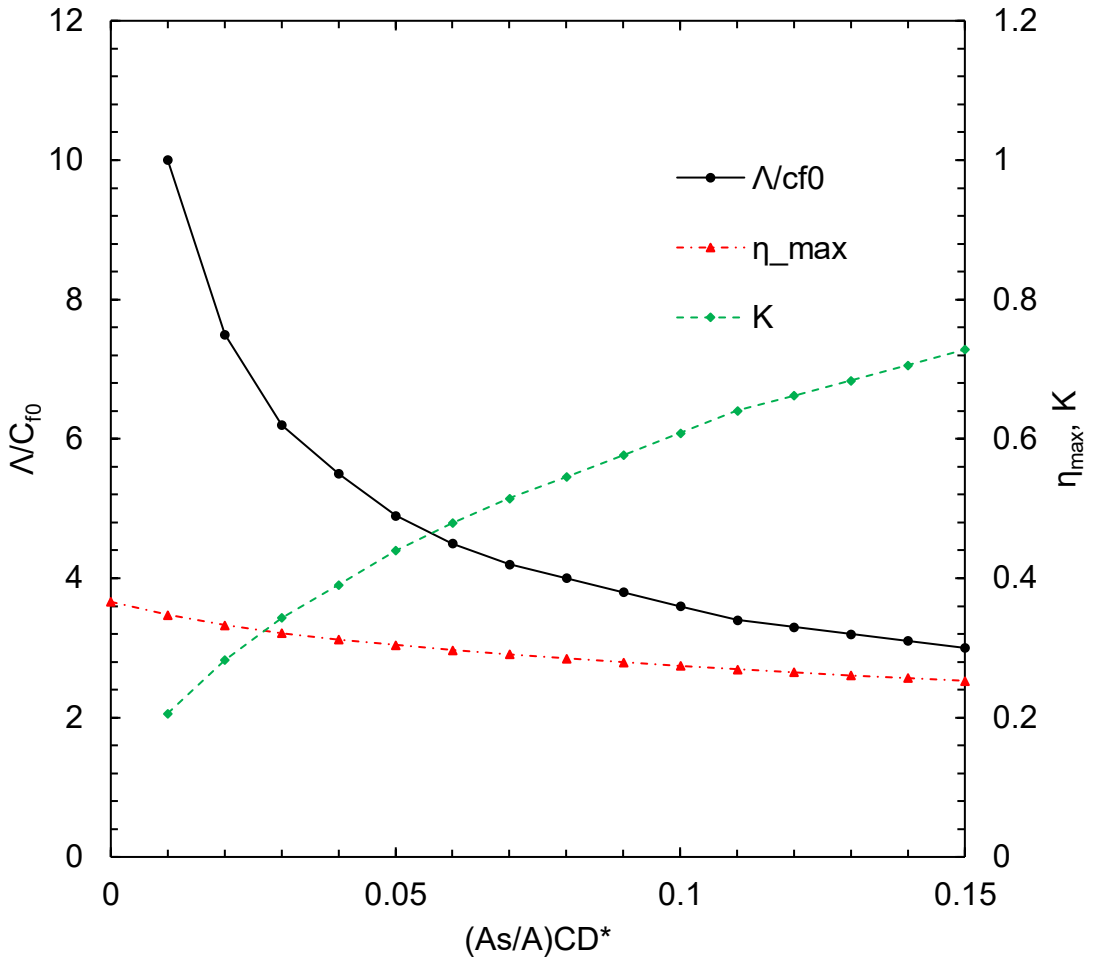

Figure 3-14 The optimal values of effective farm density Λ/C_{f0}, rotor resistance $K\left(=\frac{4(1-\alpha)}{\alpha}\right)$ and the maximum normalised power density η_{max} (for infinitely large wind farms) plotted against the normalised support-structure drag $(A_s/A)C_D^*$.

For the most common monopile-type foundation design for large offshore wind turbines (with a diameter of typically about 2 to 6 m) [112], the drag coefficient is expected to be around 0.6 (from that for a circular cylinder under relevant Reynolds number conditions [113]), and hence the value of the normalised support-structure drag ($(A_s/A)C_D^*$) is expected to be up to about 0.1 in most cases (depending on the area ratio A_s/A). Note that, strictly speaking, the value of C_D^* (defined as in Equation 3-3 using the farm-average wind speed U_F instead of an upstream wind speed) can be different from the value of a commonly used drag coefficient (defined using an upstream wind speed). However, this difference is expected to be small unless the turbines are perfectly aligned with

the wind direction to cause a significant level of direct wake interference [94]. Figure 3-11 shows the variations of β and η against the 'local' axial induction factor $(1-\alpha)$, for three infinitely-large wind farms with Λ/C_{f0} values of 1, 5 and 10, respectively, with three $(A_s/A)C_D^*$ values of 0, 0.05 and 0.1. The overall wind farm performance is hardly influenced by the support structures when the effective farm density is small ($\Lambda/C_{f0}=1$). However, as the farm density increases, the support-structure effect becomes more obvious; for example, at $\Lambda/C_{f0}=5$, the maximum power density for $(A_s/A)C_D^*$ = 0.1 (η_{max} ≈ 0.27 at α ≈ 0.89) is more than 20% lower than that for $(A_s/A)C_D^*$ = 0, i.e. for the case without support structures (η_{max} ≈ 0.35 at α ≈ 0.92).

Figure 3-12 and Figure 3-13 summarise the effects of farm density and support-structure drag on the maximum farm performance. When the support-structure drag is zero, this model goes back to the original two-scale coupled momentum model [22], in which the maximum power density η_{max} always increases with the effective farm density Λ/C_{f0} and approaches asymptotically to η_{max} = 0.385. However, when the support-structure effect is considered, the power density increases with the farm density only up to an optimal value, above which the power decreases (Figure 3-13). Importantly, the impact of support-structure drag on the maximum power density becomes more and more significant as the farm density increases (Figure 3-13). This is basically because the optimal rotor thrust decreases [96] and therefore the relative importance of support-structure drag increases as the farm density increases. It should be noted that, while the rotor thrust can be reduced or optimised by changing the rotor operating conditions, the support-structure drag cannot be reduced unless the design of support structures is changed. This implies that the farm density of a very large wind farm should be optimised by taking into account the design of support structures. This can be seen more clearly from Figure 3-14, which shows how the optimal values of the effective farm density (Λ/C_{f0}) and rotor resistance $(K=\frac{T}{\frac{1}{2}\rho U_T^2 A}=4(1-\alpha)/\alpha)$ change with the normalised support-structure drag $((A_s/A)C_D^*)$. Also plotted in this figure are the maximum normalised power density (η_{max}) values obtained from such an optimisation.

3.4.1.2 Generalised

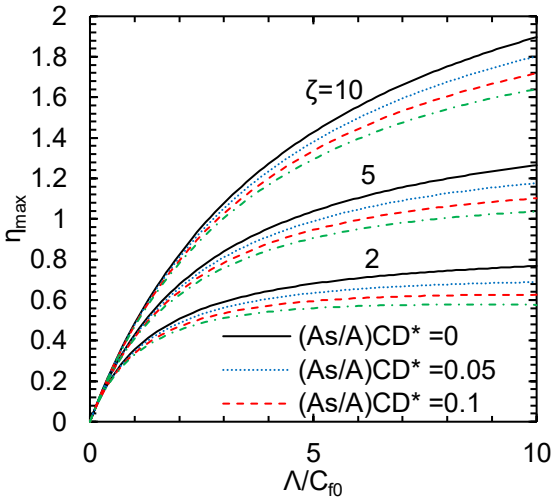

Figure 3-15 The maximum normalised power density η_{max} against the effective farm density Λ/C_{f0}, for various normalised support structure.

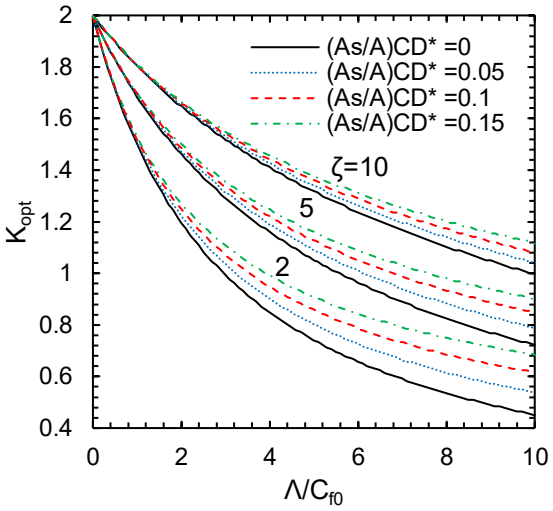

Figure 3-16 The optimal rotor resistance K_{opt} against the effective farm density Λ/C_{f0}, for various normalised support structure drag.

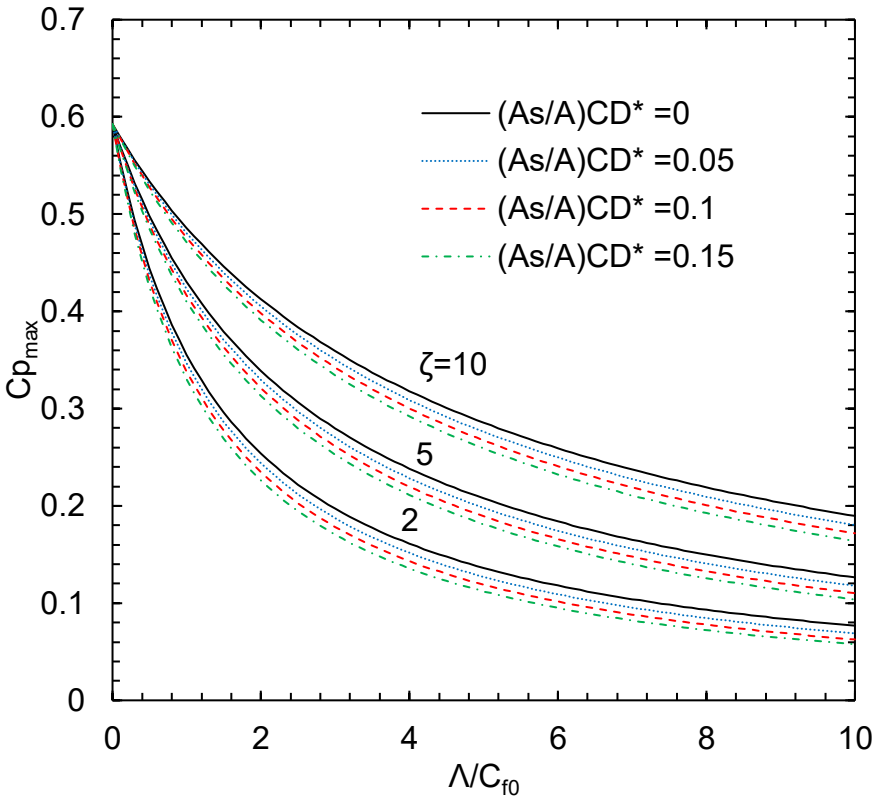

Figure 3-17 The maximum C_p value against the effective farm density Λ/C_{f0}, for various normalised support structure drag $(A_s/A)C_D^*$ and environmental parameter ζ.

Some example results of the extended model are shown in Figure 3-15 to Figure 3-17 with three ζ values: 2, 5 and 10. Although there are no conclusive data supporting the choice of these three values at this stage, the CFD simulation results presented in [21] suggest that a typical value of this environmental parameter may vary between 5 and 10 depending on the natural roughness length of the farm site (e.g. onshore or offshore). Figure 3-12 is a similar plot to Figure 3-12 but now for finite-size wind farms. One key difference from the infinitely large case presented earlier is that the maximum normalised power density (η_{max}) no longer has a clear peak point at Λ/C_{f0} < 10. When ζ equals to 2 the power density tends to be maximised around Λ/C_{f0} = 10; however, for ζ equals to 5 and 10, the power density is maximised at Λ/C_{f0} > 10, meaning that the optimal farm density (to maximise the power density) increases with the response strength of the driving force of flow over the farm (which is represented by ζ in this model). It should be remembered that Λ/C_{f0} of higher than 10 may be unrealistic (at least from the current industrial standard) and also, as noted in the previous subsection, the theoretical model may become invalid at such a high Λ/C_{f0}. Nevertheless, these results show that the support structure drag may still affect the power density substantially, in a realistic range of Λ/C_{f0}, not only for infinitely large but also for large finite-size wind farms (regardless of the value of ζ). The optimal rotor resistance (K_{opt}) plot in Figure 3-16 also shows the importance of the support structure drag for all three different ζ cases, but especially when ζ is small (ζ = 2 in this case). Finally, Figure 3-17 shows the effects of support structure drag on the maximum power coefficient of each turbine ($C_{p\,max}$) for the three different ζ cases. The results for $(A_s/A)C_D^*$ = 0 (i.e. without tower) agree with the previous study [21], and as expected, the support structure drag tends to reduce $C_{p\,max}$. Overall, these results show that both ζ and $(A_s/A)C_D^*$ tend to affect the power of large finite-size wind farms substantially.

3.4.2 Case results

Table 3-4compares results of 'empty box' simulations using WMLES and RANS. For RANS, we have tested the *k-ω* SST model as well as the Spalart-Allmaras

model for comparison. Also presented for comparison are results from the previous RANS study by Zapata et al. [96] using the Standard *k-ε* model. The (spatial- and time-averaged) natural bottom shear stress τ_{w0} obtained from WMLES is about 14% smaller than the Spalart-Allmaras RANS result. This trend, that WMLES using DES97 tends to yield a smaller wall shear stress, is in agreement with [103]. It should also be noted that the quantitative accuracy of the prediction of τ_{w0} for a given roughness height is not our primary concern, because the theoretical results to be compared with these CFD results for validation (such as the power coefficient C_P) are given as a function of Λ/C_{f0} (not as a function of the roughness height).

Table 3-4 Comparison of 'empty box' results between WMLES and RANS.

	τ_{w0} (Pa)	Pressure gradient (Pa/m)	U_{F0} (m/s)	H_F/d	Λ/C_{f0}
WMLES	0.1785	-1.785×10^{-4}	8.89	2.8	4.35
Spalart-Allmaras (RANS)	0.2081	-2.081×10^{-4}	8.55	2.6	3.45
k-ω SST (RANS)	0.2364	-2.364×10^{-4}	8.59	2.6	3.06
Standard *k-ε* (RANS) [96]	0.2597	-2.597×10^{-4}	8.34	2.6	2.63

Key results from the farm simulations (using WMLES) are summarised in Table 3-5, where C_P is calculated using Equation 3-19. It can be seen that the turbine support structures have a minor effect on the value of γ, which is slightly higher than that obtained in the previous RANS study [96] but still approximately 10% lower than $\gamma = 2$, which was considered as a theoretical upper limit in the two-scale momentum model [22].

Table 3-5 Summary of farm simulation results ($\mathbf{H_F = 280}$m, $\mathbf{U_{F0} = 8.89}$m/s).

Case	K	α	β	τ_w/τ_{w0}	γ	C_P
1	0.5	0.880	0.598	0.402	1.77	0.0728
2	0.5	0.873	0.598	0.397	1.80	0.0713
3	0.5	0.872	0.572	0.374	1.76	0.0622

4	0.5	0.870	0.569	0.365	1.79	0.0605
5	0.5	0.876	0.572	0.365	1.80	0.0627
6	0.5	0.883	0.569	0.363	1.80	0.0634
7	0.5	0.882	0.550	0.341	1.80	0.0570

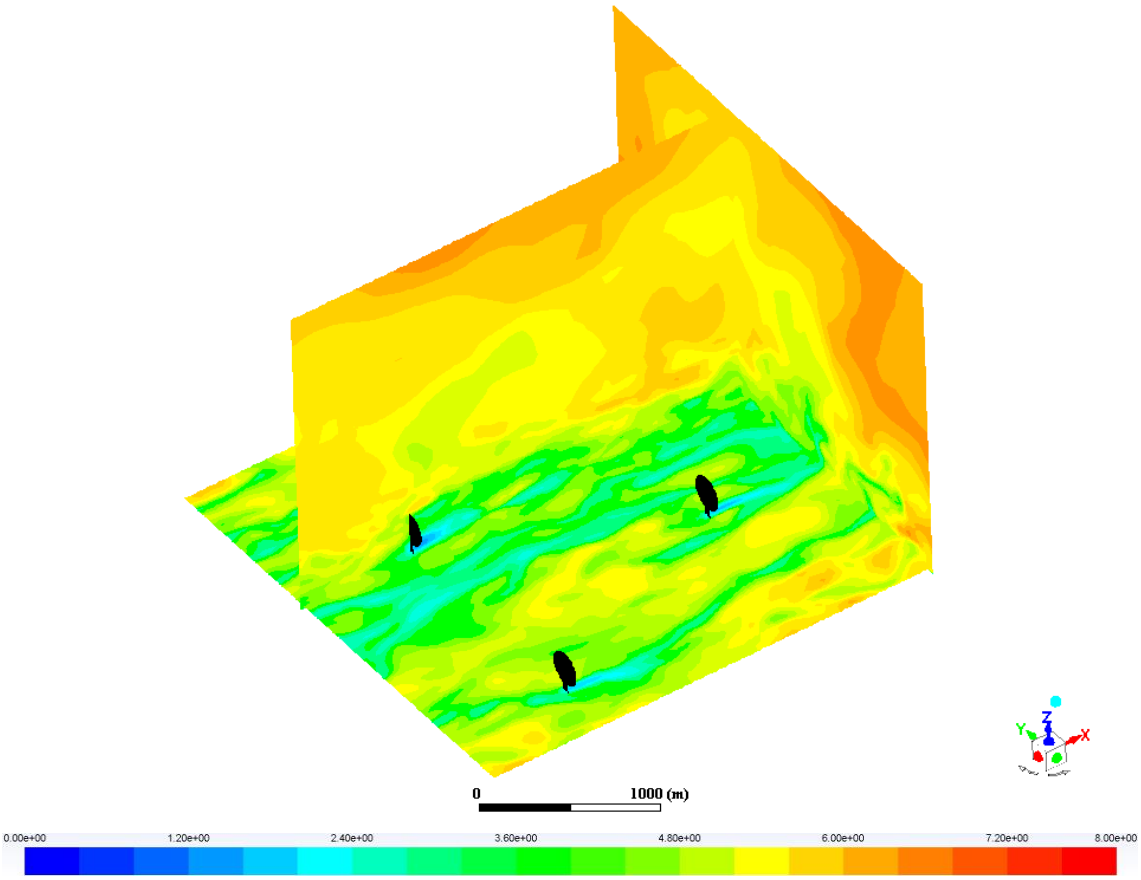

Figure 3-18 Instantaneous streamwise velocity contours [m/s] on the horizontal plane at the tower mid-height, streamwise vertical plane across the centre of a turbine, and the spanwise vertical plane at the downstream end of the domain (taken at the last time step). Case 6 (with towers, $K_s = 4$).

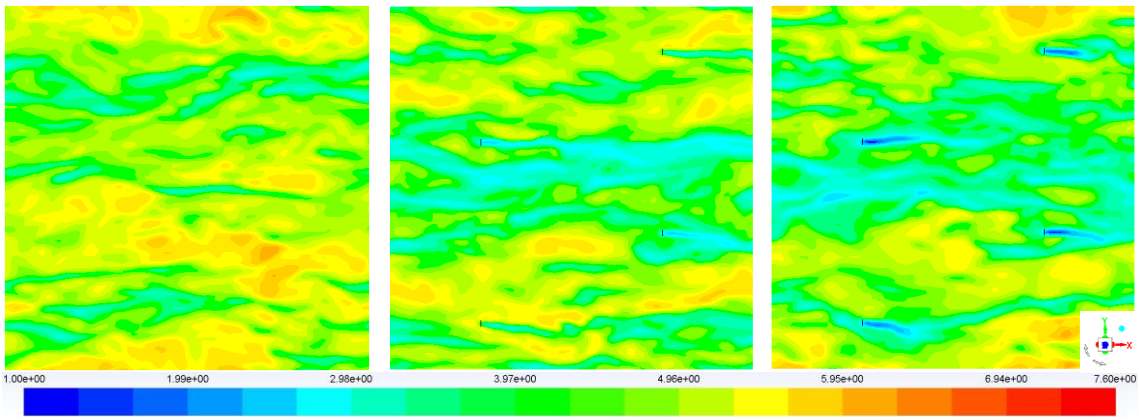

Figure 3-19 Contours of instantaneous streamwise velocity [m/s] at the tower mid-height (taken at the last time step). Left: Case 1 (no towers, $K_s = 0$), middle: Case 5 (with towers, $K_s = 1.716$), right: Case 6 (with towers, $K_s = 4$).

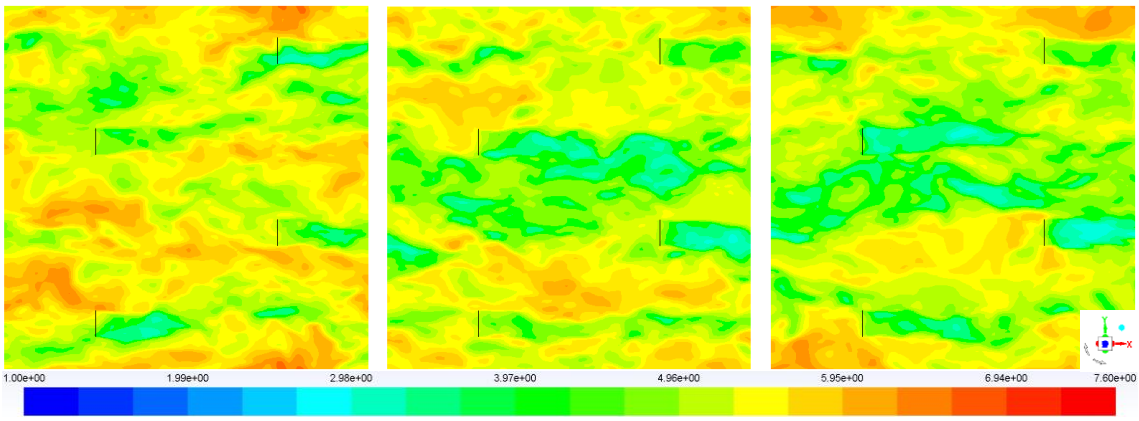

Figure 3-20 Contours of instantaneous streamwise velocity [m/s] at the rotor hub-height (taken at the last time step). Left: Case 1 (no towers, $K_s = 0$), middle: Case 5 (with towers, $K_s = 1.716$), right: Case 6 (with towers, $K_s = 4$).

Figure 3-18 shows an example of instantaneous velocity contours on three different places, visualising the wakes of the turbine rotors and support structures. More details of the instantaneous flow field are compared between three different cases in Figure 3-19 and Figure 3-20; the former is on a horizontal plane at the tower mid-height and the latter is at the rotor hub-height. It can be seen that a narrow but increasingly clear wake pattern is visible behind each tower as the tower drag increases (Figure 3-19), even though the towers have been modelled in a rather simplified manner. In addition, not only at the tower mid-height but also at the rotor hub-height (Figure 3-20), the streamwise velocity is (on average) slowed down due to the high support-structure drag.

This can be seen more clearly in Figure 3-21, which shows a comparison of time-averaged velocity profiles behind one of the turbines between the cases with and without tower. In addition to creating the narrow wake, the tower also tends to cause an effect similar to the local blockage effect [114], i.e. the acceleration of flow below the rotor (that happens if there is no tower) is prevented by the tower; such a blockage effect is not accounted for in the theoretical model presented in the previous section.

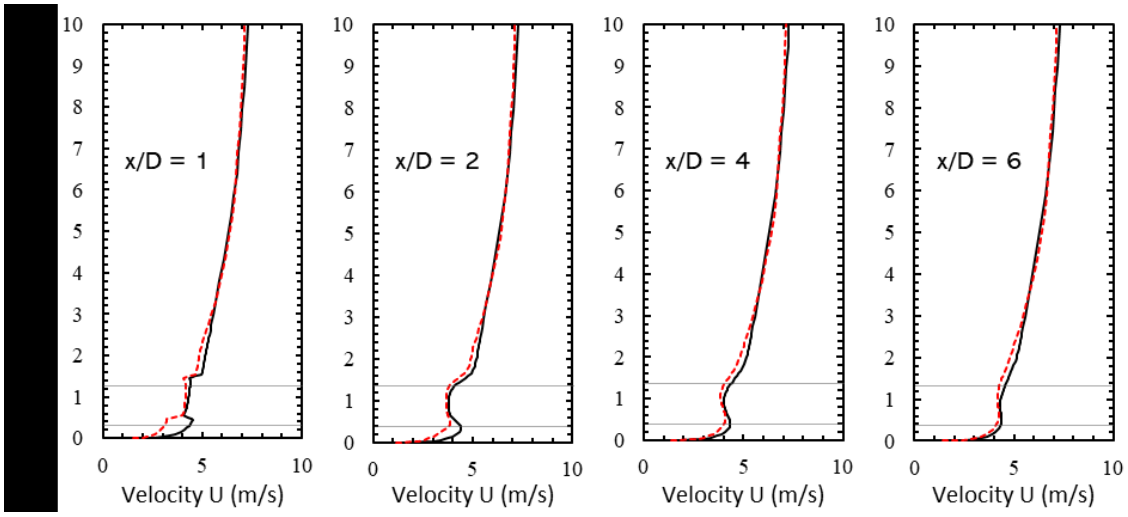

Figure 3-21 Time-averaged streamwise velocity profiles behind one of the turbines. Black solid line: Case 1 (no towers, $K_s = 0$), red dotted line: Case 4 (with towers, $K_s = 1.422$).

3.4.3 CFD vs. theoretical model

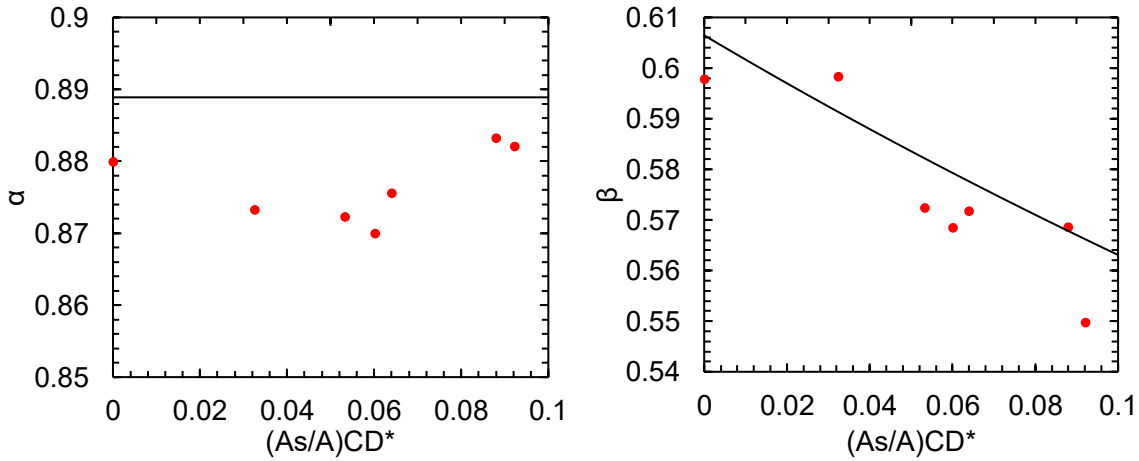

Figure 3-22 Comparison of α (left) and β (right) between CFD (red symbols) and

theoretical model (black line). Both theoretical and CFD results show constant or nearly constant α because the rotor resistance K is fixed. The same trend that β decreases as the support-structure drag increases is shown in the two models, the difference in β is about 3% at the maximum.

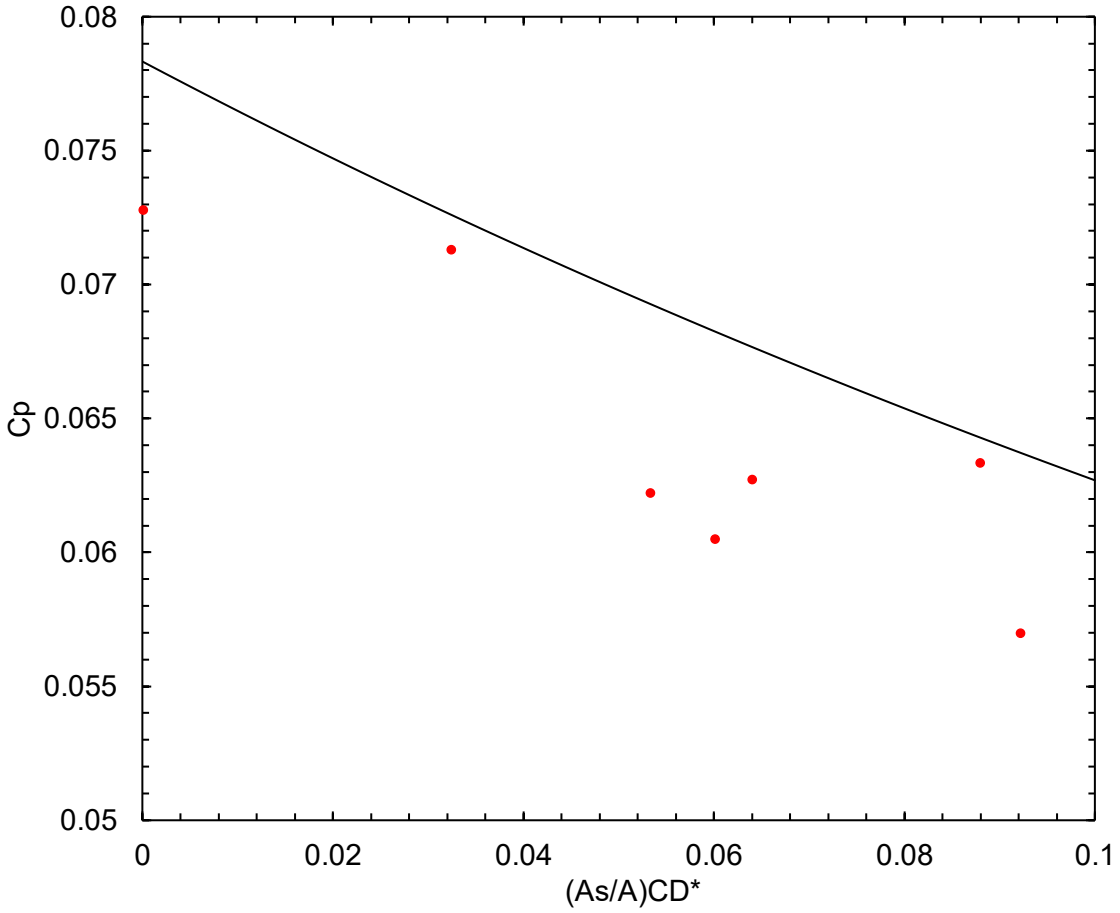

Figure 3-23 Comparison of C_P between CFD (red symbols) and theoretical model (black line). The maximum difference in C_P is about 10%, which is still reasonably good, considering the complexity of the 3D unsteady flow field simulated by CFD and the simplicity of the steady quasi-1D theoretical model.

Now we compare the values of α, β and C_P obtained from the CFD simulations with the theoretical model predictions. In the theoretical model, α is constant at 8/9 when the rotor resistance K is fixed at 0.5 (because $K = 4(1-\alpha)/\alpha$); meanwhile, the CFD simulations show nearly constant α values of slightly less than 8/9 (Figure 3-22-left). Both CFD and theoretical model also predict the same trend that β decreases as the support-structure drag increases (Figure

3-22-right); the difference in β is about 3% at the maximum, which is similar to that found in the previous RANS study [96] (where the discrepancy was less than 3% for the case without towers). Lastly, the values of C_P obtained from the present CFD simulations are also in good agreement with the theoretical model predictions, showing the same trend that C_P decrease as the support-structure drag increases (Figure 3-23). The values predicted by CFD are somewhat lower than the theoretical predictions, resulting from the slight differences in α and β. The maximum difference in C_P is about 10%, which is still reasonably good, considering the complexity of the 3D unsteady flow field simulated by CFD and the simplicity of the steady quasi-1D theoretical model.

Finally, it should be noted that the present study has considered only the staggered array and not the aligned array of turbines. As demonstrated by earlier RANS studies (for cases without support structures) [22] [96], when the turbines are aligned perfectly with the wind direction, the value of C_P may further decrease due to the direct interference of rotor wakes and hence the difference from the quasi-1D theoretical model tends to increase. However, such a perfectly aligned situation is not very common in real wind farms.

3.5 Conclusions

An extended two-scale coupled momentum model has been proposed in this study to estimate potential impacts of turbine support-structure drag on the aerodynamic performance of (i) an ideal, infinitely large wind farm and (ii) a more realistic, large but finite-size wind farm. A key implication of the proposed model is that the support structures may have an increasingly important influence on the overall farm performance as the farm density (or the number of turbines installed in a given farm area) increases. This is essentially because the optimal rotor thrust decreases and therefore the relative importance of support-structure drag increases as the farm density increases. In particular, for the case of an infinitely large wind farm, the proposed model predicts that the optimal inter-turbine spacing (to maximise the power density) depends on the support-structure drag, or more specifically, the normalised support-structure drag $(A_s/A)C_D^*$.

For the case of a finite-size wind farm, the proposed theoretical model requires an estimation of an environment dependent parameter, ζ, for a given wind farm environment. This parameter represents the response characteristics (or strength) of the driving force of flow over the finite-size wind farm. The prediction of the value of ζ is the scope of an ongoing research and is outside the scope of this study. However, we have employed three different values of ζ (selected based on an earlier CFD study in [21]) to investigate the impact of support-structure drag on the performance of three different hypothetical wind farms. The results show that the support-structure drag may still play an important role in a large finite-size wind farm regardless of the exact value of ζ. However, the optimal farm density increases with the response strength of the driving force; hence, the optimal turbine spacing cannot be predicted without knowing the value of ζ. It is therefore crucial to estimate this environmental parameter carefully and accurately in the future.

A series of CFD simulations (WMLES) of a periodic staggered array of wind turbines (with both rotors and support structures modelled simply as streamwise momentum losses) has also been conducted for comparison with the theoretical model for the case of an infinitely large farm case. Seven different resistance (K_s) values are employed for the support structures (towers) with all other conditions unchanged. The results confirm that the average wind speed through the farm tends to decrease, and so does the power, as the level of support-structure drag increases. The maximum difference in the power predicted is about 10%, which is a reasonably good agreement, considering the complexity of this unsteady 3D flow problem and the simplicity of the steady quasi-1D theoretical model.

4 Blade-resolved Model Approach

4.1 Introduction

To continue the conversation in the previous chapter, we have already established the existence of tower effect in both theoretical model and CFD wind farm model (with actuator disk turbine model). In order to further testing this concept, we use the fully resolved turbine approach in this chapter.

A variety of approaches exist to model wind turbines of different sizes, types and use purposes. Each type of turbine models has its specific strength as well as downside. The actuator disk model, as we have discussed in the previous chapter, has been widely adopted in wind energy studies [22] [87] [115] [116]. It is relatively simple to implement and low computational cost, however, it can represent only limited details of the turbine. One step above is the actuator line model, it considers the rotational motion of turbine blades and uses predetermined aerofoil data to represent the loading on each blade [117] [118] [119]. Even though, it is still essentially an actuator device that extracts momentum from the flow. The most comprehensive and computationally intensive method is the fully resolved (FR) model, where the exact 3D geometry of the wind turbine is resolved during simulations, therefore, it models turbine motions and flow behaviours in a much more realistic manner [120] [121] [122].

Furthermore, due to the complex and computationally expensive nature of the fully resolved turbine model, it has been primarily used for isolated turbine or a very small number (commonly two) of turbines simulations [123] [124] [125] [126], and not for large wind farms.

In 2009 Zahle et al. [127] conducted investigations on wind turbine rotor-tower interaction using FR NREL Phase VI turbine model [128]. Two simulations (using EllipSys3D) were presented in their study, one isolated rotor case and the other is downwind configuration of a full turbine (with tower) under tunnel flow conditions. The simulations results showed good agreement with existing experimental data. The CFD data shown clear interaction between the tower wake and rotor blades, which causes noticeable velocity deficit in the wake and

the blades has a strong effect on the tower shedding frequency. However, no details were mentioned on the tower related turbine efficiency variation in this study.

Most recently in 2020, Dose et al. [129] made further improvement on their existing model, by adding two different types of support structure, monopile and jacket tower. The numerical model as well as research methodology were both the same as their previous work, which kept the desired consistency through their research development. The results showed the power output was almost identical to the rotor only model, it is believed this is due to both models were isolated single turbine simulations, therefore the rotor performance should not be noticeably influenced by the support structure. Although, the downstream wake structure did change, which means that for wind farm simulation, the support structure would theoretically have an impact on the overall wind farm efficiency.

In a more recent (2019) study, Rodrigues and Lengsfeld established a computational framework, which was designed to investigate wind farm layout [121] [130]. They developed a twin FR turbine (in parallel) model based on the MEXICO (Model Experiments in Controlled Conditions) experiment, also adopted the velocity wake data from the MEXICO study as the initial wind flow conditions. Their approach to mimic wind farm flow conditions was to perform sequential simulations (all using the same twin turbine model), where outlet of the first simulation (or the first row of turbines in a wind farm) was the inlet of the second simulation. The results showed clear tower wake in both near and far wake flow field, and have stated noticeable velocity deficit as well as increased turbulence intensity. Even though this study did not investigate how the turbine and wind farm efficiencies were affected by the turbine towers. On the other hand, their approach of modelling wind farm flow might have the advantage of not having to deploy multiple turbines (more than two) in the domain, which would dramatically increase the mesh size, hence long simulation cost. However, the wind farm layout is limited with fully aligned and 10D spacing

between each row of turbines, which both design features are less commonly seen in modern large wind farms.

As a continuation of a previous study by Delafin and Nishino [107], in this chapter we analyse the differences of overall wind farm efficiency, with and without the turbine support structure (a typical monopile design in this case). The FR turbine model is based on the NREL 5MW horizontal-axis turbine design [52] [131], the wind flow is simulated by solving unsteady Reynolds-averaged Navier-Stokes (URANS) equations. A fully developed wind farm boundary layer is achieved by applying full periodic conditions (streamwise and spanwise directions) for the domain, which enables the simulation of one turbine operating inside and infinitely large wind farm with a fully staggered layout. The URANS results are analysed in conjunction with a modified version of the theoretical model initially proposed by Nishino [22] [132]. In addition, we also perform a Delayed Detached Large-Eddy simulation (DDES) using the same FR turbine model, which shows the possibility and advantages of high fidelity CFD wind farm modelling.

The work presented in this chapter is a collaboration with Delafin. The turbine 3D model and mesh were created by Delafin, and the rotor only URANS was partially performed prior to this present study.

4.1.1 NREL 5MW

The turbine sample used in this case is the NREL designed 5MW three blades model [52], that has 126m diameter (D). We have also taken into account the alternations suggested by Sandia National Laboratories [131], unlike the original design, smoothing process has been applied to blade thickness distribution as well as root-blade transition. Furthermore, the tip shape was not specified in the reference designs, a ‘rounded’ tip design approach is used in this study. In addition, to simplify the construction process of a fully structured mesh, the hub diameter has been increased to 5.4m (3m in the original design). The hub centre is at 90m above the ground, which is equivalent to 0.21D ground clearance. There is 5° (respect to the horizontal plane) tilt angle applied to the rotational axis and a 2.5° upwind precone, as defined in [52]. More detailed 3D

modelling of this turbine will be demonstrated in the following section, some of the modifications will also be discussed further.

4.2 Methodology

4.2.1 Turbine and domain geometries

The blade design is comprised by 2 cylinder and 6 aerofoil profiles, with a maximum twist angle of 13.308º, the detailed distribution of aerodynamic properties along the spanwise direction of the blade is tabulated in Table 4-1 (cross-section profiles of the blade is shown in Figure 4-1).

Table 4-1 Distributed Blade Aerodynamic Properties [52].

y (m)	Chord (m)	Twist (°)	Aerofoil
2.8667	3.542	13.308	Cylinder1
5.6	3.854	13.308	Cylinder1
8.3333	4.167	13.308	Cylinder2
11.75	4.557	13.308	DU40_A17
15.85	4.652	11.48	DU35_A17
19.95	4.458	10.162	DU35_A17
24.05	4.249	9.011	DU30_A17
28.15	4.007	7.795	DU25_A17
32.25	3.748	6.544	DU25_A17
36.35	3.502	5.361	DU21_A17
40.45	3.256	4.188	DU21_A17
44.55	3.01	3.125	NACA64_A17
48.65	2.764	2.319	NACA64_A17
52.75	2.518	1.526	NACA64_A17
56.1667	2.313	0.863	NACA64_A17
58.9	2.086	0.37	NACA64_A17
61.6333	1.419	0.106	NACA64_A17

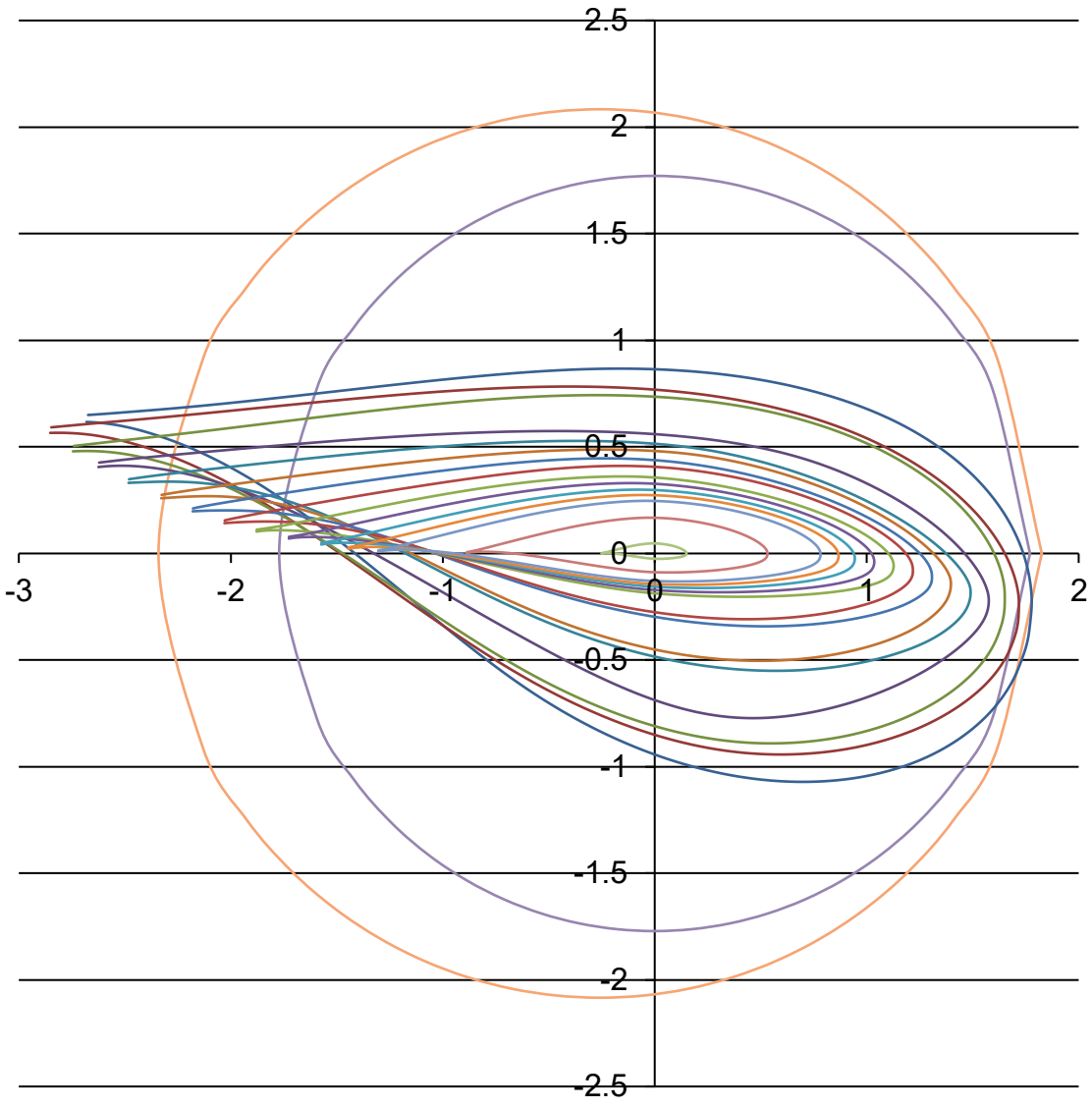

Figure 4-1 Cross-section profiles of the blade are represented in a Cartesian frame and superimposed one over the others.

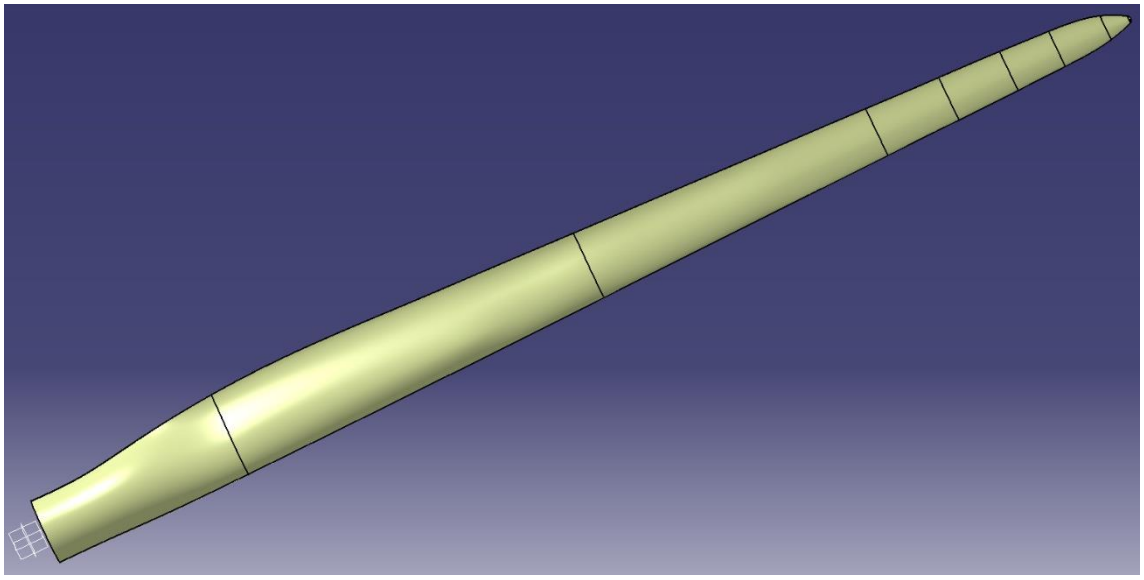

Figure 4-2 Pressure side view.

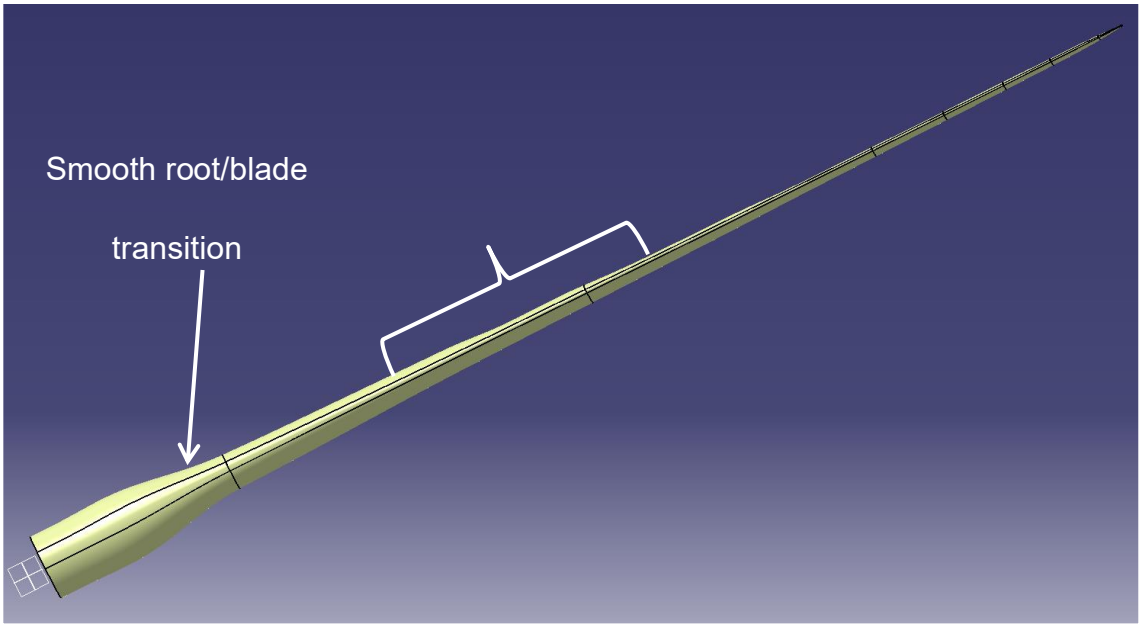

Figure 4-3 Leading edge view.

Based on the original design outline, the 3D CAD model of the blade was built in 8 difference sections (Figure 4-2), the body of each sections was interpolation of two known airfoil cross sections. As it was mentioned above, the overall 3D wind turbine construction follows Resor's proposal [131], however, a few liberties were taken, since there is no corresponding geometrical data available. The "Cylinder 2" section is omitted, because it is in fact not an oval shape (not a

perfect cylinder, in the original article the coefficient drag for this section is lower than “Cylinder 1” [52]), this allows us to create a smooth root surface (Figure 4-3). The second DU35 section is also omitted during blade surface generation (Figure 4-3), this is for limiting the “waviness” typical of the original design, this has also been mentioned by Resor [131].

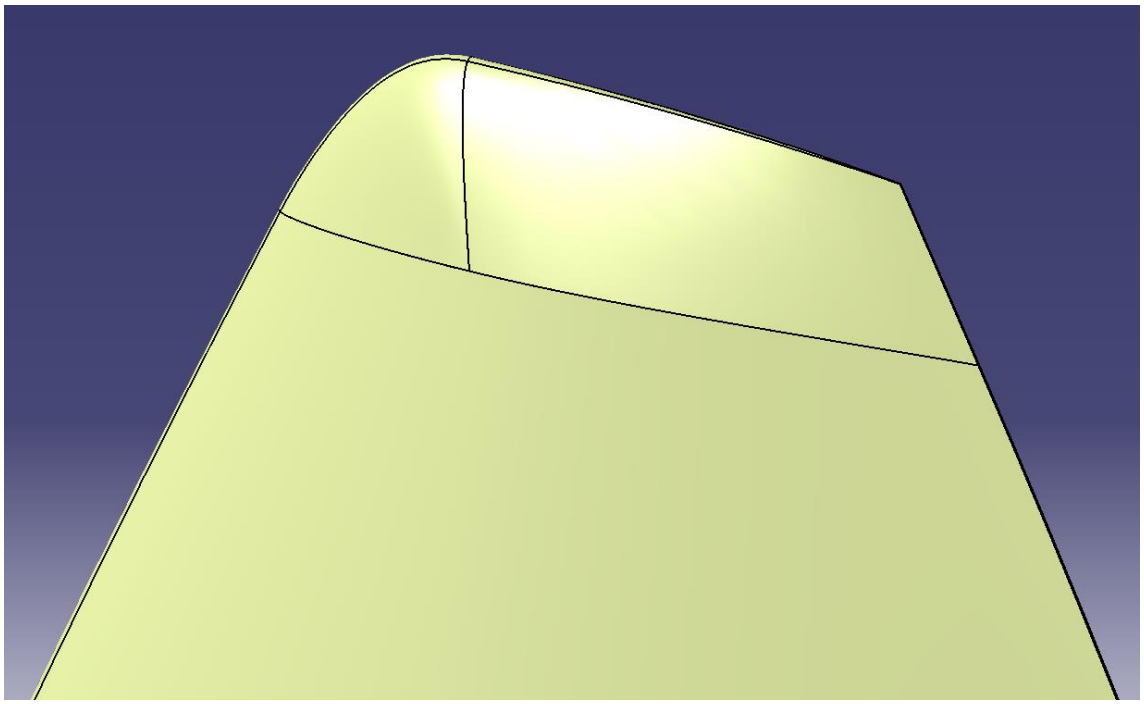

Figure 4-4 Rounded tip shape of the blade.

The last cross section of the blade is defined at $R = 61.6333m$ [52], the section beyond this point is left undefined. In this study, a simple rounded shape design was applied from $R = 62.9m$ to $R = 63m$, shown in Figure 4-4.

The original report stated the turbine tower base diameter is 6m and the top diameter (at 87.6m the nacelle and tower interaction) is 3.87m [52]. To simplify the 3D modelling and meshing process, we use a slightly narrower design in this case. The base diameter is still 6m, but the top is 3m at 90m height (which is inside the nacelle) (Figure 4-5). With this design the tower diameter at the nacelle and tower interaction is 3.14m.

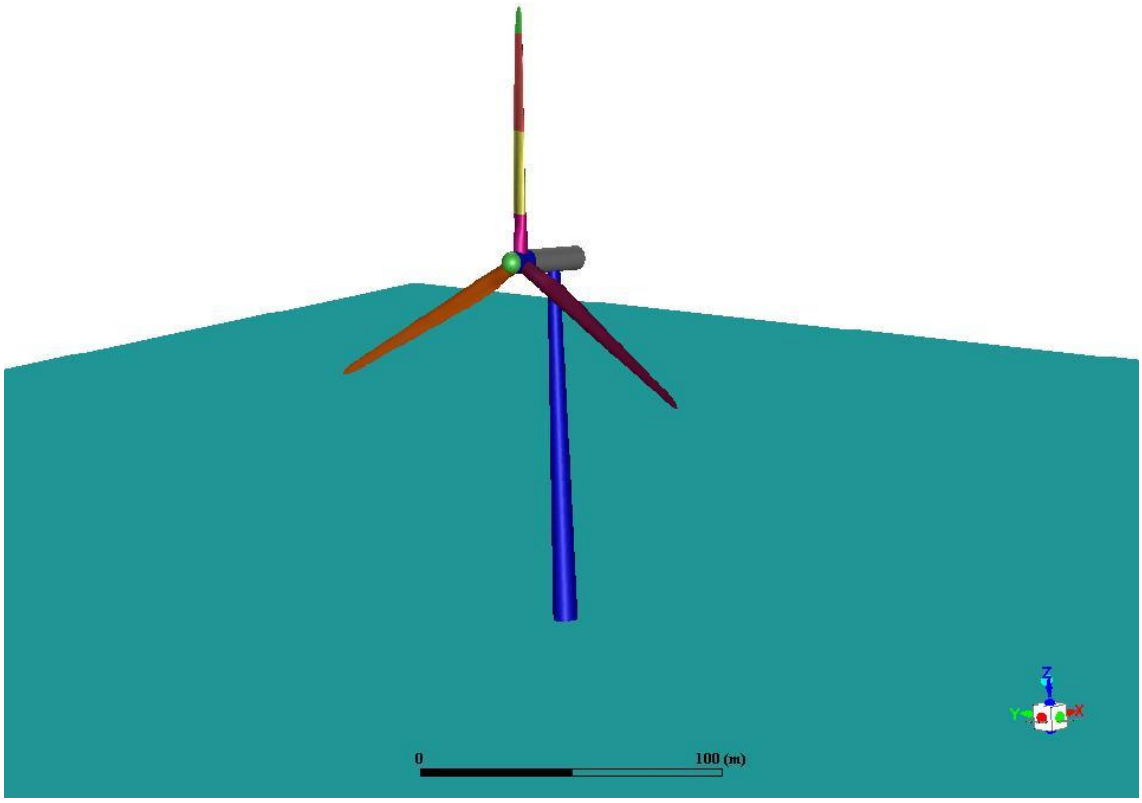

Figure 4-5 Full turbine assembly in FLUENT.

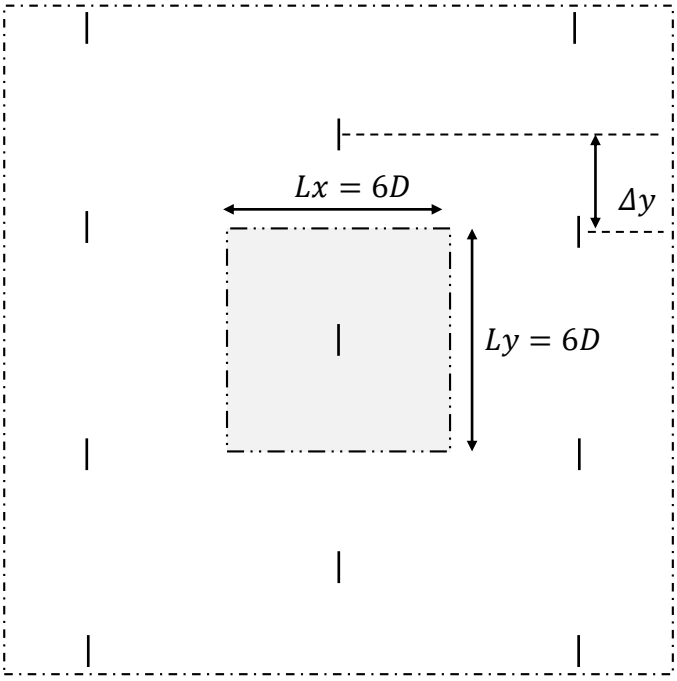

Figure 4-6 Staggered turbine array.

Furthermore, there will be two research directions during simulation stage: one is fully staggered wind farm modelling (Figure 4-6), using single rotor with periodic conditions; the other one is single wind turbine simulation, primarily for rotor validation purpose. The wind farm modelling requires a relatively small domain, in this case $L_x = L_y = 6D$ (Figure 4-6) and $L_z = 8D$, to represent reasonable turbine spacing within a wind farm. On the other hand, single turbine modelling will need much larger domain size, to reduce boundary condition effect. Therefore, the mesh is divided into three parts (shown in Figure 4-7), a rotating cylindrical shape sub-domain (diameter is $1.1D$ and thickness is $0.079D$ (10 m)) that contains three blades and hub body, a box shape mid domain ($6D \times 6D \times 8D$) that includes hub nose and nacelle and a larger box shape outer domain ($40D \times 40D \times 8D$).

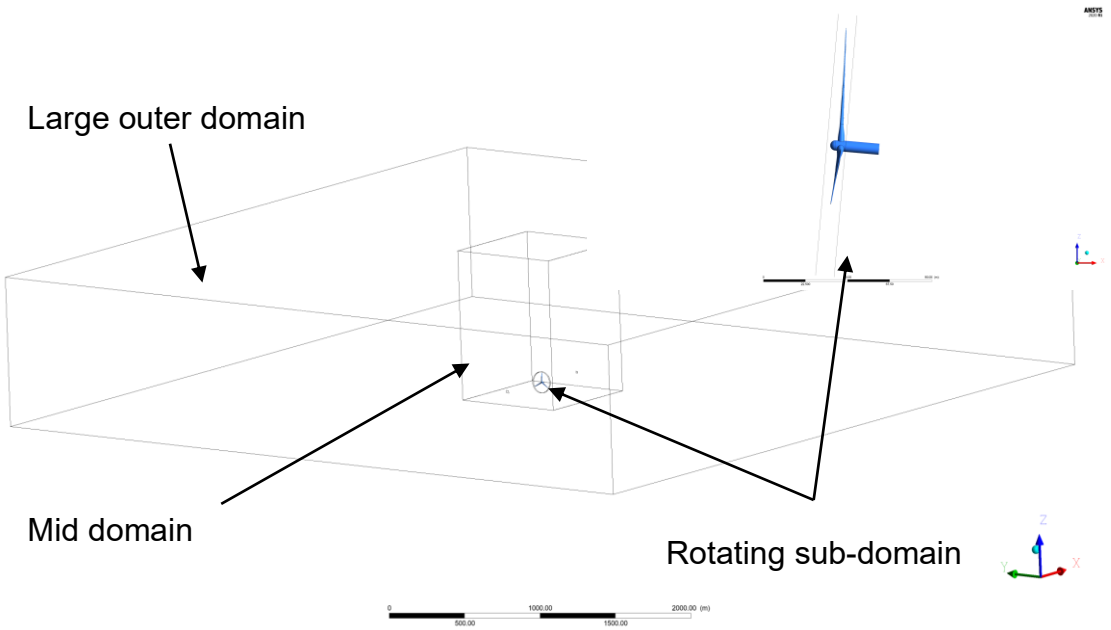

Figure 4-7 Domain size and rotor position.

For the purpose of this study, the boundary layer around the blades and tower will be resolved, but wall function will be applied on the hub and nacelle in order to reduce total number of cells. In addition, the bottom surface of the domain will initially be treated as symmetry (for single turbine case), however, for farm simulation, wall boundary condition with specific roughness height will be

applied on the bottom surface (representing real ground or sea surface conditions) [107] [132]. Therefore, the bottom surface is treated as solid wall during this meshing stage. In general, y^+ value determines whether wall function is applied or not [44], for resolved boundary layer y^+ should be close to 1 and no larger than 3, and for wall function y^+ should be between 30 and 300. Based on these pre-set conditions, the Reynolds number, targeting y^+ value and estimated initial wall normal spacing corresponding to each part of the turbine are tabulated in Table 4-2.

Table 4-2 Initial estimate of Re, y^+ and wall normal spacing (ρ = 1.225 kg/m^3 and μ = 1.838x10^{-5} kg/m·s).

	Re	Targeting y^+	Wall normal spacing (m)
Blade (at 4.652 m chord length)	6.20×10^6	~1	$\leq 2 \times 10^{-5}$
Blade (at 1.419 m chord length)	7.57×10^6	~1	$\leq 1 \times 10^{-5}$
Hub and nacelle (approximately 25 m long)	1.9×10^7	30< y^+ >300	$> 1.0 \times 10^{-3}$
Tower (average diameter 3m)	2.7×10^6	~1	$\sim 3.0 \times 10^{-5}$
Bottom surface (40D)	3.83×10^9	30< y^+ >300	$> 1.7 \times 10^{-3}$

4.2.2.1 Rotor only

The upstream side of the rotor domain has been depressed in the centre (Figure 4-8 (a)), which gives a more tailored fit to the rotor design. Surface mesh of the blades is created on one blade with O-grid topology (the multi-colour blade in Figure 4-8 (b)), then copied on to the other two remaining blades. The blade has been split into 4 parts: root, two middle sections and tip (based on aerofoil profile distribution).

The hub is relatively simple to mesh, since it is basically a cylinder shape with three holes that connect with the blades. There are 399 nodes along the

circumference direction and 70 nodes to cover the cylinder length. Particular attention is applied on the connecting area where the hub meets the blade (with smallest spacing of 8×10^{-5}), as well as the area in between the blades (Figure 4-9).

There are in total 111 nodes on the spanwise direction along the blade, with the same 1.2 growth rate applied slightly differently with each section. The root section is approximately 10m long with 34 nodes, the smallest and largest spacing are 0.001 (next to the hub) and 0.5 respectively (Figure 4-10). The two middle parts are treated as single section, the length is approximately 44.5m combined and with 32 nodes in total. In order to keep a good continuity, the smallest spacing is 0.5m and the size of the largest cell is 1.3m. The tip section of the blade is 6.9m long with 45 nodes, the smallest cell (0.0015) is at the end, where refined mesh is needed to represent an accurate and smooth shape.

On the chordwise direction, 190 nodes are distributed into 4 sections around the blade, which are upper surface, lower surface, leading edge and trailing edge. Both upper and lower surface are allocated with 65 nodes, the smallest and largest cell spacing vary depending on the spanwise location on the blade. In addition, the first growth rate (from leading edge towards trailing edge) of 1.2 and opposite direction second growth rate of 1.03 are applied on most of the sections of blade on spanwise direction, apart from the tip end of the blade where 1.2 is applied on both growth rate, since the size of the geometry is considerably smaller than the blade root. The leading and trailing edge each has 30 evenly distributed nodes along their surfaces, that smooth surface has been captured.

The volume mesh is process primarily based on the initial calculation in Table 4-2 to ensure $y+ \sim 1$ around the blades (Figure 4-11 and Figure 4-12). This gives 6.06×10^{6} cells in this rotor domain.

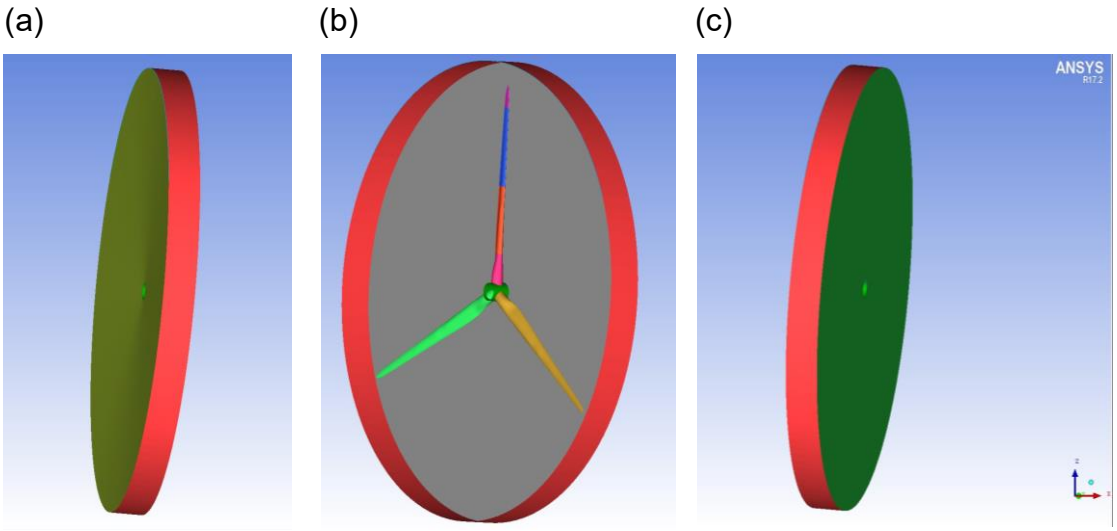

Figure 4-8 Rotor domain shape outline, (a) shows the upstream, (b) shows the rotor and hub positioning in the domain face and (c) show the downstream face.

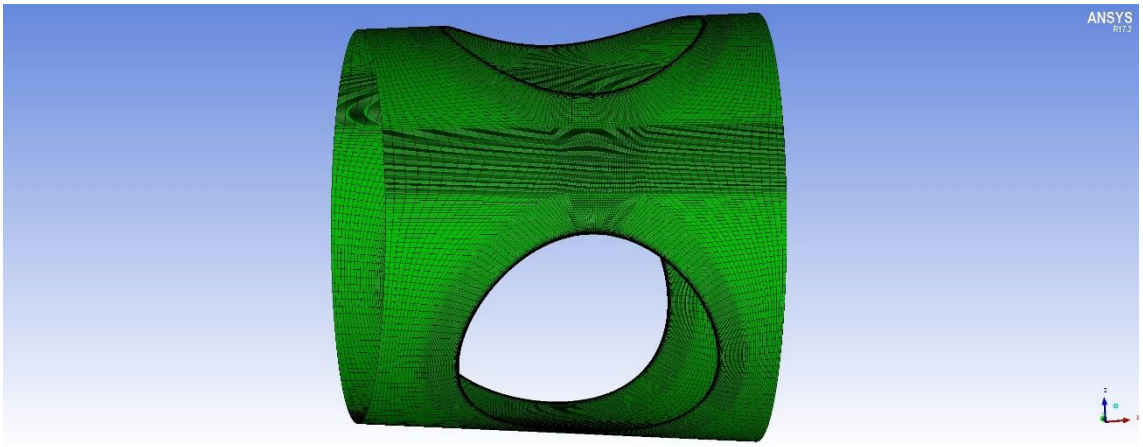

Figure 4-9. Hub mesh.

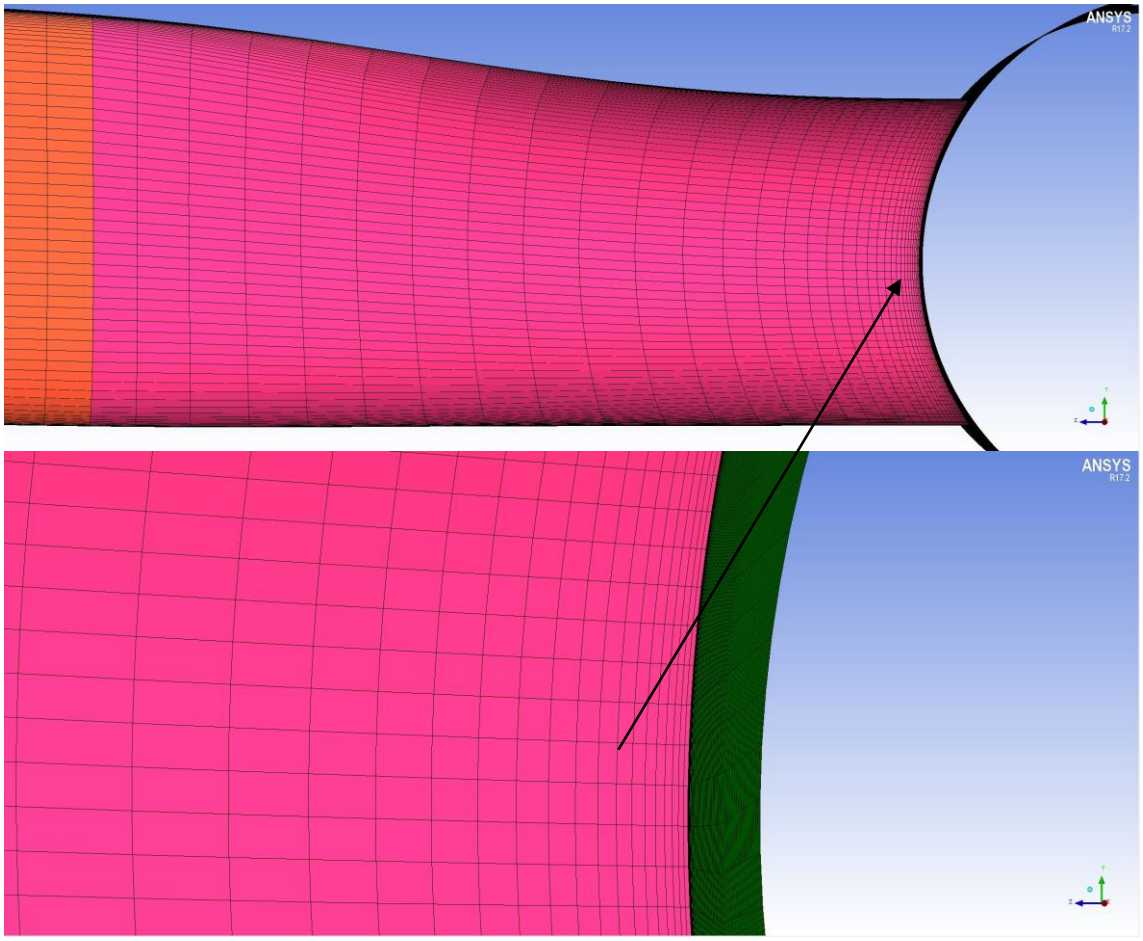

Figure 4-10 Blade root section, cell distribution on spanwise direction.

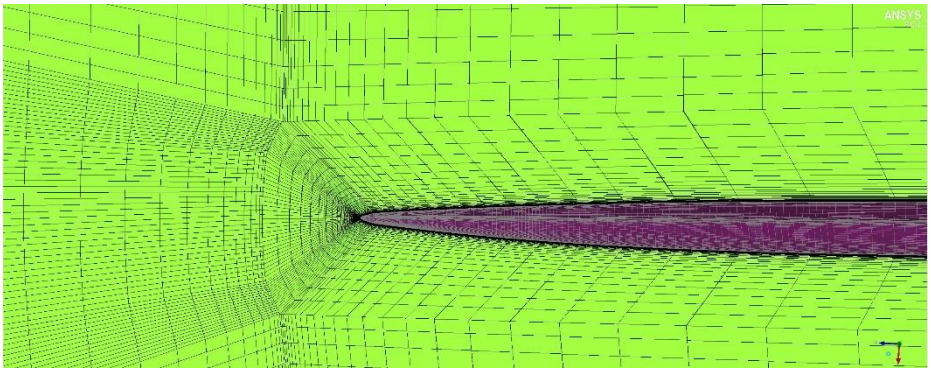

Figure 4-11 Cross-section view (xz plane), at blade tip.

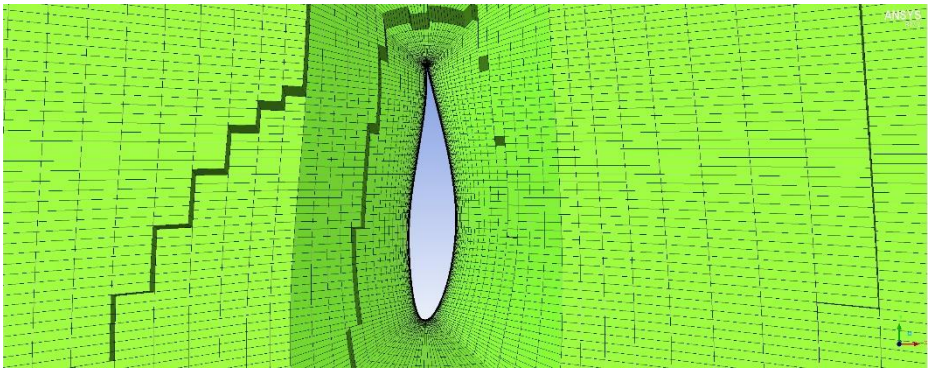

Figure 4-12 Cross-section view (xy plane), close to blade tip.

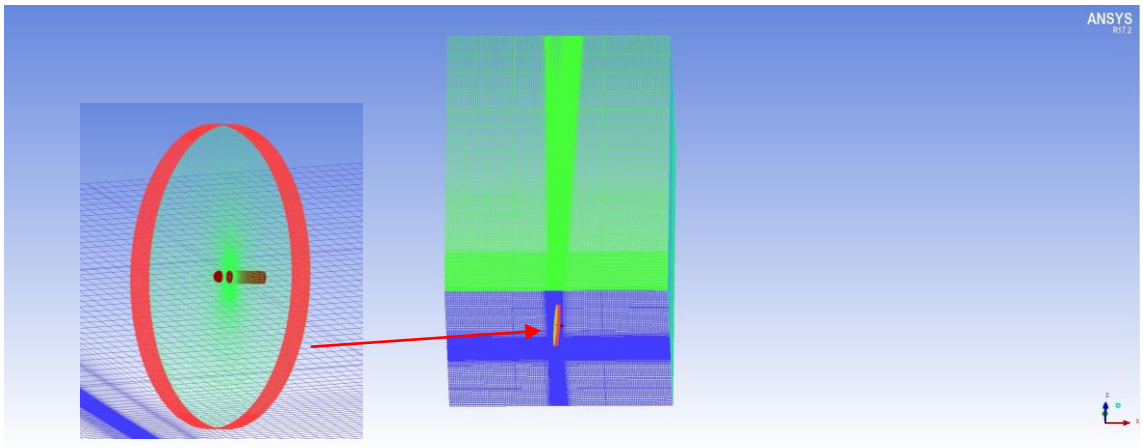

Figure 4-13 Mid domain outline.

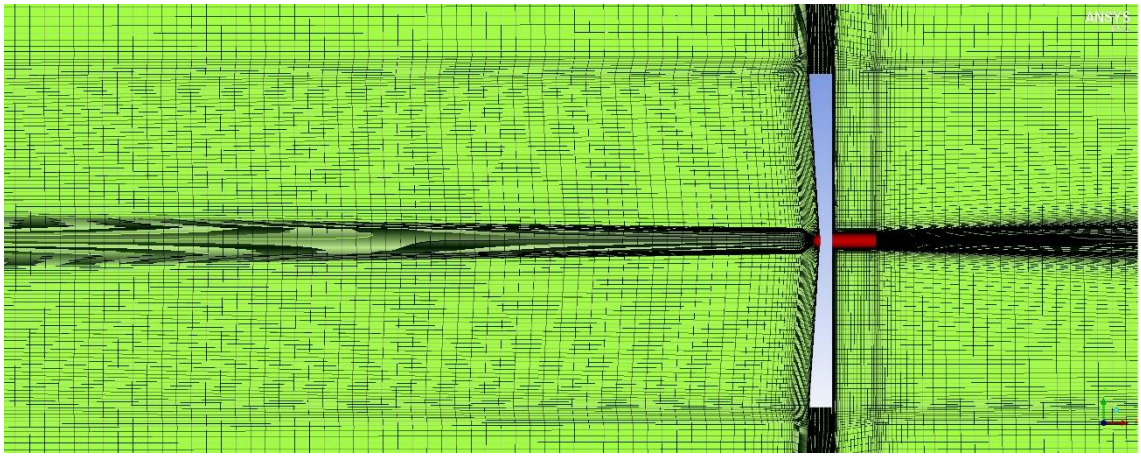

Figure 4-14 Cross-section view of the mid domain, xy plane across hub centre.

The two outer domains are relatively more straight forward to mesh since they do not contain complex geometry. The basic layout and overall mesh distribution of the mid domain is shown in Figure 4-13, as mentioned earlier in

this chapter, the hub nose and nacelle are modelled within this domain (since they are not rotating), a hollow disc shape is also built in that contains the rotor domain. The concentrated cell groups on the streamwise and spanwise direction, which can be seen in Figure 4-14, are especially designed to capture accurate and correct turbine wake characteristics. Moreover, since the bottom surface of the domain will be modelled as solid ground or sea surface for wind farm modelling, (it will be treated as symmetry during single turbine simulation), the first cell above the bottom surface is 1 m and with 1.2 growth ratio. In addition, the shape of cell distribution along the rotating axis is also especially designed (Figure 4-15), in order to match with the rotating domain geometry. The total number of cell in this domain is 6.9×10^6.

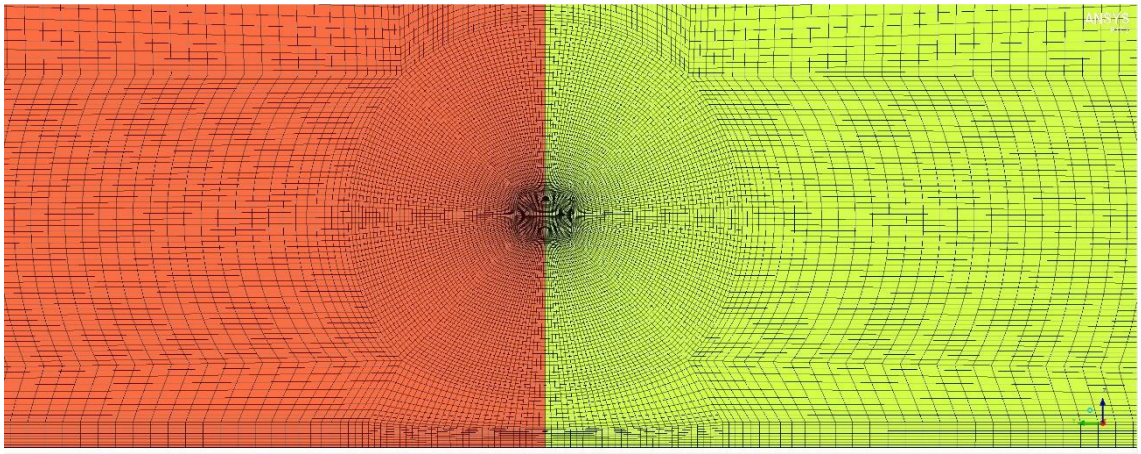

Figure 4-15 upstream surface of the mid domain.

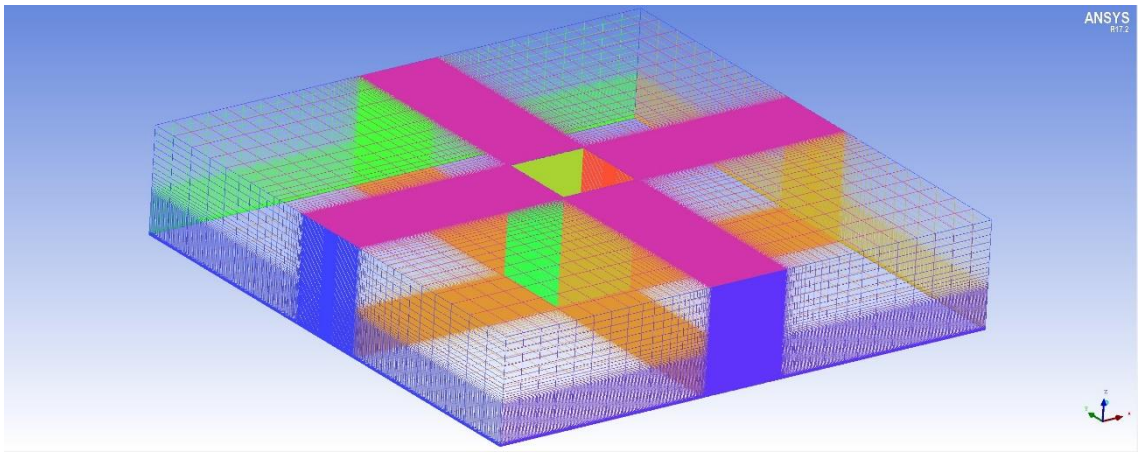

Figure 4-16 Large outer domain.

Finally, the large outer domain is the simplest one amount the three. The main idea is to keep the cell distribution on the interface area the same between the mid and large outer domain, which can reduce calculation time and errors during simulation. The cell spacing is then gradually increased toward the edge of the domain (Figure 4-16), with largest cell size of 265 m at the upper corners. Combining the two box shape domains, there are 8.87×10^6 cells in total.

4.2.2.2 Adding tower

The full turbine (with tower) is created separately after the rotor only mesh. An O-grid partition is created within the mid domain that based on the tower geometry. The node distribution on the tower surface is relatively straightforward, it is mostly determined by the existing surface mesh of the nacelle (Figure 4-17) and ground. Near to the tower bottom, the height of the 1st cell above ground has been reduced slightly, for better consistence and keeping reasonable cell aspect ratios.

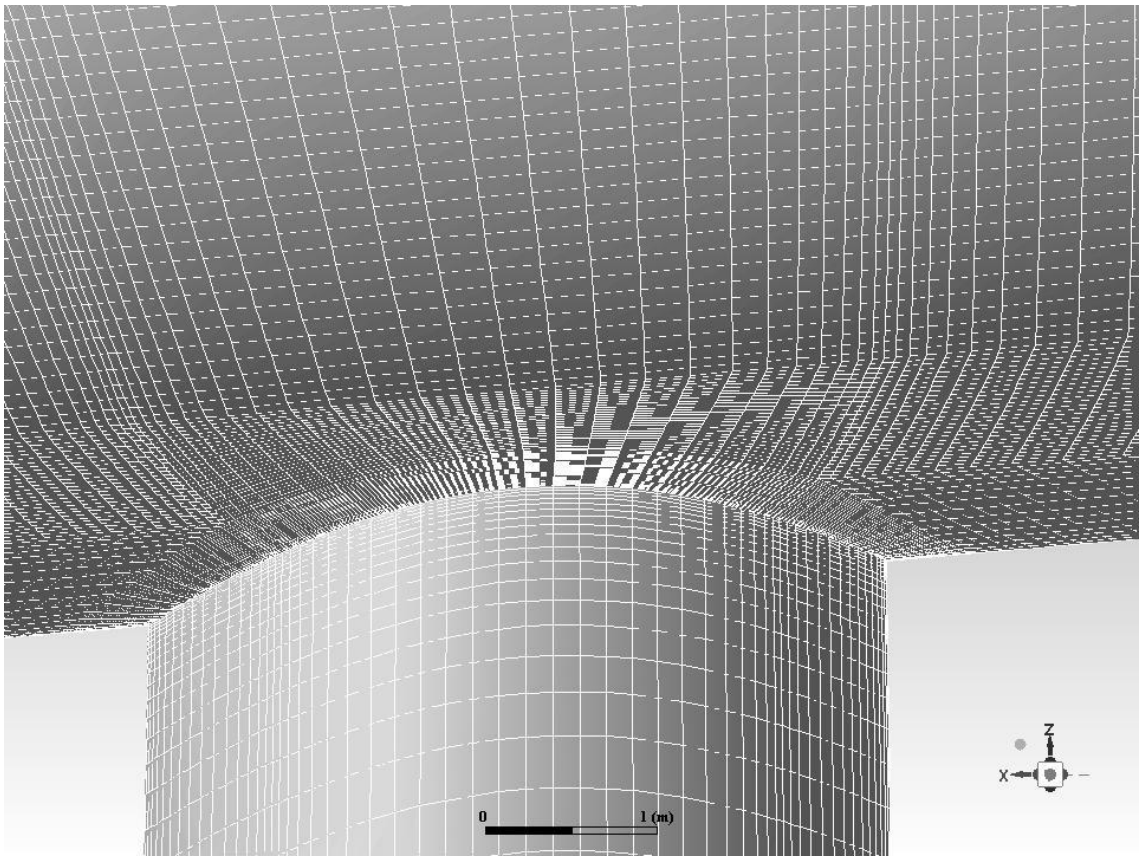

Figure 4-17 Nacelle and tower intersection mesh details.

A mesh quality check is performed using ICEM, with two common quality criterions: Angle and Determinant 2×2×2. Due to the fact that the large outer domain has very simple cell distribution shape, therefore, this check is only carried out with the rotor and mid domain. For time saving purpose, only the non-tower mid domain has been tested. Both domains have shown reasonable minimum Determinant 2×2×2 values, that are around 0.6. However, both domains have cell angles that are smaller than 45° shown in Figure 4-18 and Figure 4-19, which is almost unavoidable for complex geometry meshing. Although, the quantity of the elements, that have small cell angles, is relatively small and all located around expected areas.

4.2.2.3 Mesh quality checking (rotor only)

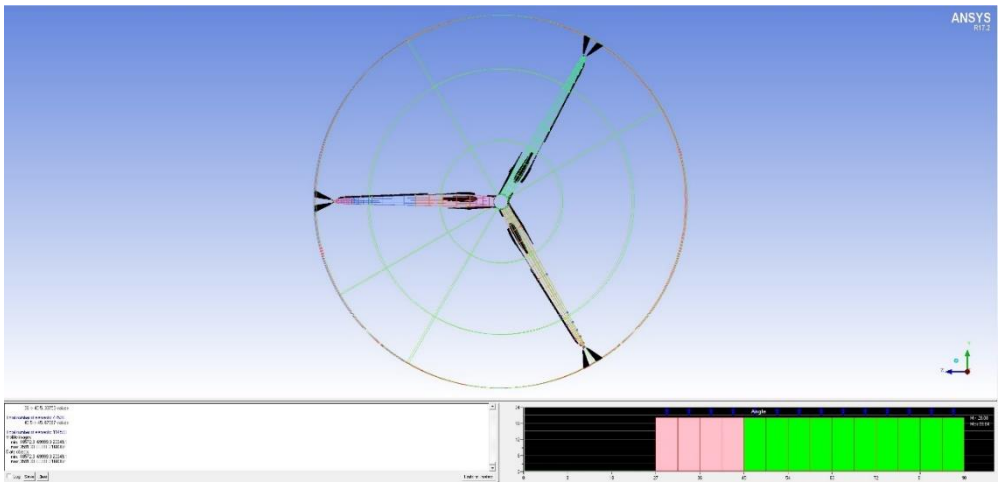

Figure 4-18 Rotor domain cells that has angle smaller than 45.

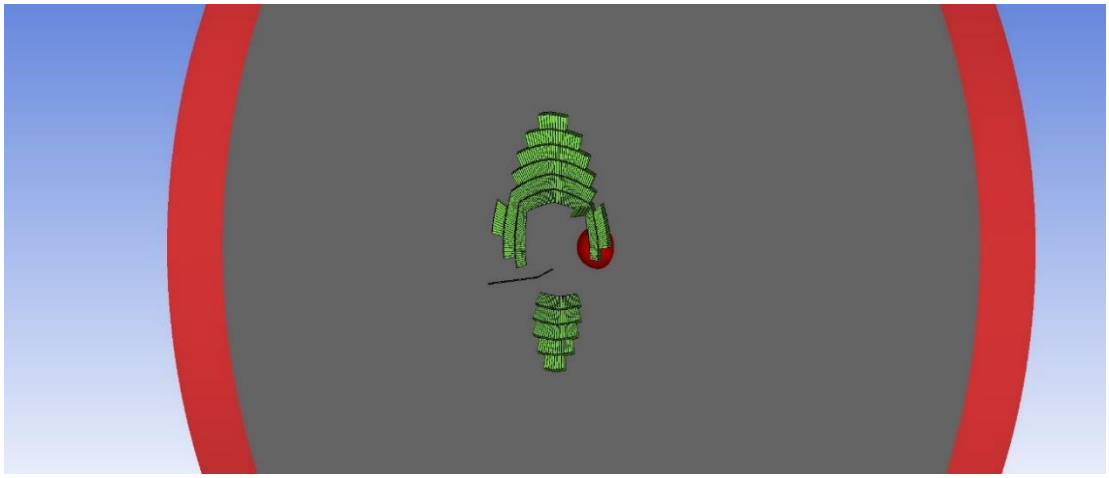

Figure 4-19 Mid domain cells that have angle smaller than 45.

A single turbine URANS simulation, as a testing case, has been carried out, with the same boundary and initial conditions described earlier. The simulation has been run for 5 rotor revolutions; this is not enough to achieve convergence for all results, however, should be adequate to check y^+ distribution along the blade. As shown in Figure 4-20, the y^+ value is around 1 mostly around the blade surface, although, there is a small area at the tip of the blade, where y^+ is close to 3, according to FLUENT manual [44], this is still acceptable for URANS simulation. Although it was infeasible to conduct a mesh sensitivity study for the entire rotor, we carefully designed the blade-surface mesh based on the results of existing mesh sensitivity studies in the literature. For example, a recent 120 study shows that for a NACA 64-618 aerofoil profile, under similar flow conditions, grid independence can be achieved when the total node number is above 180 around the aerofoil [133].

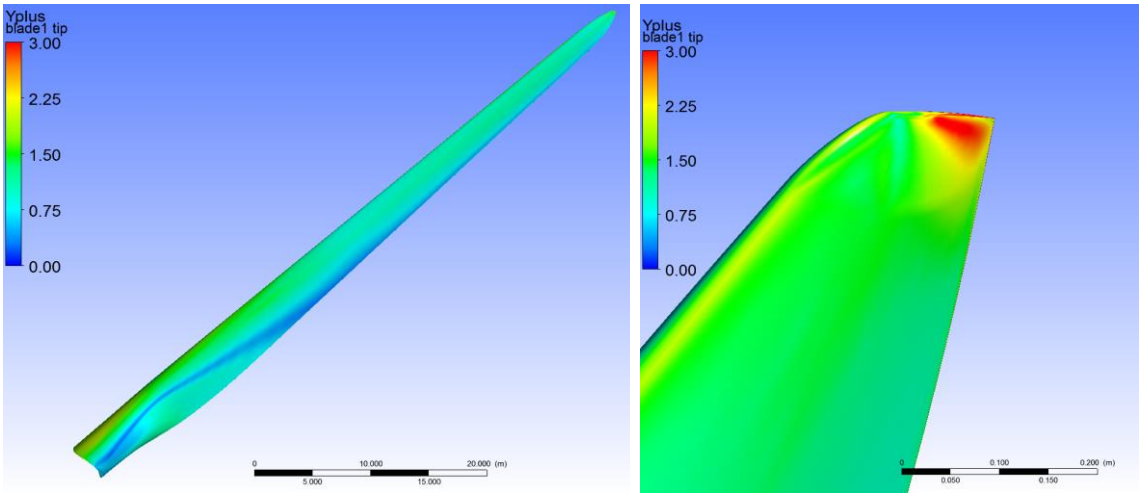

Figure 4-20 y^+ value on one of the blades.

4.2.3 Turbulence model analysis

The purpose of this task is to perform a turbulence model comparison study between $k-\omega$ SST and $k-\varepsilon$ standard, for a fully resolved (FR) single wind turbine simulation. It was considered as the most efficient configuration to assess the difference between the 2 turbulence models, only the rotor is modelled in this case, but the full turbine structure (including tower) will be added at latter stage. Even though, the majority of the similar studies have

suggested the $k-\omega$ SST is the preferable turbulence model, for the purpose of this current research, $k-\varepsilon$ Standard turbulence model is also tested to compare with $k-\omega$ SST.

4.2.4 Simulation setup

The basic fluid (air in this case) properties have been kept as FLUENT default values, for both single turbine and farm simulation, that the density and viscosity are $\rho = 1.225kg/m3$ and $\mu = 1.7894 \times 10^{-5} kg/(ms)$ respectively. The surfaces of the entire turbine (blades, hub, nacelle and tower) are treated as smooth non slippery wall. As mentioned previously, here the rotating motion is modelled using sliding mesh method, therefore, the “Mesh Motion” is selected in FLUENT for the rotor cell zone. The rotation axis origin and direction are carefully adjusted to align with the actual turbine geometry.

4.2.4.1 Single turbine

The purpose of single turbine simulation is to validate the accuracy of the 3D turbine and test various turbulence models against the original data in [52], therefore boundary conditions are as close to the original report as possible. A uniform wind speed $U_\infty = 11.4m/s$ is applied at the inlet surface and pressure outlet is set as the outlet condition, both of the side walls on the outer domain as well as top and bottom surface are defined as symmetry. In addition, all interfaces between three domains are connected using ‘Matching’ function in Fluent [44]. The rotating speed is 12.1rpm (which translated to 1.2671rad/s in Fluent settings). Following the suggestions in the previous studies [129] [107], the time step corresponds to the rotor azimuthal angle $\Delta\theta = 0.5°$ ($\Delta t = 0.00689s$ in this case) and 15 iterations per time step. The simulations have been run for 5760 time-steps, which is exactly 8 revolutions in simulation time. For time-saving purpose and according to the previous study [107], 8 revolutions of simulation should be sufficiently long for this type of study. In order to initialise the simulation smoothly, the first revolution (720 time-steps) uses first order upwind spatial discretisation for momentum, TKE and specific dissipation rate, the rest 7 revolutions are all calculated using a second order

upwind method. The results obtained at the 8th revolution are taken for this turbulence comparison study.

4.2.4.2 Farm simulation

The farm simulation set up is mostly the same to the previous study by Delafin [107], the only difference is the presence of a fully resolved turbine tower. The idea is to create a wind farm environment instead of an isolated single turbine scenario, only the smaller outer domain ($6D \times 6D \times 8D$) is used in this case. We use the same strategy described in Chapter 3 to achieve the fully staggered wind farm layout. The inlet and outlet periodic interfaces have been split vertically into two parts, where the right inlet is connected to the left outlet and vice versa. The side boundaries are set as periodic interfaces as well, therefore, we have created an infinitely large wind farm. The bottom boundary is set as 'wall' in this case, with a nominal roughness height $K_s = 1m$, and the empirical constant E and roughness constant C_s values are kept as 9.793 and 0.5 respectively. The tope boundary is the same as single turbine case, which is 'symmetry'.

The rotational speed of the rotor for farm simulation is not very straightforward. The flow profile in the fully developed farm boundary layer is not known a priori, this means that the exact wind velocity at hub height is unknown. This is a key aspect to match the tip speed ratio (TSR) used in the original report [52]. To solve this issue, a few actuator disc (AD) simulations (rotor only, no tower) (RANS with $k-\omega$ SST) were conducted by Delafin (2017) prior to this current study.

The basic geometry of the AD was carefully matched with the fully resolved NREL 5MW model. Different K values for the disc had been tested to obtain C_T as close as possible to initial FR turbine simulation during Delafin's investigation in 2017 [107], the most appropriate value was found to be $K = 1.2825$ with a corresponding average wind speed across the AD $U_T = 8.666\, m/s$ (U_T is the area-averaged velocity across the AD). These tests were conducted under the same flow conditions described in the single turbine case of this study as well as in [52].

The AD model was then placed in a farm simulation ($6D \times 6D \times 8D$ domain size). Firstly, the same 'empty box' simulation described in previous chapters was also employed here, this is to generate the undisturbed fully developed farm boundary layer. This simulation was run with $K_s = 1m$ with a constant mass flow rate. A power-law velocity profile (with an exponent of 0.1) with reference wind speed $U_{ref} = 15\,m/s$ at $z = 90m$ (hub level) was adopted to calculate the constant mass flow rate, which gave a result of $16.528 \times 10^6\,kg/m^3$ [107]. Once again, the purpose of the 'empty box' simulation was to obtain the background pressure gradient inside the domain (refers to the original two-scale momentum model [22]), the result was $-7.49 \times 10^{-4}\,Pa/m$. The AD farm simulation was then carried out using this pressure gradient and gave $U_T = 5.517\,m/s$, in addition, the simulation process was identical to section 3.3.1.

We used a simple proportional relationship between rotor rpm and AD U_T values to determine the appropriate rotational speed for the farm simulation, which is essentially derived from C_T matching to the original specification [52]:

$$\frac{RPM_{single}}{RPM_{farm}} = \frac{U_{T_{single}}}{U_{T_{farm}}} \rightarrow \frac{12.1rpm}{RPM_{farm}} = \frac{8.666m/s}{5.517m/s} \rightarrow RPM_{farm} = 7.703rpm\,(0.806656\,rad/s).$$

Once the rotational speed is determined, the simulation time step is set as $\Delta t = 0.0108s$ (again this corresponds to rotor azimuthal angle $\Delta\theta = 0.5°$) and 15 iterations per time step. One point should be noted here, this rotational speed is FR rotor (without tower). Adding tower to the model would reduce the average wind speed within the wind farm. The rotational speed might need to be slightly altered after adding tower, in order to match the same TSR with the rotor only case. Although, we are not expecting significant wind speed reduction in this case, therefore, we are using the same rotational speed for both 'tower' and 'no tower' cases.

Due to the high level of complexity of the periodic farm simulation, it would be very expensive to generate a fully developed farm boundary layer by only using

the pressure gradient. Therefore, the flow calculated in AD farm simulation is applied as the initial flow condition for the FR simulations. The rotor sub-domain. Both farm simulations (with and without tower) have been run for 100 revolutions, under URANS with appropriate turbulence model (which is determined by the turbulence model analysis results shown in later section of this chapter). Then an additional 18 revolutions of time-averaged simulation have been carried out, for generating comparable results to the theoretical model [132]. The number of revolutions for time-averaged simulation will be explained in the results section of this chapter.

The fully structured mesh for the FR model was initially created for RANS initially. Even though, the mesh quality should be adequate for DES, to avoid any potential issue with RANS to LES transition DDES is used in this case. All model constants are left as default values in FLUENT [44], the turbulence model for the RANS region is kept the same as URANS case, as well as all boundary conditions. The viscous model is switched from RANS to DDES after the first 100 revolutions.

4.2.5 Calculations for CFD data processing

One thing should be pointed out is that FLUENT uses a reference velocity value [44] to calculate coefficient values during simulation, by default this value is generated based on the initial flow conditions. In a simple input-output simulation (which is the single turbine simulations in this case) this reference value is correct, it represents the far field upstream velocity. However, for fully periodic farm simulations, this reference value is no longer appropriate, because the velocity changes away from the initial value. Therefore, for wind farm data the coefficient values recorded during simulation will need to be "corrected" by using appropriate wind velocity value.

The momentum coefficient of each blade is recorded during simulation, the moment centre and axis are set as the hub centre and rotating axis respectively. The total rotor momentum coefficient is obtained by simply adding the momentum coefficient of each blade together, the torque of the rotor can then be calculated as:

Equation 4-1

$$\tau = C_m \frac{1}{2} \rho A r V_{refe}^2$$

where C_m is rotor torque coefficient, ρ is air density (1.225kg/m^3), A is the swept area of the rotor ($A = \pi r^2$), r is the radius of the rotor (63m) and V_{refe} is the reference upstream wind velocity (6m/s for farm simulations and 11.4m/s for isolated turbine simulation). The reference wind velocity is the value FLUENT used to calculate C_m, it is generated by initial flow conditions [44]. To calculate the power output of the rotor:

Equation 4-2

$$P = \tau \cdot \omega$$

where ω is the rotational speed of the turbine (0.80666rad/s for farm simulations and 1.267rad/s for isolated turbine simulation). The drag coefficient has also been recorded for each blade; the rotor thrust can be calculated as:

Equation 4-3

$$T = C_d \frac{1}{2} \rho A V_{refe}^2$$

The power and thrust coefficient of the rotor can then be calculated as: $C_T = \frac{P}{\frac{1}{2}\rho A U_{F0}^3}$ and $C_T = \frac{T}{\frac{1}{2}\rho A U_{F0}^2}$, where U_{F0} is 14.9m/s and 11.4m/s for farm simulations and isolated turbine simulation respectively.

4.3 Results and Discussions

4.3.1 Turbulence model comparison

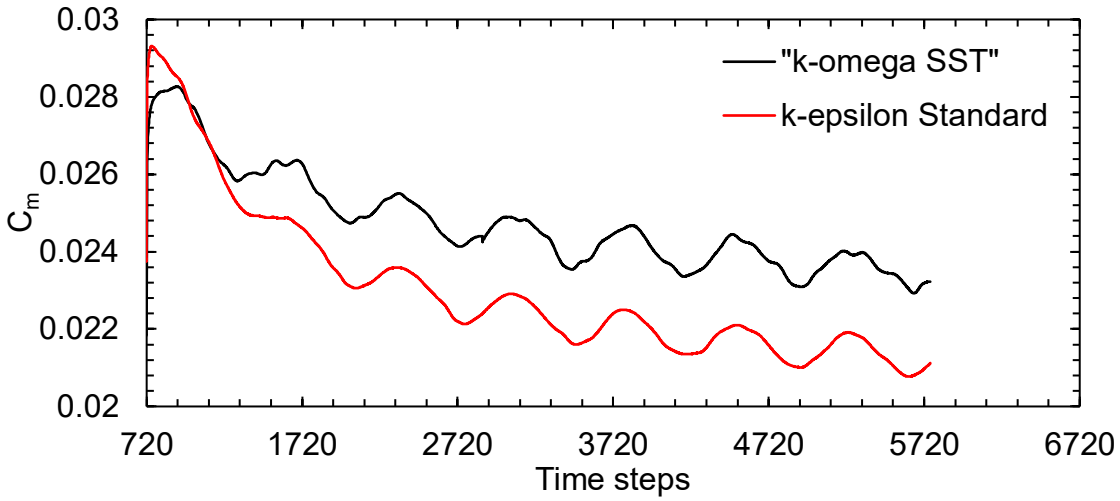

Figure 4-21 Time-history of C_m for one blade.

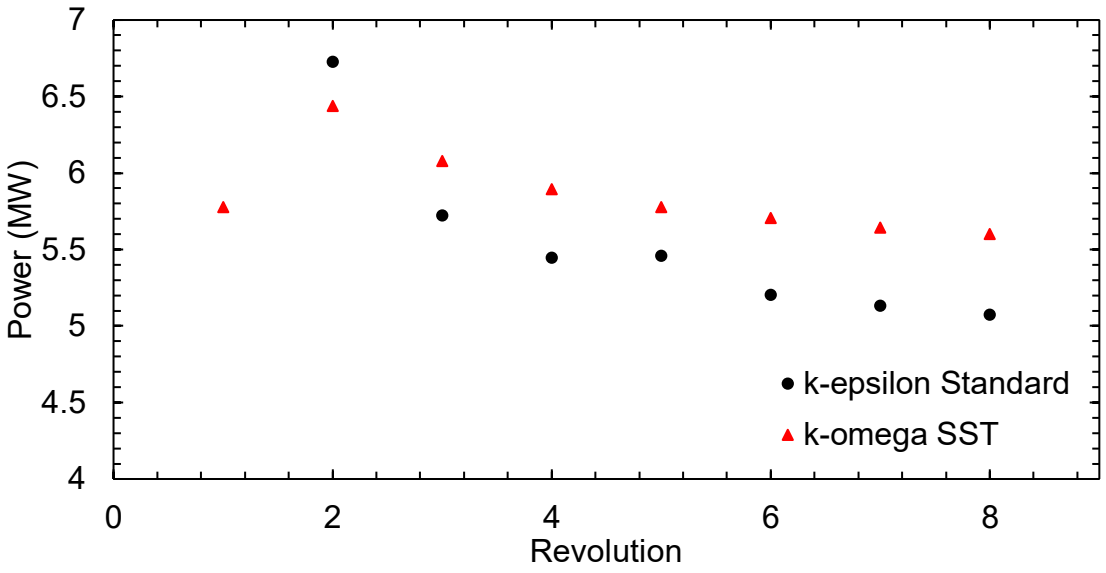

Figure 4-22 Power output over number of revolutions.

For result convergent check, the momentum coefficient for one of the three blades is taken as an example. Since the first 720 time steps (first revolution) are for initialising the simulation, the time-history shown in Figure 4-21 is starting after 720 time step. Due to both cases are URANS and the blade is travelling at different locations when it is rotating, a completely steady result is not expected, instead the result should reach a steady oscillating state. After

approximately 3000 time steps, both of the C_m plots starts to level, although, the results may seem still decreasing at a very small rate after the completion of 8 revolutions, the gap between the two lines is clearly constant. The purpose of this study is to compare the two different turbulence model, the current results should be sufficient to fulfil the task. The simulations will be extended at later stage together with GCI study, to complete the overall model validation process.

In addition, the power output plot over each revolution is shown in Figure 4-22, that further proves that the results after 8 revolutions appear to be stable enough for this stage. Another point should be noted is that both Figure 4-21and Figure 4-22 suggest that the $k-\varepsilon$ Standard turbulence model is underestimating the turbine performance comparing to $k-\omega$ SST.

Table 4-3 Turbulence model comparison results summery.

	NREL Fast	$k-\omega$ SST	Diff.	$k-\varepsilon$ Standard	Diff.
P (MW)	5.29	5.60	5.86%	5.08	-3.97%
C_p	0.47	0.49	4.26%	0.45	-4.26%

The results for the two turbulence models shown in Table 4-3 are averaged from the last revolution of the simulation, they are then compared with the original data calculated by NREL using FAST (BEM based turbine model) [52]. These results have confirmed that the $k-\varepsilon$ Standard turbulence model is under predicting the power output of the turbine, whereas the $k-\omega$ SST turbulence model is over predicting. In addition, the power output plots in Figure 4-22 show that the results from both turbulence models are still decreasing. This indicates that the $k-\varepsilon$ Standard model would move further away from the NREL Fast value. On the other hand, the $k-\omega$ SST model is moving closer to the NREL Fast prediction. The power coefficient comparison shows that both models have exactly the same magnitude of percentage of difference compared to NREL's data, but in opposite direction. In theory, the current model setup should give a slightly higher power output or C_p than a perfectly isolated turbine, due to the local blockage effect because of the proximity of the bottom boundary [106].

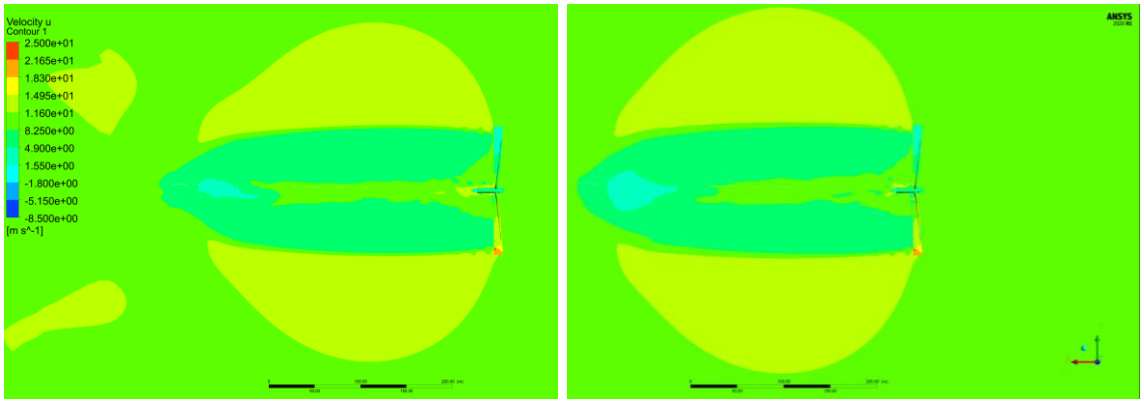

Figure 4-23 Instantaneous (at the last iteration) velocity U (m/s) contour plot, left: $k-\varepsilon$ Standard and right: $k-\omega$ SST.

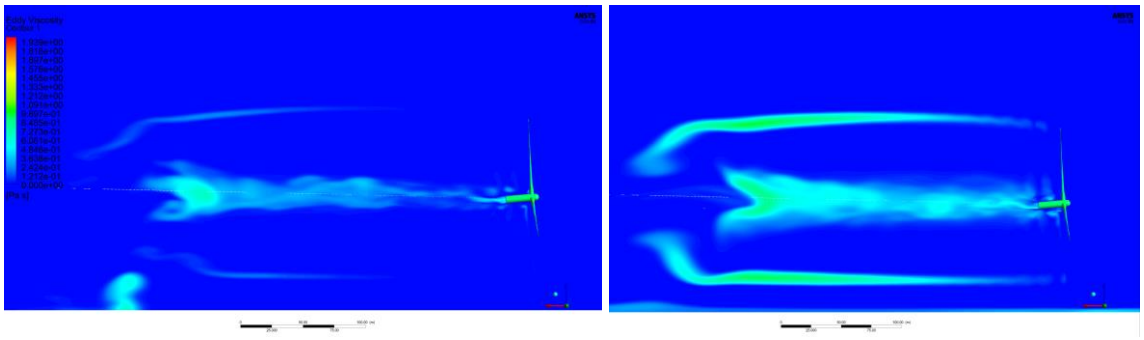

Figure 4-24 Instantaneous (at the last iteration) Eddy Viscosity (Pa·s) contour plot. Left: $k-\varepsilon$ Standard and right: $k-\omega$ SST.

Additionally, the instantaneous velocity U plots in Figure 4-23 shows that the shape of the downstream wake region is similar between the two turbulence models. Moreover, the comparison shown in Figure 4-24 appears that the eddy viscosity within the wake is much smaller for the $k-\varepsilon$ Standard model.

4.3.2 Farm simulations

All farm simulations have been performed on a HPC (High-performance Computing) system, a total of 128 CPU cores are utilised for each simulation. Based on the actual simulation (13 hours per revolution) time and the job scheduling constrains (maximum of 240 hours per job) on the HPC system, each job submission can carry out 18 revolutions of simulation time.

4.3.2.1 URANS

The URANS (with $k-\omega$ SST) have been run for 118 revolutions for both cases ('Tower' and 'No Tower'), 100 revolutions of standard calculations plus 18 revolutions of time-averaged calculations. The simulations were relatively stable during each revolution; there is no obvious blade-scale abnormality; the power output changes depending on the farm-scale wind flow conditions (Figure 4-25). This indicates that the boundary conditions for each blade are acting correctly. The results do not follow the same trend during the first half of the simulation (Figure 4-26), this could be due to the added tower structure causes different flow behaviours from 'No Tower' case. A constant difference between the two plots appears after around 80 revolutions (Figure 4-26). This clearly shows the power reduction by adding turbine tower into the modelling process, in addition It shows the simulations require a long time to stabilise.

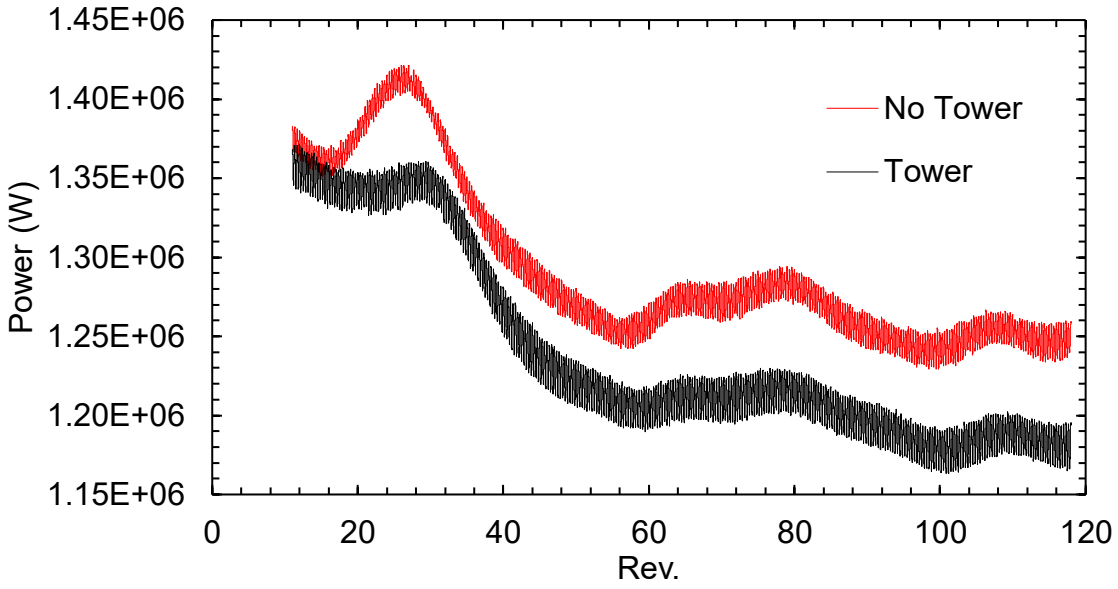

Figure 4-25 Convergence history of instantaneous power output.

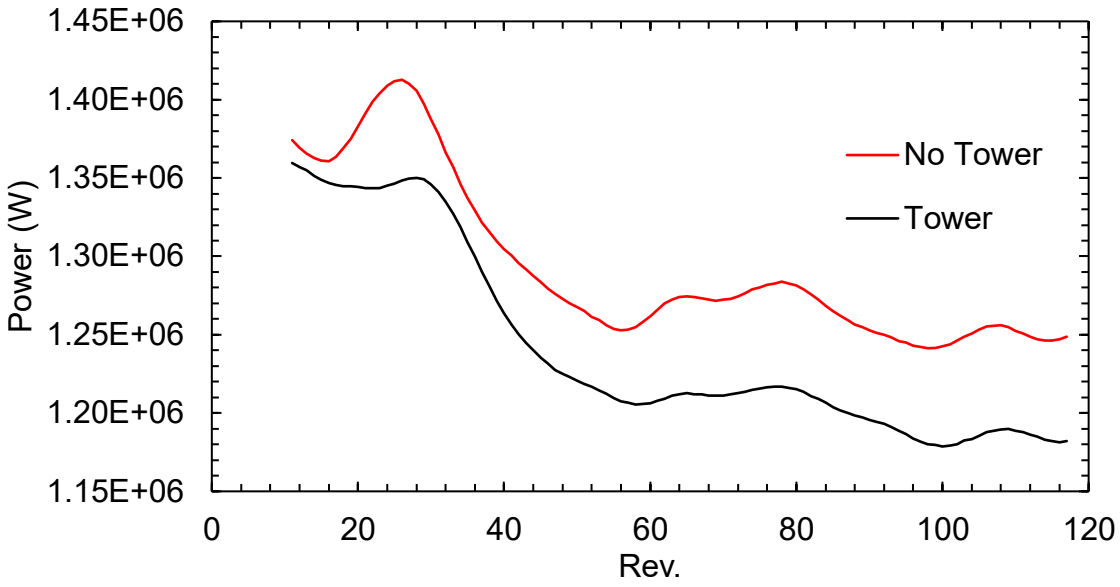

Figure 4-26 Convergence history of revolution-averaged power output.

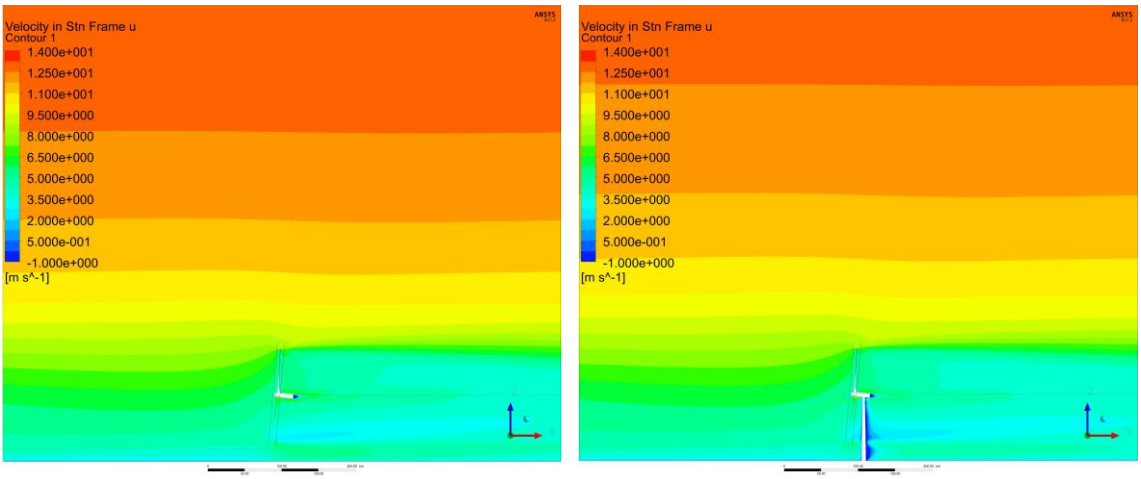

Figure 4-27 Contours of instantaneous streamwise velocity [m/s] at the horizontal centre plane (taken at 100th revolution). Left: no tower, right: with tower.

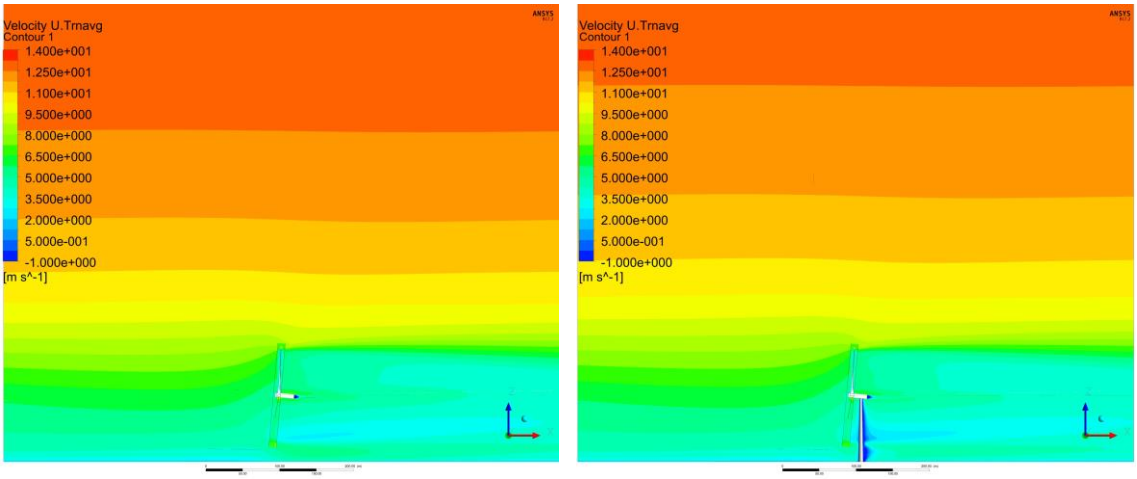

Figure 4-28 Contours of time-averaged streamwise velocity [m/s] at the horizontal centre plane. Left: no tower, right: with tower.

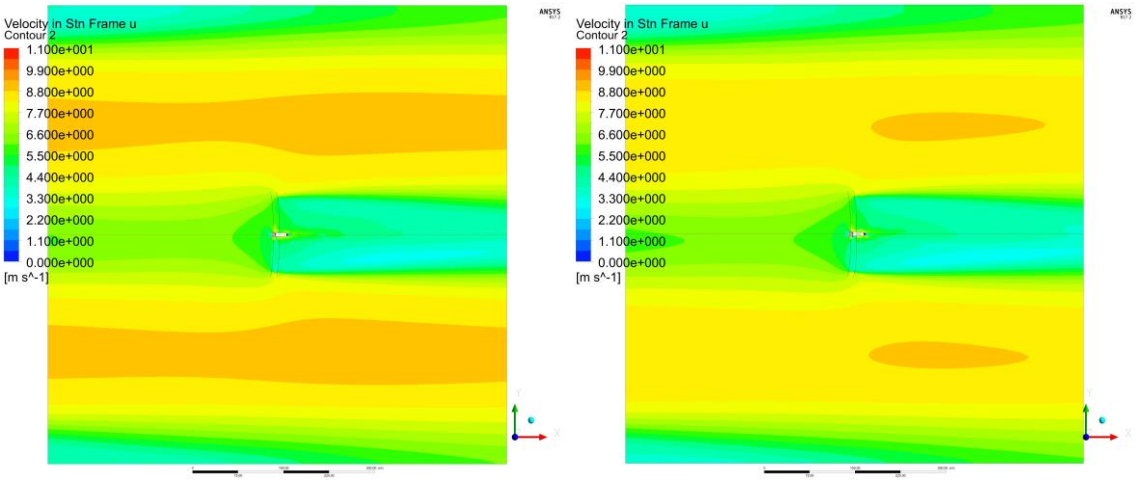

Figure 4-29 Contours of instantaneous streamwise velocity [m/s] at the rotor hub-height (taken at 100th revolution). Left: no tower, right: with tower.

The flow field comparison between 'Tower' and 'No Tower' cases is shown in Figure 4-27, Figure 4-28 and Figure 4-29. The first two graphs are plotted on a vertical plane that goes through the centre of the turbine, the last one is on a horizontal plane at hub centre level (90m above the ground). The tower seems to enlarge and elongate the wake behind the lower part of the rotor, as well as causes significant velocity deficit around itself. Even though, the upstream flow

profile on the rotor level does not look very different between “No Tower’ and ‘Tower’ case, this could suggest that this wind farm model has strong wake recovery potential.

There is no significant difference between the instantaneous and time-averaged contour plots, which means that the simulations have already reached a fairly stable state before the time-averaged calculation, this also agrees with what the plots are showing in Figure 4-26. It is clear to see the effects of the tower on the overall wind flow speed in the domain, the flow velocity has been slowed down on both vertical (Figure 4-27 and Figure 4-28) and spanwise directions (Figure 4-29). This essentially means that ‘Tower’ case has lower U_F value (7.9713m/s) compared to ‘No Tower’ (8.1389m/s) case. The decrease of U_F value leads to wind turbine performance reduction (refers to Equation 3-14 and Equation 3-15).

4.3.2.2 DDES

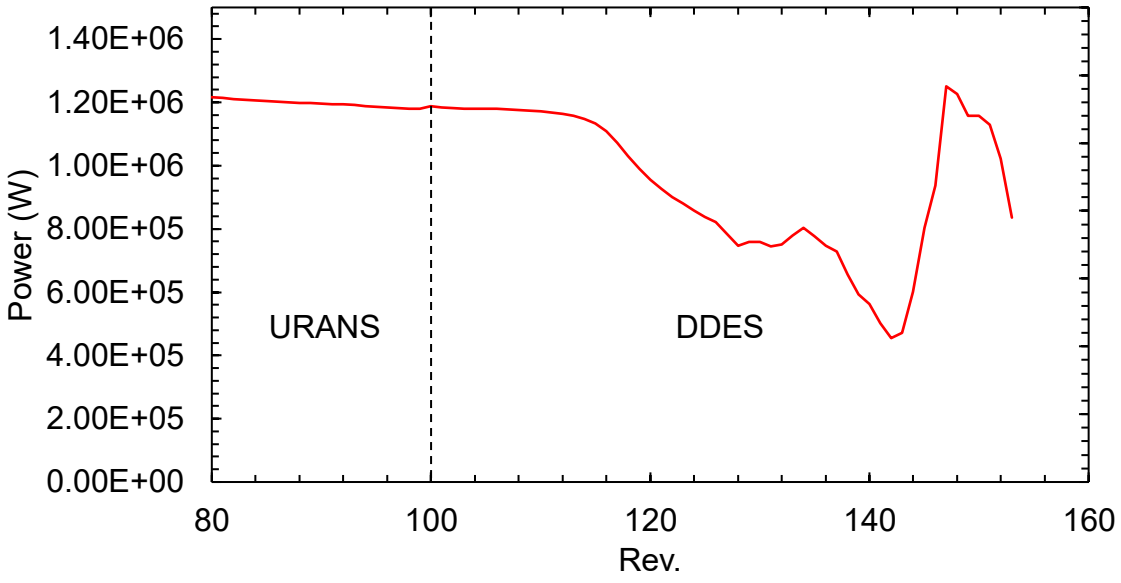

Figure 4-30 Convergence history of revolution-averaged power output, for URANS+DDES.

Within the time allowance of this study, we managed to run 54 revolutions of DDES for the ‘Tower’ case only. Using $U_F = 7.9713\mathrm{m/s}$ as a reference velocity, it takes approximately 13 revolutions for the wind flow go through the domain

once. As it shows in Figure 4-30 the turbine power output starts to differentiate from URANS results about 13 revolutions after switched to DDES followed by large fluctuations, as expected. The simulation will need to be extended for a much longer period, in order to obtain converged statistics of this highly turbulent wind-farm flow. Therefore, the DDES results are mostly for qualitative analysis in this study, they are not compared with the theoretical model.

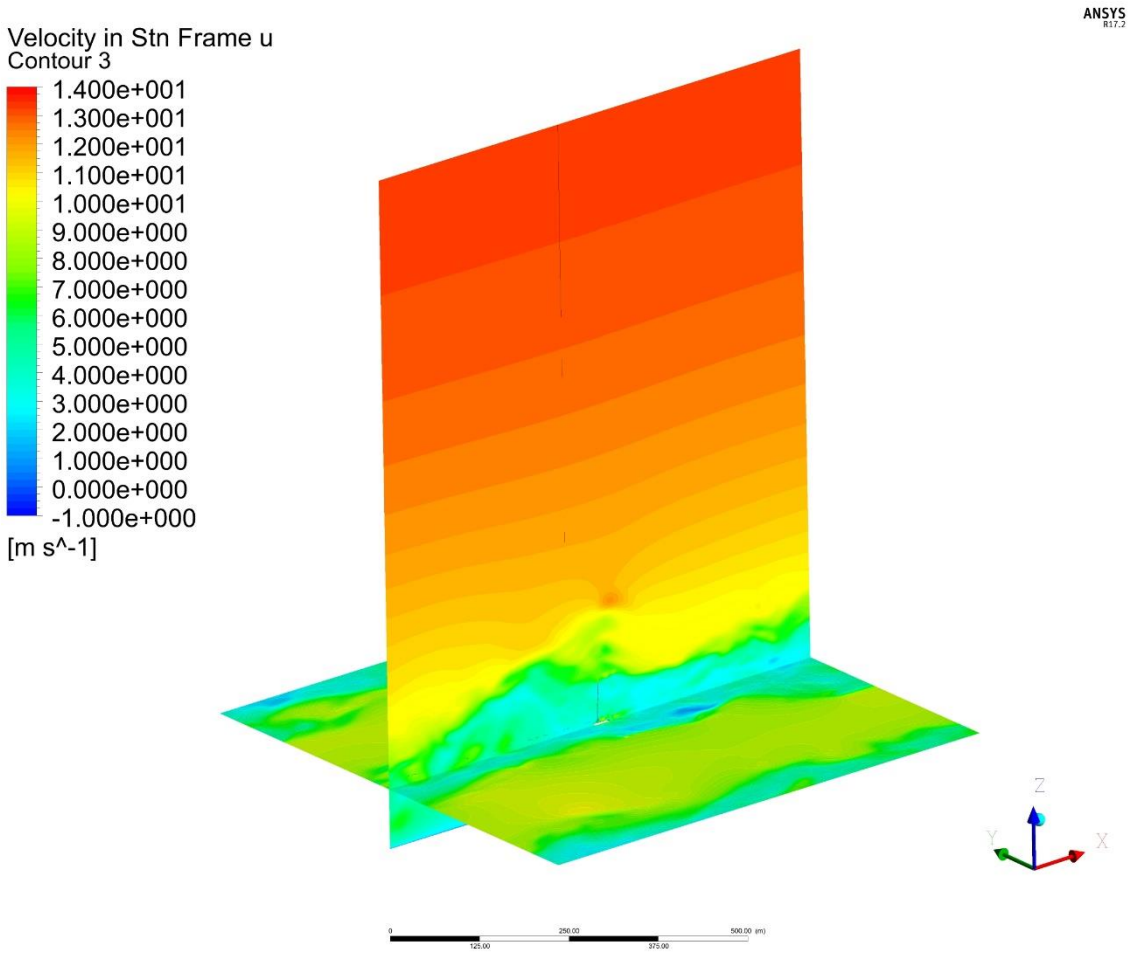

Figure 4-31 Instantaneous streamwise velocity contours [m/s] on the streamwise vertical plane across the centre of a turbine, and the spanwise vertical plane at the downstream end of the domain (taken at 118th revolution).

Figure 4-31 shows an example of instantaneous velocity contours on two different places, visualising the wakes of the entire wind turbine. The wind flow at the higher level stays in a much more uniform (RANS like) state compared to the lower level, unlike the AD simulations shown in Chapter 3 where large

eddies are visible throughout the entire domain (Figure 3-18). As it has been mentioned previously, the mesh and domain size of the FR model was created for URANS initially. Even though, the mesh quality and aspect ratios should not cause any noticeable issues, the relatively small domain size might restrain large eddy formation where it mostly exists at the higher level of the domain. It is still possible to have large eddies developed at the higher level of the domain, but this might take much longer simulation time than if a larger domain size was used.

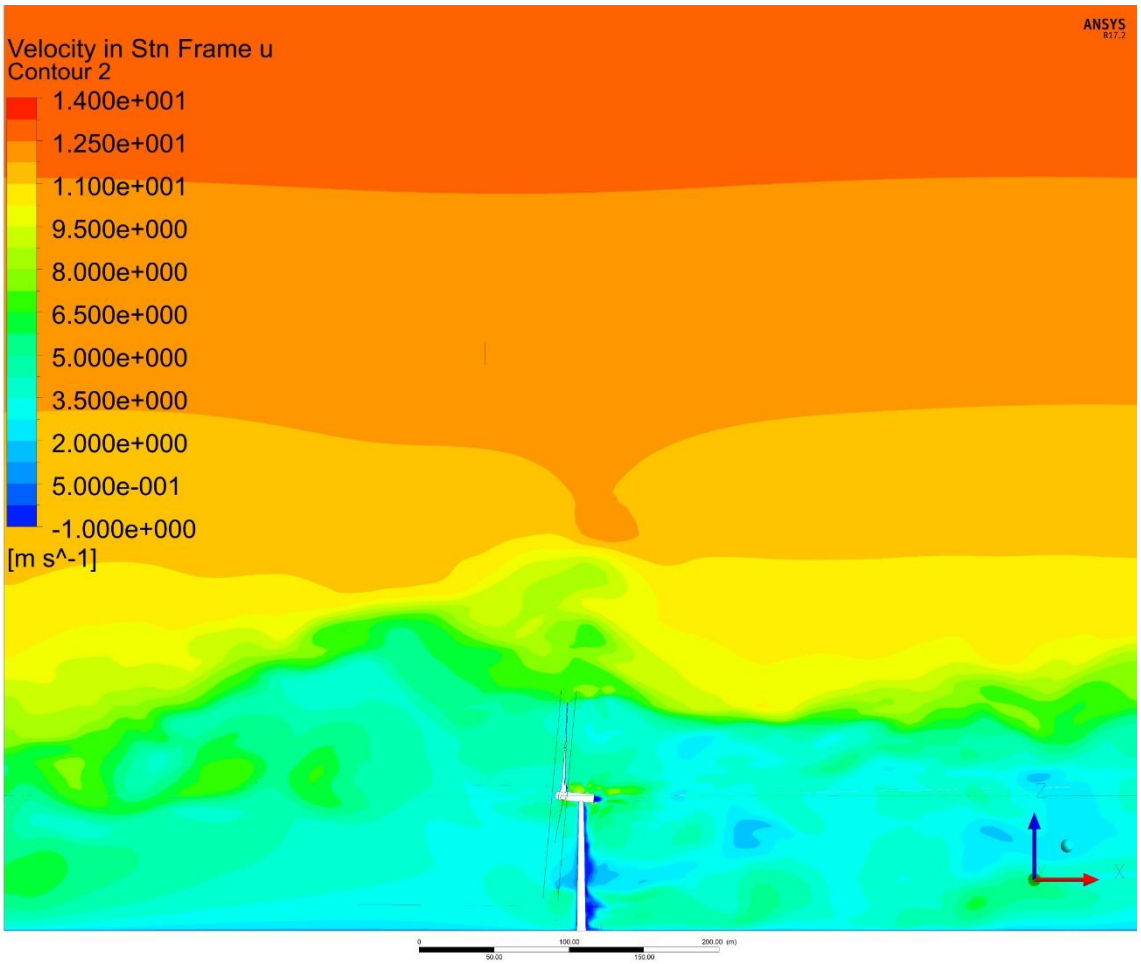

Figure 4-32 Contours of instantaneous streamwise velocity [m/s] at horizontal centre plane (taken at 154th revolution).

On the other hand, compared to higher level the wind flow at turbine level seems to be much more developed with realistic wake structures (Figure 4-32 and Figure 4-33). In addition, the flow pattern and velocity magnitudes in the

DDES stays relatively similar to the URANS results at $x/D = 1.5$ and $x/D = 3$ (Figure 4-34). However, the flow profiles show noticeable differences at $x/D = 5$, it seems URANS predicts quicker wake recovery than DDES. Furthermore, in the DDES flow profiles there is a clear separation especially at $x/D = 3$ and $x/D = 5$ (Figure 4-34), which agrees with Figure 4-31. This separation is mostly above the highest point of the turbine rotor, further investigation is required to determine whether the wind flows were actually affected by this issue or not.

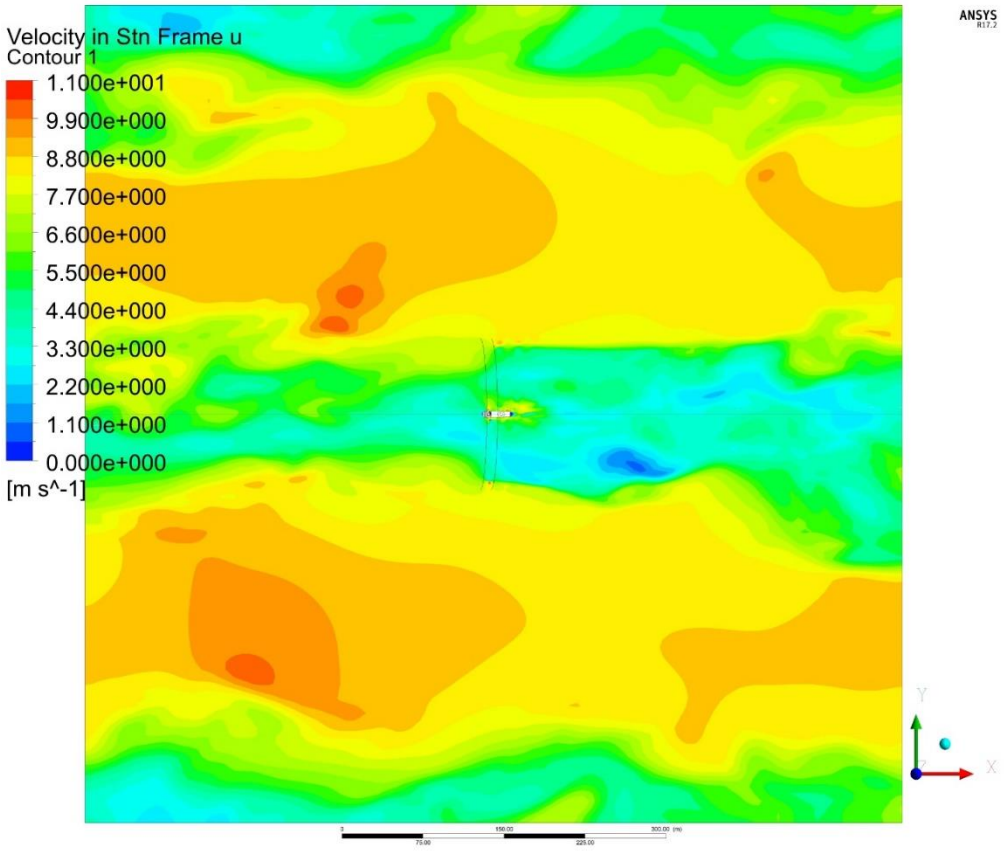

Figure 4-33 Contours of instantaneous streamwise velocity [m/s] at rotor hub-height (taken at 154th revolution).

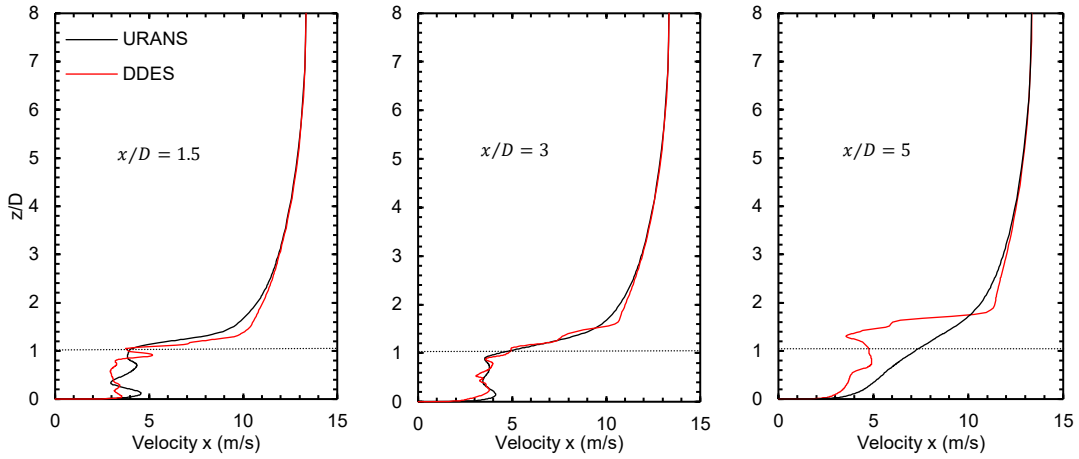

Figure 4-34 Instantaneous velocity profiles at different locations in the wake of the turbine, data taken at 118th revolution for the URANS and 154th revolution for DDES. The dash line is marking the top of the turbine.

The four 3D figures, Figure 4-35, Figure 4-36, Figure 4-37 and Figure 4-38, are showing the instantaneous vortex structures of URANS and DDES, where the first two are plotted on farm level and the other two are on turbine level. The vortex geometries are defined by Q-Criterion and the colour scheme is based on the instantaneous velocity.

The original single turbine domain is copied and relocated to the appropriate position in Figure 4-35 and Figure 4-36, in order to visualise the actual wind farm layout (refer to Figure 4-6). There are basic characteristics of turbine generated vortices that have been captured in the URANS data. However, we can not see any turbine and wake interactions, the turbines are as if they were isolated from each other. It is possible to show more wakes that is interacting with turbines by changing the Q-Criterion value, but it will only show solid cylindrical structure along the streamline without much meaningful details.

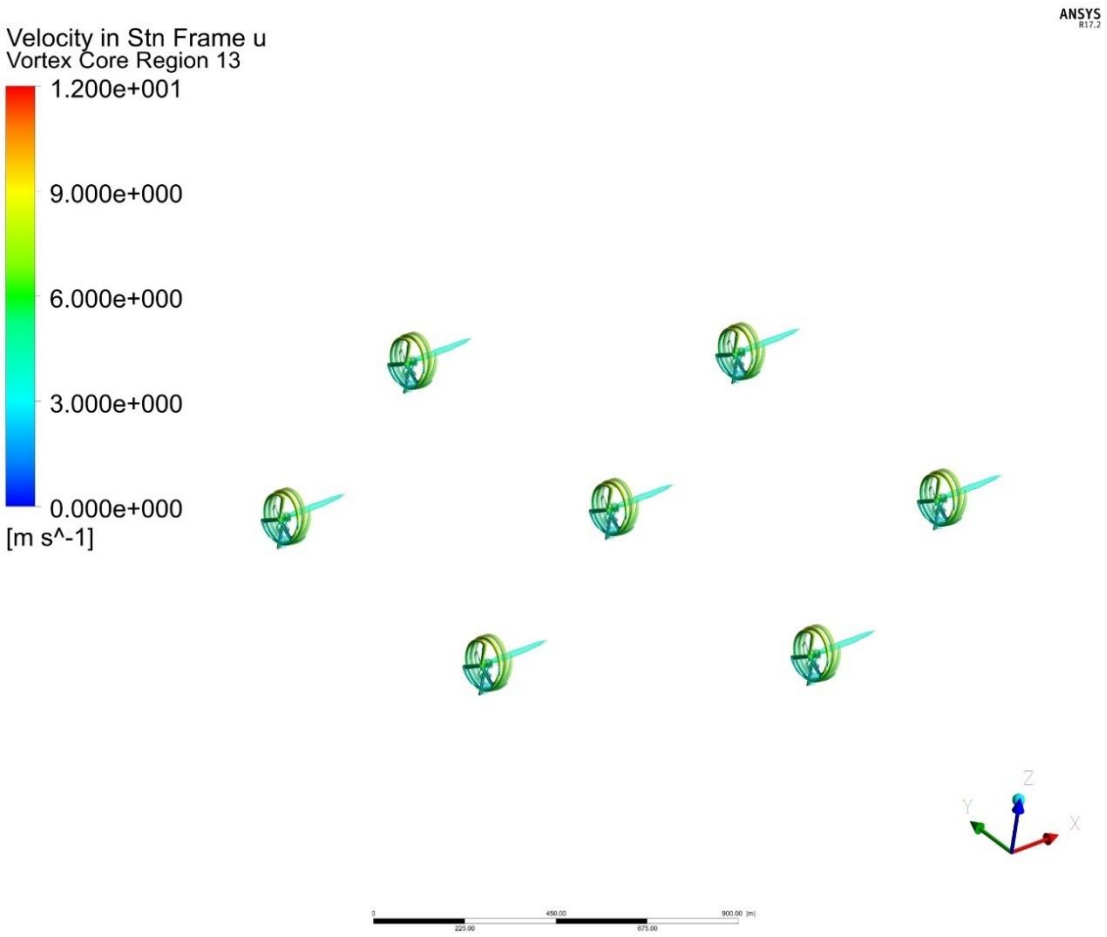

Figure 4-35 Farm level instantaneous vortex structures from URANS simulation.

On the other hand, using the same Q-Criterion value as the URANS, the DDES plot is demonstrating much more detailed vortex structures, we can see clear correlations between turbines and wakes. The DDES data has also captured the typical hairpin vortices, where they would normally appear on top of turbulent bulges of the turbulence wall [134]. This indicates the development of turbulence boundary layer around the turbines. In addition, the turbine wakes seem to predominantly affect turbines in the streamwise direction and not the ones in spanwise direction.

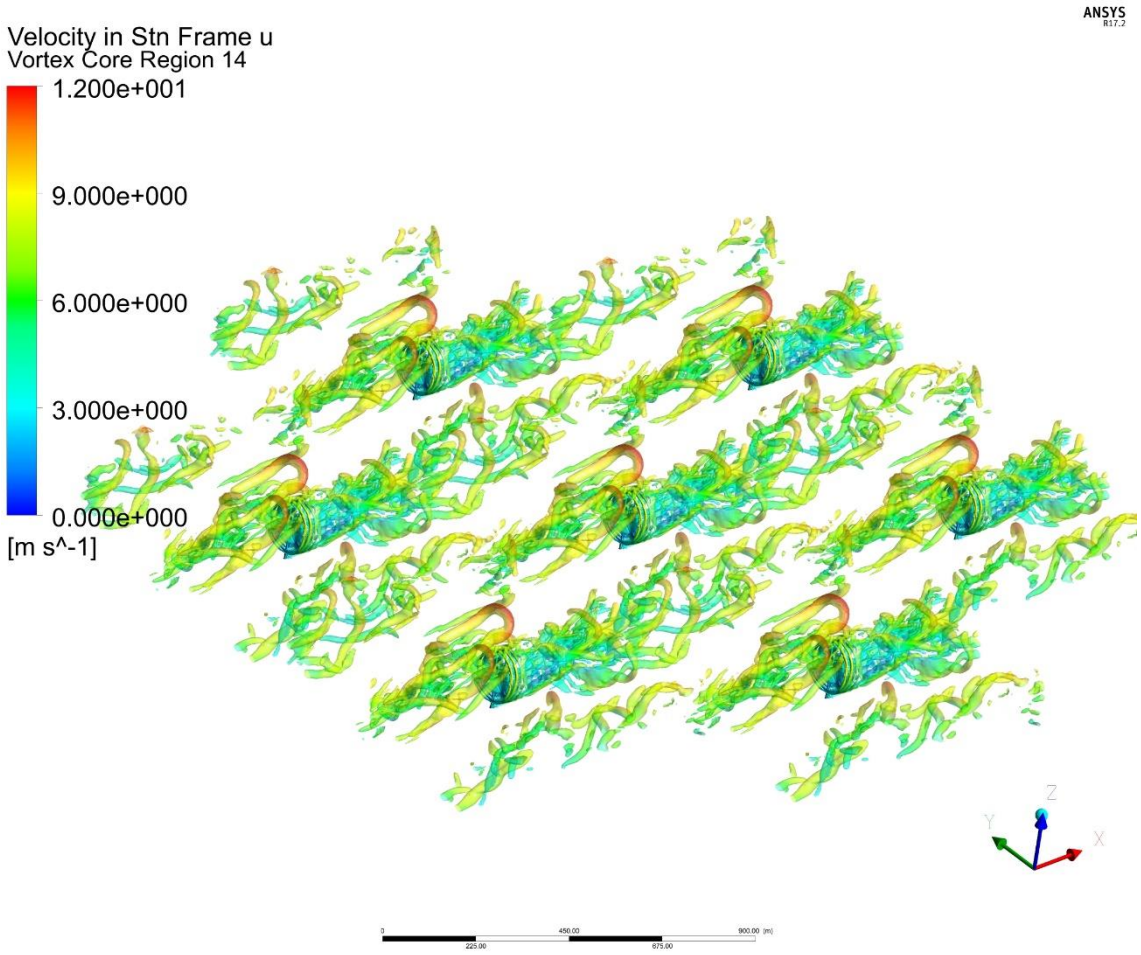

Figure 4-36 Farm level instantaneous vortex structures from DDES simulation.

The turbine level vortex plots (Figure 4-37 and Figure 4-38) are using slightly different Q-Criterion level from the farm level plots, so that we could focused on the smaller vortices that are close to the turbine surfaces. Similar to the farm level plots, the DDES results are showing more detailed vortex geometries compared to URANS. Both cases are showing strong and clear tip vortices generated by the turbine blades with similar geometries. One thing should be noted here, the near wall regions in the DDES are treated as RANS, therefore, the vortex structures close to the turbine surfaces are comparable between DDES and URANS results.

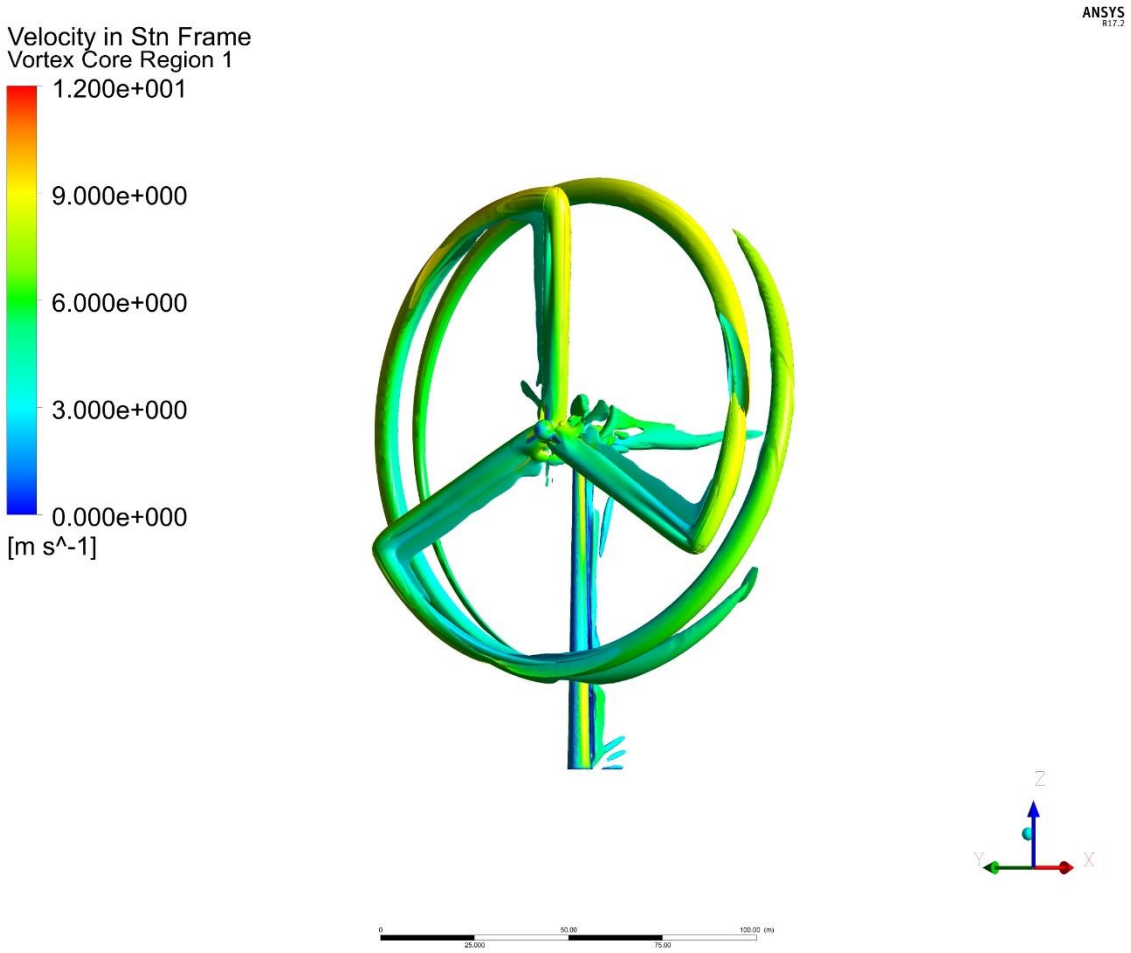

Figure 4-37 Turbine level instantaneous vortex structures from URANS simulation.

Moreover, the hub vortex has also been captured during the simulation, this vortical structure is located at the central part of the near-wake and elongated in the streamwise direction (Figure 4-39, we used URANS data to plot this figure that gives clearer visualisation of the hub vortex than DDES data). This phenomenon is being studied in some recent studies [135] [136], where it has been confirmed that the hub vortex is interacting with the tip vortex layer. Although, the exact behaviour and effects of such vortex is still not clear, even large discrepancies have been found between experimental and numerical studies [137] [138]. This should be a key point for future studies to investigate.

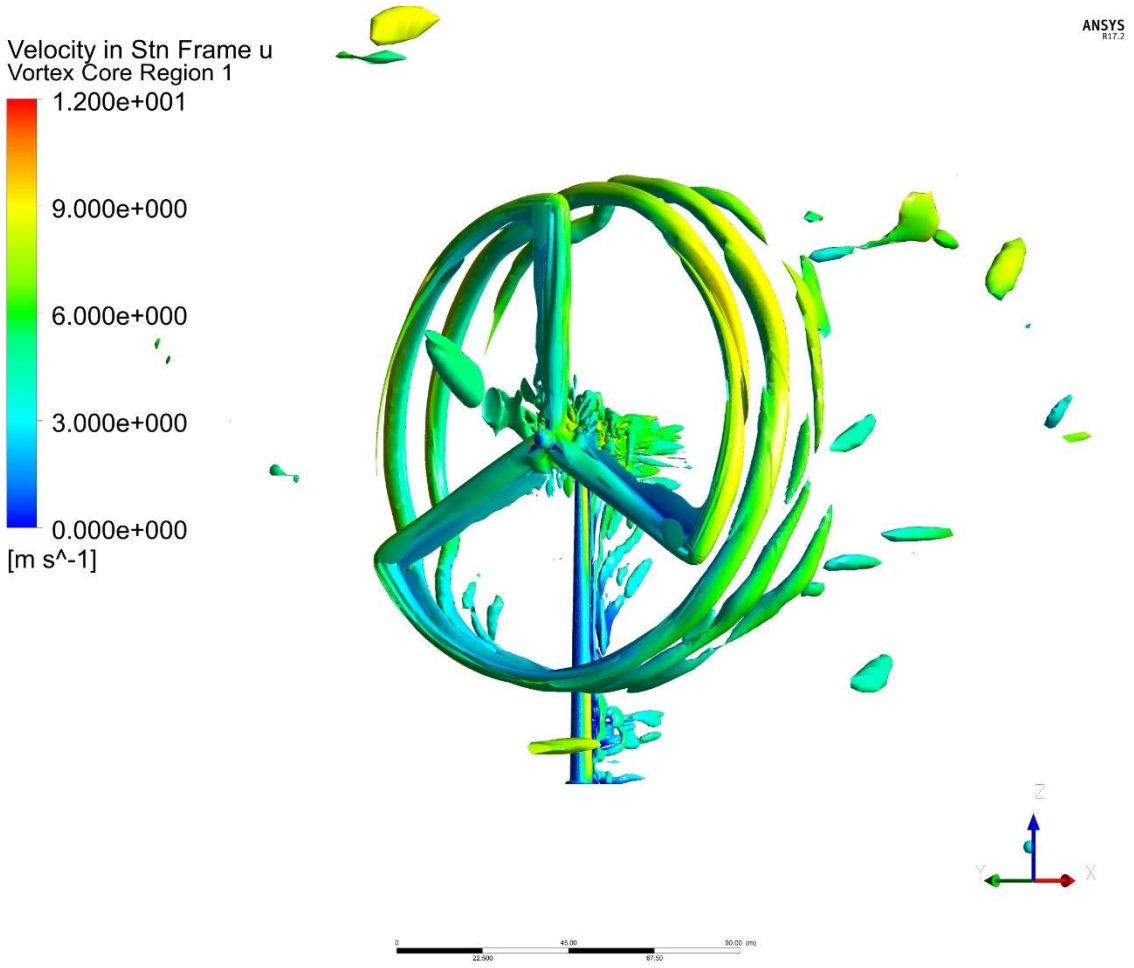

Figure 4-38 Turbine level instantaneous vortex structures from DDES simulation.

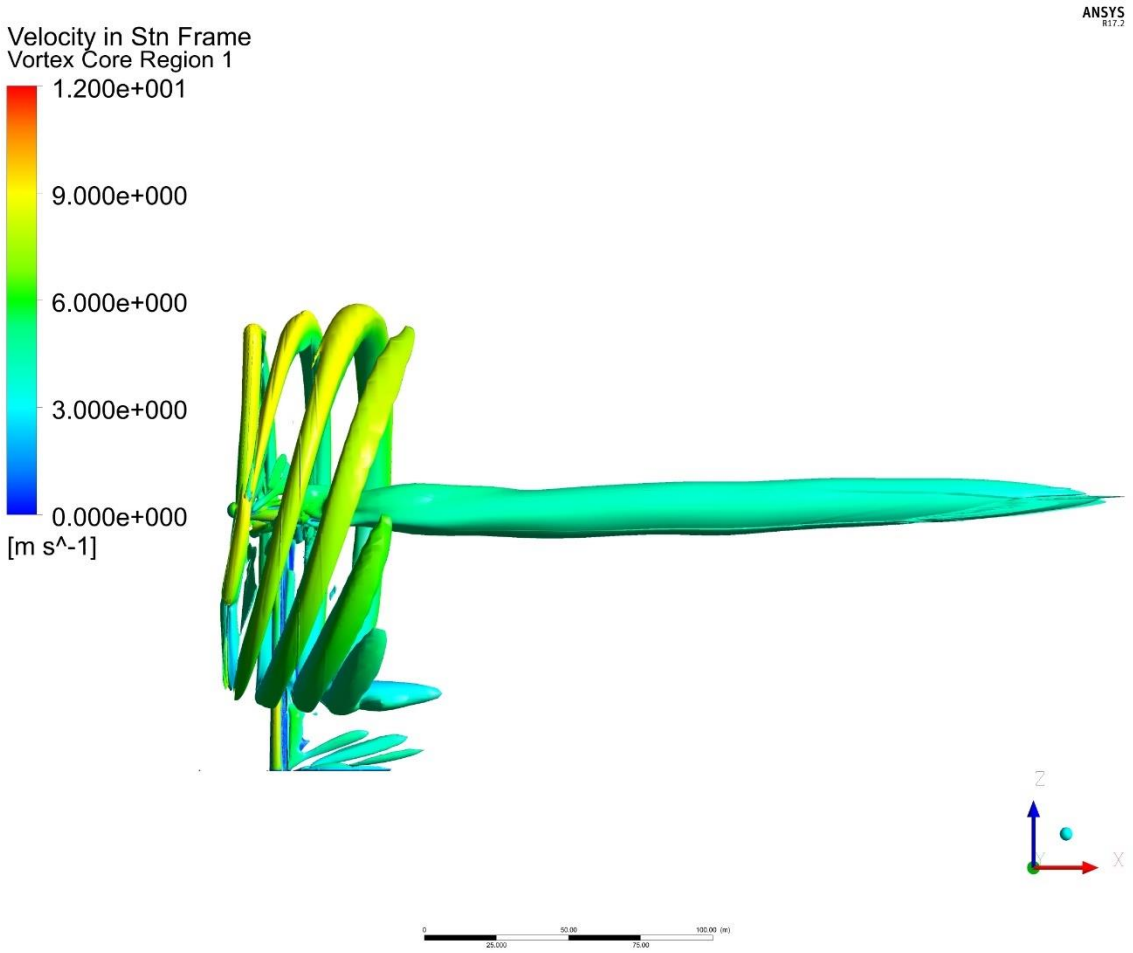

Figure 4-39 Turbine level instantaneous vortex structures from URANS simulation, nacelle wake visualisation.

4.3.3 CFD vs. theoretical model

As mentioned earlier the DDES data is still far away from stable, the CFD data used to compare with theoretical model is from the 18 revolutions of time-averaged URANS. The two plots showing in Figure 4-40 and Figure 4-41, are the comparisons of C_P and C_T calculated by CFD and theoretical model. It is clear to see that the CFD simulations have predicted the wind farm performance reduction due to the tower, which agrees with the theoretical model calculations. Furthermore, the CFD simulations seem to underestimate the farm performance compared to the theoretical model, this agrees with the AD model study discussed in Chapter 3. Even though, the CFD model is underestimating wind

farm performance level, the added turbine tower is showing greater effect here than theoretical predictions (Table 4-4).

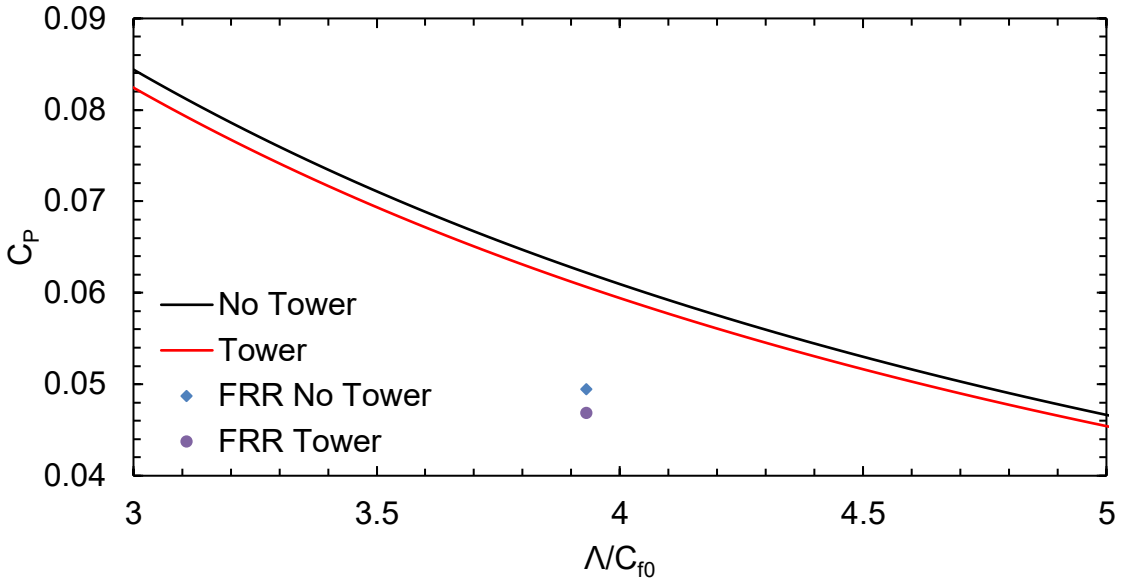

Figure 4-40 Comparison of C_P between CFD (blue and purple symbols) and theoretical model (black and red lines).

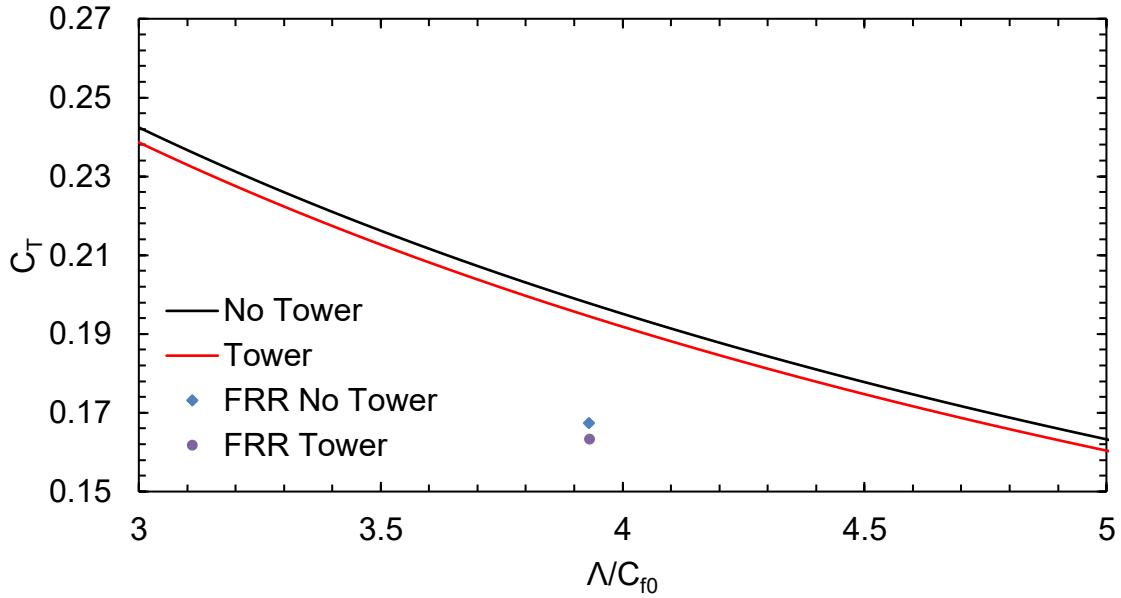

Figure 4-41 Comparison of C_T between CFD (blue and purple symbols) and theoretical model (black and red lines).

On one hand, these discrepancies between the theoretical farm model and FR farm simulations are understandable, since the theoretical model uses the

classic actuator disc theory as rotor and tower models, i.e. the theoretical model considers 'ideal' turbines and highly simplified support structure to predict an upper limit to the farm performance. In addition, the original theoretical mode (that we are comparing with in this chapter) does not include turbine and wake interactions as well as local blockage effects.

Table 4-4 CFD and theoretical model results comparison ($K_s = 1m$, $\lambda/C_{f0} = 3.93$, $U_{F0} = 14.9m/s$, $\tau_{\omega 0} = 0.7547Pa$ and $(A_s/A)C_d = 0.01949$).

		β	C_P	C_T
CFD	No Tower	0.546235	0.049464	0.167463
	Tower	0.534987	0.046887	0.163316
	Diff.%	2.06%	5.21%	2.48%
Theoretical model	No Tower	0.471763	0.06222	0.197822
	Tower	0.467793	0.060662	0.194506
	Diff.%	0.84%	2.50%	1.68%

The original idea was also to compare the estimated support structure drag with the simulated results from CFD model. The assumed support strugure drag for this case is calculated (equations are decribed in Chapter 3) using the tower geometry in the 3D model and a tipical cylinder drag coefficient 0.6 (matched to the Re number in this study [113]). However, we have noticed that the recored drag cofefficient values for the tower in CFD simulations are lower than 0.6 (Figure 4-42). The three rapid C_d value reductions (more than 50% less from peak value) are when each time one of the three blades is overlaping with the tower.

As it was mentioned earlier, FLUENT uses a constant reference velcocity value to calculate all recorded coefficent during simulations. The tower surface area is much smaller compare to the swept area of the rotor, it is not straightforward to find the approperiate velocity value for the "correction" process. This is a cirtical

part for future studies to investigate, placing probs close to the tower to record live wind velocities could be a solution.

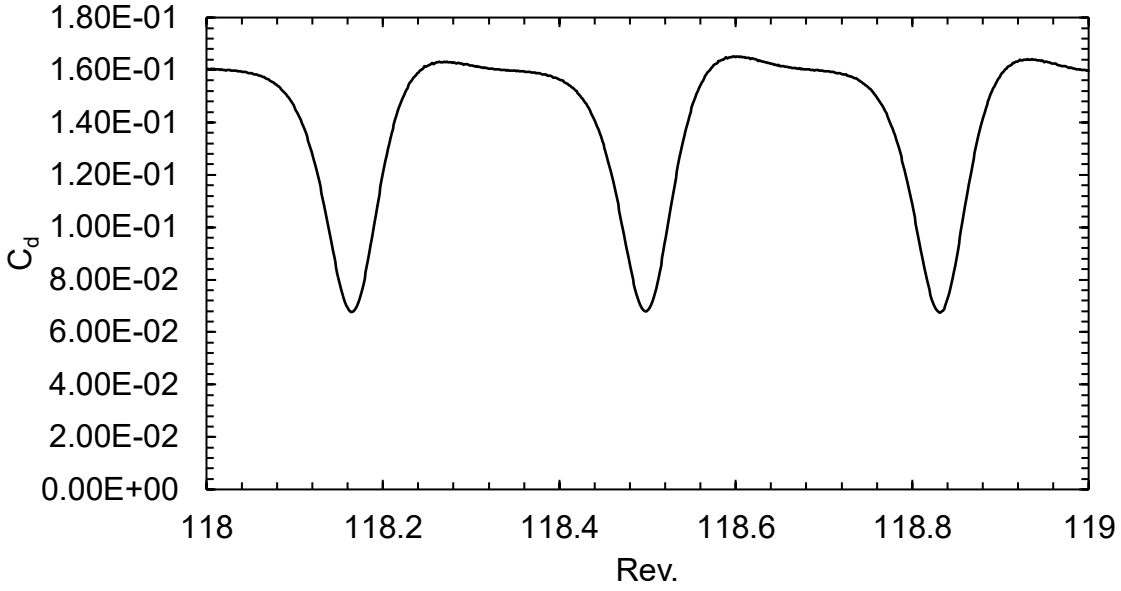

Figure 4-42 Recorded drag coefficient of the tower during 1 revolution in CFD simulation.

4.4 Conclusions

In this chapter we have demonstrated the 3D model construction and meshing process of the NREL 5MW wind turbine, with and without the monopile tower. The turbine model validation and turbulence model comparison have been performed using the non-tower single turbine model. Two commonly used turbulence models $k-\varepsilon$ Standard and $k-\omega$ SST have been tested; the results are compared with the original NREL report. Both models have shown good agreement with the original data, which indicates that the 3D turbine model and mesh is a close representation the original NREL 5MW design. It should be noted that this turbine was only created a reference for numerical studies, no experimental data exist up to this point. Moreover, the $k-\omega$ SST seems to underestimate the turbine performance and $k-\varepsilon$ Standard is the opposite. Considering the local blockage effect the CFD model should give higher estimations than the original values [114], the $k-\omega$ SST model seem to be the better choice in this case.

Three wind farm simulations have been conducted in this study, which are URANS ‘No tower’, URANS ‘Tower’ and DDES ‘Tower’. The CFD results have shown prominent overall wind farm efficiency differences between ‘No tower’ and ‘Tower’ cases. This further approves the importance of including turbine support structures for wind farm modelling, which agrees with the findings in Chapter 3 (also in [93] [132]).

The time-averaged URANS results have been compared with the theoretical model [22] [132] predictions. Similar to the previous study [107], the theoretical model is predicting higher wind farm efficiency in general, compared with CFD simulations. On the other hand, the CFD models show large efficiency reduction from the added tower. The results difference between AD and theoretical model is only up to 10% (as shown in Chapter 3), but the FR model is showing even greater variations. Since the FR model is a more realistic modelling method compared to AD and theoretical models, we could assume that the tower effect might be even more prominent in real life scenarios.

The discrepancies between FR and theoretical models could be due to the theoretical model is a highly simplified representation of the wind farm, it does not include complex flow conditions (such as local blockage effect and turbine-wake interactions) that the high fidelity CFD models could produce. Although, there are a few modifications to the original theoretical model have been proposed by Nishino. One particular change is to replace the classic actuator disk theory with BEM (it is called ‘BEM-FM’ method) [94], which allows the model to consider more sophisticated local (turbine and even blade level) flow conditions. This modified version of the theoretical model is still under development, the FR model results could be used to validate and improve this modified theoretical mode in future studies.

We have manged to run 54 revolutions of DDES for ‘Tower’ case. The contour plots shown in this chapter have presented useful information. The hub vortices have been clearly captured in both DDES and URANS simulations, even though, the exact mechanism and effects on wind farm (or wind turbine) efficiency are still unclear, at least we know this FR model is able to capture this

phenomenon and it could be potentially adopted for further investigation. As expected, the DDES results show much more realistic flow conditions and details than URANS can, for instance the typical hairpin vortex structures are clearly visible around the turbulence boundary layer. Moreover, it is slightly more complicated to initiate a DDES case with FR model, but the actual simulation cost is very similar to URANS (for a given number of rotations). Therefore, we valuable information could be extracted, if the DDES was extended for a much longer period. One thing should be noted, a larger domain size (similar to the one used in chapter 3) with multiple turbines should be considered in the future, in order to capture the correct large eddy structures, although, the simulation cost might become unrealistically high. Finding a trade-off point between domain size and simulation time could be a valuable research topic for future studies.

5 Numerical Weather Prediction Model

5.1 Introduction

Wind farm blockage effect is becoming a popular topic in the wind energy industry today [100]. The basic idea of this effect is that the incoming flow is deflected by the wind farm, which leads to part of the flow bypassing the entire farm; therefore, the average wind speed across the wind farm is reduced more than the case without such farm-scale flow deflection. To predict this power reduction effect for a given large wind farm under given weather conditions, it is essential to understand how the momentum balance over the wind farm changes under various weather conditions. The two-scale momentum theory proposed recently by Nishino and Dunstan [21] may help analyse this complex flow problem. The theory describes a generic relationship between 'farm-scale' and 'turbine-scale' flows, derived directly from the law of momentum conservation. This essentially allows us to consider large-scale motions of the atmospheric boundary layer (ABL) in a timedependent manner. In this study we follow the concept of the two-scale momentum theory and try investigating the momentum balance over a large offshore wind farm using a numerical weather prediction (NWP) model. The NWP model used in this study is the one currently being used for weather forecasting in the UK. Some initial results of a test case, which considers an offshore wind farm site located in the North Sea, are presented in this chapter.

One thing should be noted here, due to national security reason the NWP model is not accessible outside the UK Met Office, therefore, the simulations presented here were ran by Dunstan within the Met Office facilities.

5.2 Theoretical Model Modification

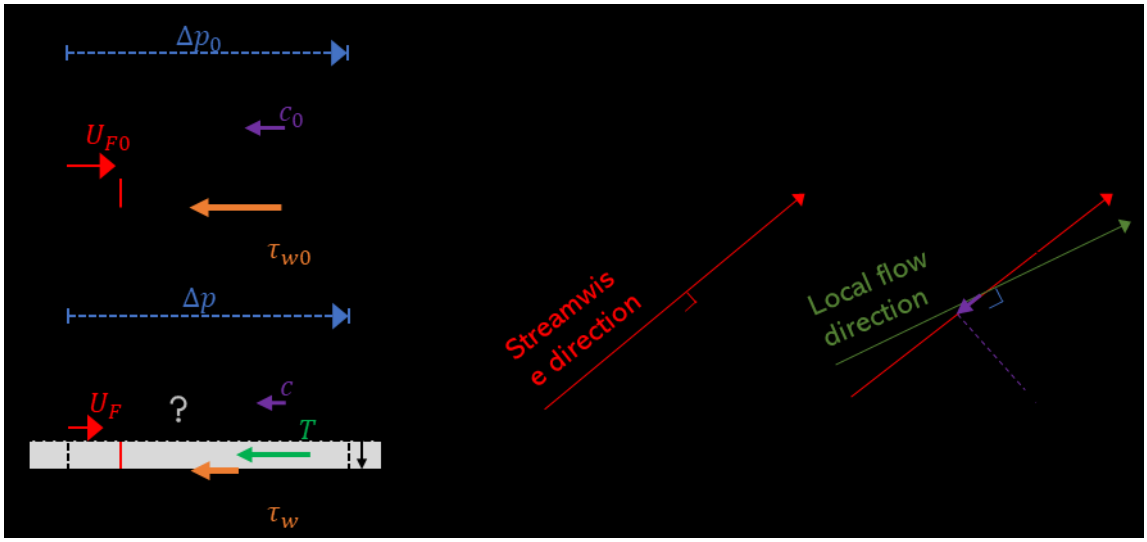

Figure 5-1 Schematic of the two-scale momentum model [102]: (a) fully developed boundary layer before and after farm construction, (b) Force vectors and flow directions at the hub-height (left) and at a higher altitude (right) with the 'streamwise' component of the Coriolis force (purple arrow).

The two-scale momentum theory [102] considers the momentum balance of flow over a large finite-size wind farm, where the length of the farm is much larger than the thickness of the ABL. Essentially, this theory helps us combine 'internal' (turbine scale) and 'external' (farm scale) flow models while satisfying the law of momentum conservation. The external flow model considers large-scale fluctuations due to changes in atmospheric conditions (with periods of more than about an hour), whereas the internal flow model considers small-scale motions due to turbulence (with periods of typically less than a few minutes). The theory explains that, if we assume that the flow over the turbine array is in a fully developed state, the momentum available to the ABL's bottom resistance (due to turbine drag and land/sea surface friction) can be described by three key terms, namely the pressure gradient, Coriolis and time-derivative (flow acceleration/deceleration) terms [102]. In the present study, we numerically investigate how these three terms tend to change in time, using an NWP model.

The pressure gradient term ($\Delta p/\Delta x_F$, where x_F is the 'streamwise' direction of flow over the wind farm, defined as the direction of flow at the turbine hub-height averaged over the entire farm) may be considered as the primary driving force of flow over the wind farm [21] [94]. This pressure gradient may change depending on the existence of the wind farm itself, since the reduction of wind speed may occur even upstream of the entire farm due to the farm-scale blockage effect [100], and hence the farm may experience a larger streamwise pressure gradient than that observed before farm construction [21] [132]. This pressure gradient may also be affected by the generation of gravity waves (induced by the wind farm itself under certain atmospheric conditions) [6] [7]. Figure 3-2 shows a schematic of this additional pressure gradient induced by a large finite-size wind farm.

In addition, the latest theory also considers the effects of wind acceleration/deceleration ($\partial[\rho U]/\partial t$, where ρ is air density and U is streamwise velocity, and the square bracket represents averaging over a representative control volume (CV) defined later) as well as the Coriolis effect (C) [102]. Although the direction of the Coriolis force is always perpendicular to the local flow direction, this may still affect the streamwise momentum balance of the farm, since the local flow direction may change in altitude, as depicted in Figure 5-1. The Coriolis force term C is approximately $f_C[\rho U \tan\theta]$, where f_C is the Coriolis parameter ($f_C = 2\Omega \sin\phi$, where $\Omega = 7.292 \times 10^{-5}$ rad/s is the rotation rate of the Earth and ϕ is the latitude of wind farm location), and θ is the difference in angle between the streamwise and local flow directions (θ in this case is measured positive in the clockwise direction as shown in Figure 5-1(b)). Eventually, we can derive a (non-dimensionalised) momentum balance equation that describes the relationship between these three terms and the ABL's bottom resistance as follows [102]:

Equation 5-1

$$\frac{T + \langle \tau_w \rangle S}{\langle \tau_{w0} \rangle S} = \frac{\frac{\Delta p}{\Delta x_F} - C - \frac{\partial}{\partial t}[\rho U]}{\frac{\Delta p_0}{\Delta x_{F0}} - C_0 - \frac{\partial}{\partial t}[\rho_0 U_0]}$$

where T is the turbine drag within the CV, $\langle \tau_w \rangle$ is the streamwise bottom shear stress averaged over the CV's bottom surface area, S, and the subscript '0' indicates that the variable is for the case with no wind farm. To summarise, the left-hand-side of Equation 5-1 represents the ratio of streamwise momentum loss between the case with farm and the case without farm, and the right-hand-side represents the ratio of the streamwise momentum available to the total bottom resistance for the case with farm to that for the case without farm.

It should be noted that, although only the ground shear stress $\langle \tau_{w(0)} \rangle$ is explicitly shown in this momentum equation, the effect of mixing inside and above the wind farm is also included implicitly. The introduction of wind farm will change the strength of mixing, which will change the local flow angle θ (shown in Figure 5-1) and consequently the Coriolis term in the two-scale momentum model.

Another key factor considered in the two-scale momentum theory is the farm wind-speed reduction factor, $\beta \equiv U_F/U_{F0}$, where U_F and U_{F0} are the 'farm-average' wind speeds for the cases with and without the wind farm, respectively, defined as in [102]. The role of β is essentially to provide a link between the 'internal' and 'external' parts of the flow system. In the internal problem, the turbine wind-speed reduction factor is defined as $\alpha \equiv U_T/U_F$, where U_T is the average wind speed through turbines. The two wind-speed reduction factors, α and β, can be calculated by solving both internal and external problems simultaneously, and the validity and usefulness of this two-scale coupled approach have been confirmed, for example, in [98]. However, this will not be discussed further here since the focus of the present study is on the external part of the problem only. The full explanation and derivation of the two-scale momentum theory is available in [102].

5.3 Methodology

The NWP simulations are carried out using a limited-area configuration of the Unified Model nested within the Global Model at N768 resolution (~20km Δx) [139]. The inner domain is a rotated pole lat-lon grid with a uniform horizontal grid spacing of approximately 1km. The domain size is 200x200 grid points in

the horizontal, and a 70-level stretched vertical grid is used with the first grid level at 5m. We have conducted ‘twin’ simulations, i.e., two simulations under identical initial and boundary conditions for 24 hours of simulation time, but one with farm and the other without. A circular shaped wind farm is located at the centre of the domain with a diameter of 20 km, and is represented simply by an area of increased bottom roughness ($z_0 = 0.7\,\mathrm{m}$, which is found to yield a plausible level of farm-average wind speed reduction as shown later in Figure 6) to assess the effects of large-scale motions of the atmosphere on the flow over the farm area. The main advantage of using roughness to represent a wind farm is its simplicity, whereas the weakness is that it may not necessarily predict the Reynolds stress distribution across the farm correctly. The geographical region chosen is an offshore region in the North Sea, south east of Arbroath in Scotland (Figure 5-2).

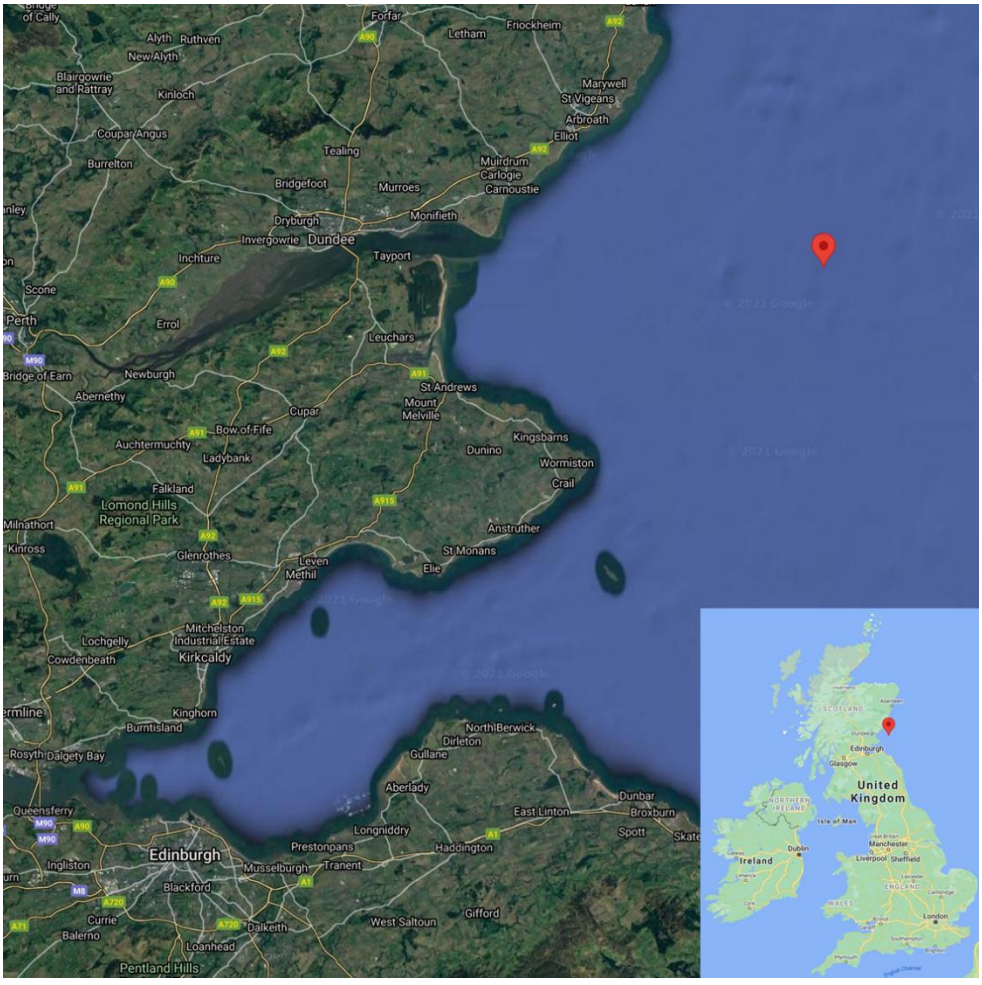

Figure 5-2 Exact location, from Google Maps

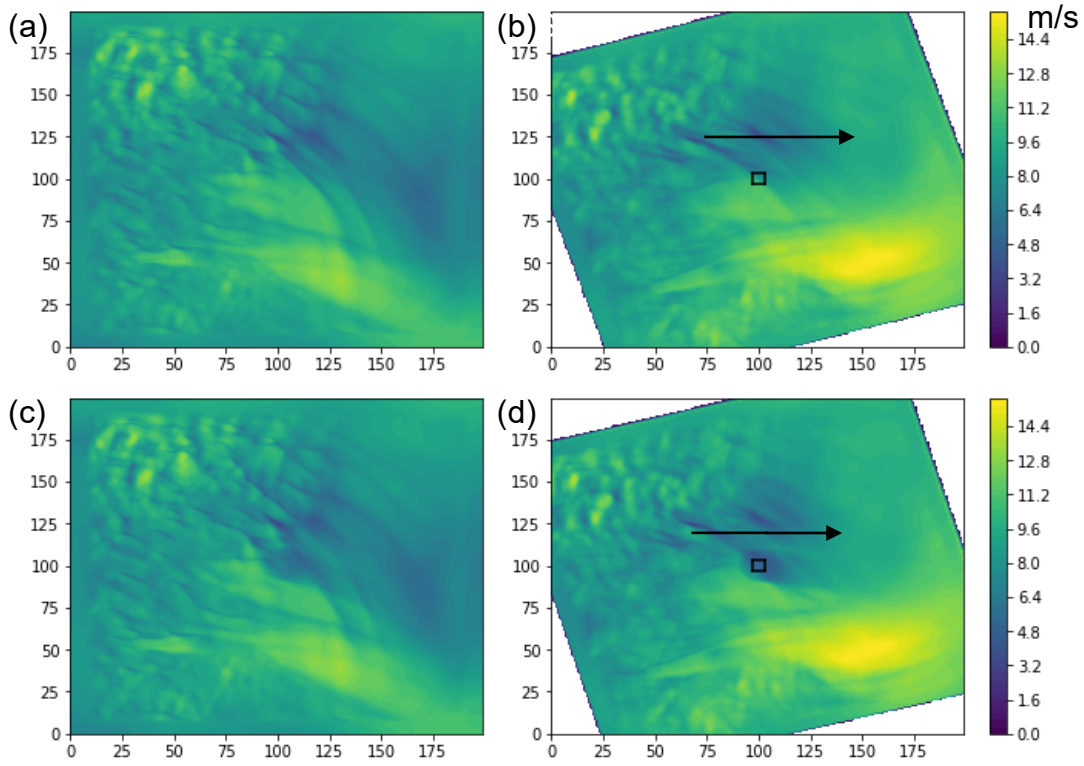

Figure 5-3 Contours of instantaneous (0800 UTC) horizontal velocity (m/s) at 33m above sea level (the scale used on x and y axis is in km). (a) and (c) are before data rotation, showing longitude-wise velocity. (b) and (d) are after data rotation, showing stream-wise velocity. The black square indicates the CV within the farm. A moderate wind speed reduction can be observed in the wind farm region, with a clear wake behind the wind farm as well.

By comparing the two cases as in Figure 5-3 (a) and (c), a moderate wind speed reduction can be observed in the wind farm region, with a clear wake behind the wind farm as well. The 'twin' simulations started with identical conditions (apart from the wind farm) and, after 8 hours of simulation time, the two flow fields are still mostly identical except for the region around the wind farm, suggesting that this twin simulation approach is appropriate for the purpose of this study. Furthermore, a data rotation method is applied to the raw data from the simulation, which can be seen in Figure 5-3 (b) and (d). The idea is to align the streamwise direction with the horizontal axis and the 'inlet' and 'outlet' faces of the rectangular CV (located at the centre of the farm) are perpendicular to the streamwise direction. This is to simplify the calculation

steps in the post-processing, especially for the calculation of the Coriolis term where the flow direction angle is important.

The black square shown in Figure 5-3 (b) and (d) indicates the specified CV inside the wind farm, with dimension of 6km x 6km x 2km. The horizontal size of the CV was decided to be large enough to represent essential characteristics of the wind farm, and yet small enough not to include the edge of the wind farm. The height of the CV ($\mathrm{H_{CV}}$, as depicted in Figure 5-1) was determined from the time-averaged streamwise velocity profile for the no farm case, to reduce the effect of shear stress at the CV's top surface (Figure 5-4). Although the velocity profile changes in time, we use the same $\mathrm{H_{CV}}$ value (2km) at all time steps in this study for simplicity.

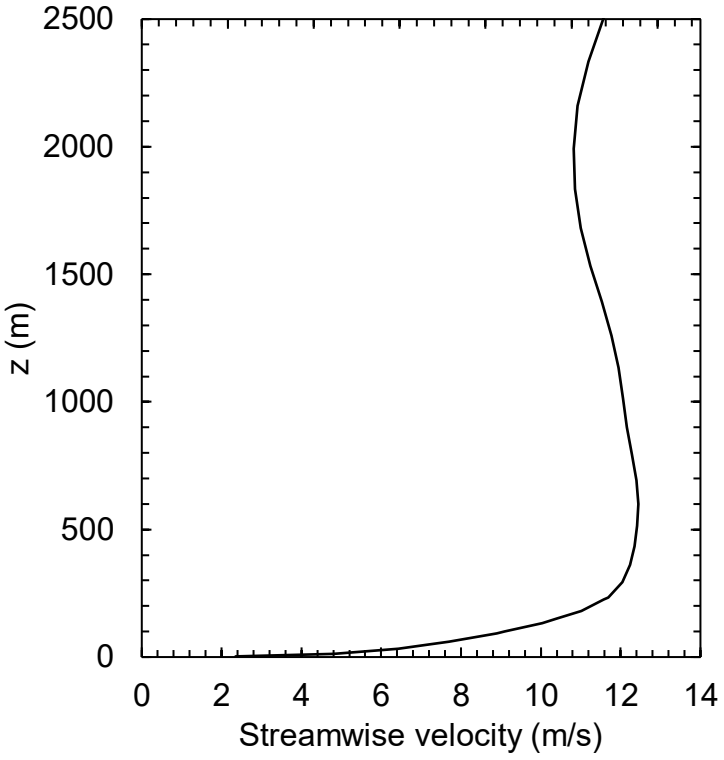

Figure 5-4. Time-averaged streamwise velocity profile at the centre of the wind farm.

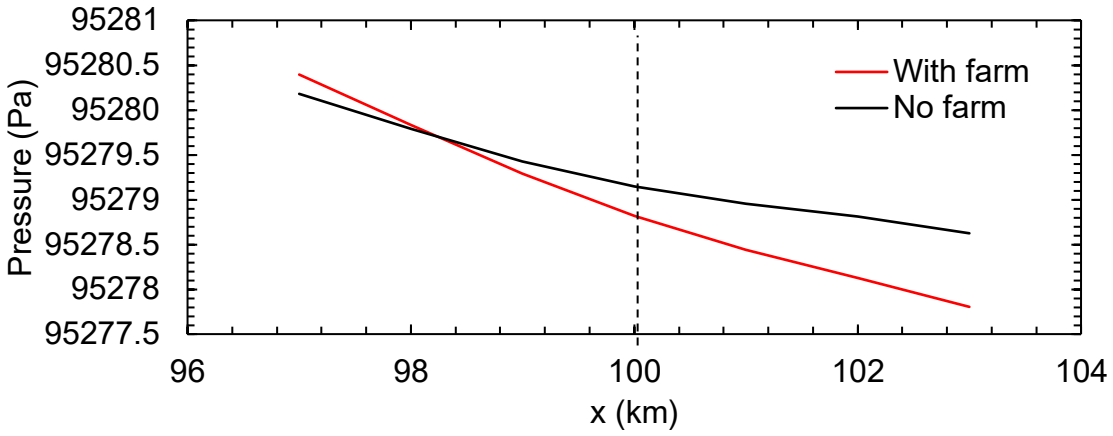

Figure 5-5. Streamwise variation of instantaneous (0800 UTC) pressure (averaged vertically from 0 to 2000m above the sea level) across the CV region (wind farm centre is at x=100 km). This agrees with the assumption shown in Figure 3-2 that the pressure gradient increased after adding wind farm.

As an example, the instantaneous pressure profiles shown in Figure 5-5 demonstrate the additional pressure difference induced by the wind farm, i.e., the pressure profile has a steeper streamwise gradient when the farm is introduced, which agrees qualitatively with the schematic picture shown earlier in Figure 3-2.

5.4 Results and Discussions

Results of the twin simulations are presented below. The time period of the results presented here is from 0800 UTC to 2200 UTC, although the simulations conducted were for 24 hours of simulation time. The initial 8 hours of the data were excluded to allow for spin-up within the inner domain, whereas the last hour was excluded as some of the variables (which require their time-derivative for their calculation) are not available at the last hour.

Figure 5-6 shows the time-histories of area-averaged streamwise velocity (averaged horizontally across the CV) at the assumed 100 m hub height, for the cases with and without wind farm. A relatively constant difference can be seen between 'No farm' case and 'With farm' case, indicating that the wind speed is slowed down by introducing a wind farm (modelled using a constant roughness length of z_0 = 0.7m) fairly consistently throughout the day.

The changes of streamwise angle are shown in Figure 5-7. It can be seen that the streamwise angle of 'With farm' case is slightly changed from 'No farm' case, and the 'With farm' case always has a smaller value for the streamwise angle than 'No farm' case, which means that the wind farm turns the hub-height wind direction slightly in the anti-clockwise direction. The angle difference between the two cases is relatively consistent (about 1 to 4 degrees).

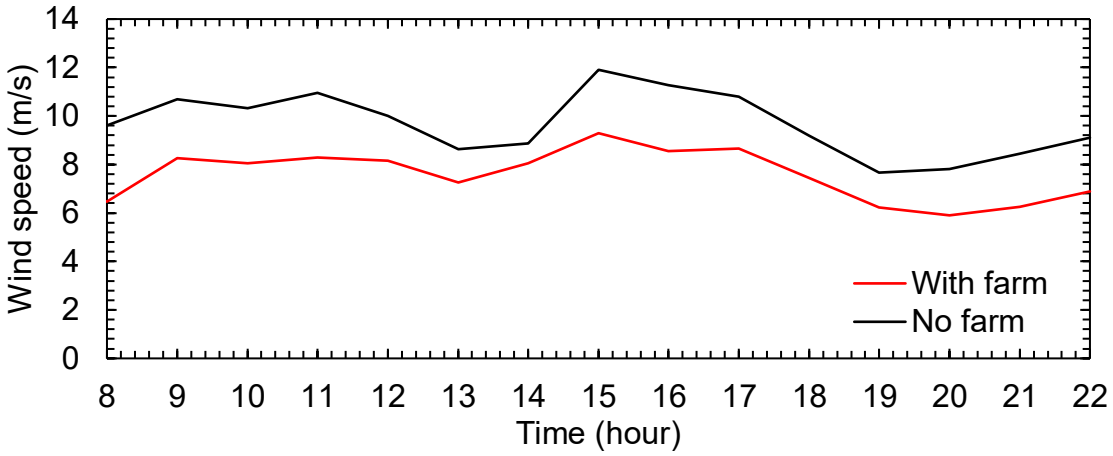

Figure 5-6 Streamwise wind speed at the hub height. A relatively constant difference can be seen between 'No farm' case and 'With farm' case, indicating that the wind speed is slowed down by introducing a wind farm.

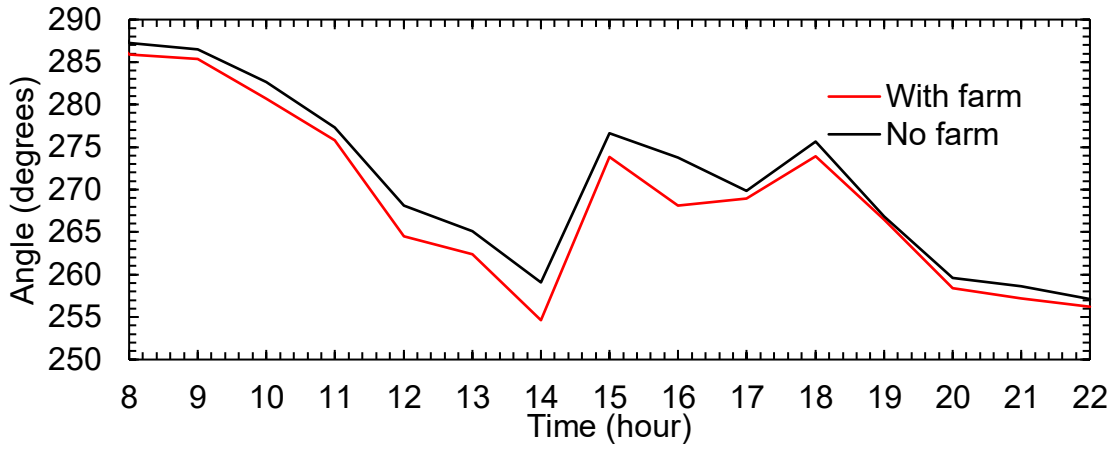

Figure 5-7 Streamwise angle (measured from North, taken positive in clockwise) at the hub height. The 'With farm' case always has a smaller value for the streamwise angle than 'No farm' case, which means that the wind farm turns the hub-height wind direction slightly in the anti-clockwise direction.

To calculate the pressure gradient term ($\Delta p/\Delta x_F$), we take the difference of the surface-average pressure values between the 'inlet' (upstream side) and the 'outlet' (downstream side) surfaces of the CV, and then divide it by the streamwise length of the CV, Δx_F = 6000 m. The results shown in Figure 5-8 are in agreement with Figure 5-5, i.e., the additional pressure difference induced by the farm is apparent, and this effect is relatively consistent during the day. This supports the argument that the streamwise pressure gradient tends to be enhanced by the wind farm itself.

The Coriolis term, C, is calculated from the volume-average (over the CV) of the streamwise component of the Coriolis force at each grid point (using local wind direction and velocities). From the plots in Figure 5-9 it appears that the wind farm also affects this Coriolis term slightly compared to 'No farm' case. As illustrated in Figure 5-1 and Equation 5-1, this Coriolis term is acting in the opposite direction to the farm's streamwise direction. It should be noted, however, that this term is affected by the strength of mixing inside the CV since the mixing affects the local flow angle θ (measured from the streamwise direction). Therefore, to assess this Coriolis term more accurately, we would need a more sophisticated representation of the wind farm in the NWP model, such as the one proposed in [140], giving a better prediction of the mixing within and above the wind farm.

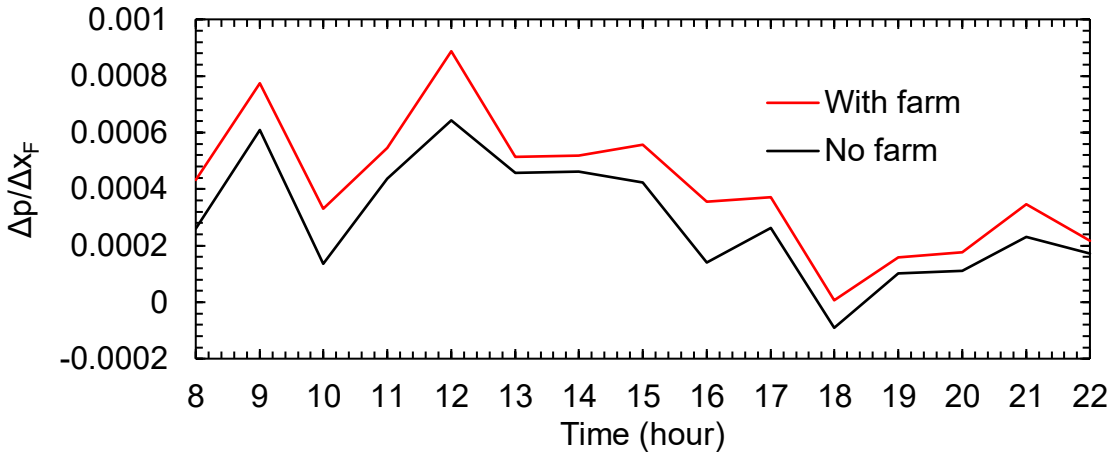

Figure 5-8 Comparison of the streamwise pressure gradient term. The additional pressure difference induced by the farm is apparent, and this effect is relatively consistent during the day.

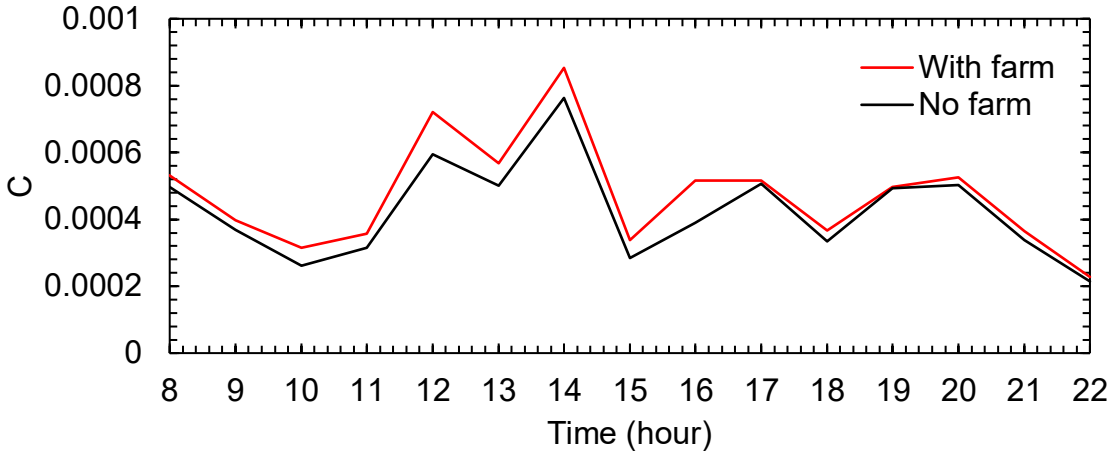

Figure 5-9 Comparison of the Coriolis term. The wind farm affects this Coriolis term slightly compared to 'No farm' case, this Coriolis term is acting in the opposite direction to the farm's streamwise direction.

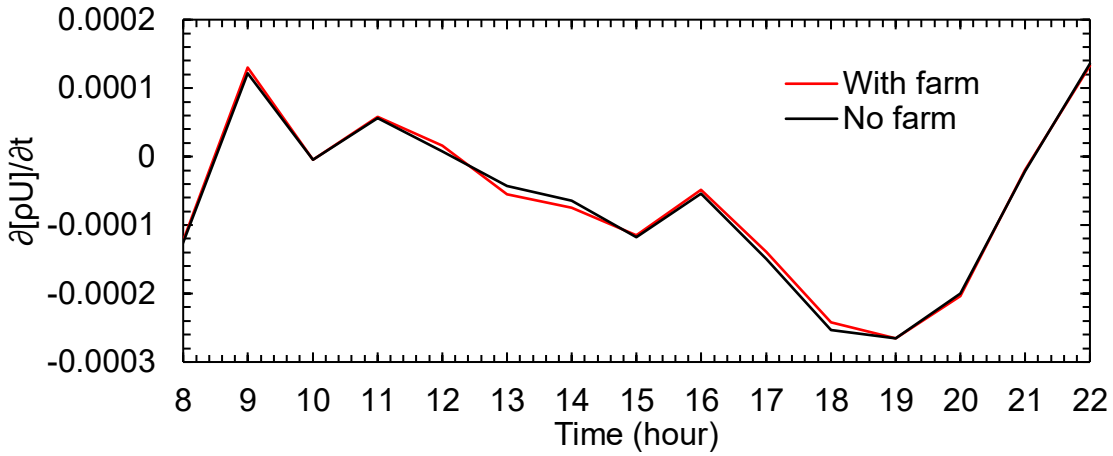

Figure 5-10 Comparison of the wind acceleration/deceleration term.

Finally, Figure 5-10 shows a comparison of the acceleration/deceleration term. It can be seen that the wind farm has almost no effect on the acceleration/deceleration term as the two plots in Figure 5-10 are almost identical. It should be noted, however, that this term depends substantially on the time interval of the NWP model output (which is 1 hour in this study). A further investigation into the sensitivity of this term to the time step size is required in a future study.

5.5 Conclusions

In this chapter we have presented some initial results of numerical analysis on the momentum balance over a large offshore wind farm, following the two-scale momentum theory proposed recently by Nishino and Dunstan [102]. This theory describes the basic relationship between the external (farm-scale) and internal (turbine-scale) flow problems based on the law of momentum conservation, but in the present study, only the external momentum balance has been considered. Specifically, we have employed a numerical weather prediction (NWP) model as a realistic flow model for the external problem to investigate how the three key terms in the farm-scale momentum equation (streamwise pressure gradient, Coriolis and acceleration/deceleration terms) tend to change in time.

Two NWP simulations have been performed for 24 hours of simulation time in parallel, i.e., under the same initial and boundary conditions except that one of the simulations had a simple wind farm model integrated in the domain. Our initial results support the existence of additional streamwise pressure gradient induced by the resistance caused by the wind farm, whereas the influence of the wind farm on the other two terms appears to be relatively minor. These results, once combined with turbine-scale flow models via the two-scale momentum theory, may help us better understand the mechanisms of the so-called wind farm blockage under realistic atmospheric conditions. However, further investigations and validation of these numerical results are required in future studies. In particular, it should be noted that the Coriolis term in the farm-scale streamwise momentum equation is affected by the strength of mixing inside and above the wind farm, meaning that a more sophisticated representation of the wind farm in the NWP model (than the roughness model used in this study) would be required to assess the characteristics of this term more accurately. The analysis should also be conducted for different types of weather conditions in future studies to assess their effects on the farm-scale momentum balance and thus the wind farm blockage.

6 Conclusions

6.1 Summary of Achievements

In this research, we have carried out a large offshore wind farm efficiency analysis, from the aerodynamics perspective. The wind turbine support structure has been mostly overlooked in previous wind energy studies; however, here we have established the significance turbine tower effects on the overall wind farm efficiency. In addition, interactions of ABL flow with a very large offshore wind farm has been investigated in this research. In particular, we have primarily focused on the relationship between the wind farm performance and three environmental parameters, namely the streamwise pressure gradient, Coriolis force and acceleration/deceleration. In order to make a meaningful contribution, a detailed literature survey was conducted in advance, which has been summarised in Chapter 2.

In Chapter 3, a modified version of the two-scale coupled momentum model has been established, that could be utilised to estimate the potential impacts of turbine support structure drag on the aerodynamic performance of large wind farms. The improved theoretical model indicates that as the wind farm density increases the support structure drag influence becomes more pronounced on the overall farm performance. In other words, the normalised support-structure drag should be taken into consideration when designing the optimal inter-turbine spacing. In addition, the finite-sized wind farm testing case was also included in this chapter, we found that the support-structure drag still played an important role regardless of the exact value of the environment dependent parameter ζ. Furthermore, for comparison purposes, a series of DES of a periodic fully staggered array of turbines has been conducted. The CFD results matched with the theoretical prediction relatively closely (maximum deviation is about 10%). However, actuator disc model has been adopted as a rough estimation of wind turbine, therefore, we shifted to a higher fidelity (fully resolved) turbine model in Chapter 4, in order to further validate the tower effect concept.

In Chapter 4, three wind farm CFD simulations have been demonstrated, which are Fully-resolved rotor + tower URANS, FR rotor only URANS and FR rotor + FR tower DDES. It is clear to see the flow velocity reduction (hence reduced wind farm efficiency) caused by the turbine tower, by comparing the URANS 'Tower' and 'No tower' cases. This also agrees with the theoretical model prediction. This is a strong evidence to confirm the significance of the support structure drag effect on wind farm performance. The FR turbine CFD results have shown larger deviations from the theoretical model results than the AD data showed in Chapter 3. The discrepancies are expected and understandable, since the theoretical model employs classical AD theory, and wake interactions as well as blockage effects are not considered in the theoretical model. Similar discrepancies were also observed in the previous study from Delafin [107]. On the other hand, the resolved turbine URANS simulation is a much higher fidelity model compared to theoretical and AD model, which is capable of representing more realistic wind farm flow conditions. Therefore, we could assume that the turbine tower effect might be even stronger in real life. The DDES data shown in this study is still in its early stage of development, however, valuable information has already been revealed in the current results. We were able to create a 3D overview of turbulent flows inside a wind farm, which is very close to real life scenarios. In particular, the hairpin vortex structures are clearly visible around the turbulence boundary layer. Moreover, we have found that the computational cost of running FR turbine in DDES is very similar to URANS (for a given number of rotations). This indicates that the DDES approach could be adopted more widely for future wind energy studies.

The environment dependent parameters which include streamwise pressure gradient, Coriolis forces and acceleration/deceleration of wind speed, are the other category of wind farm efficiency factors we have investigated in Chapter 5. This was a collaboration project with the UK Met Office, their state-of-the-art numerical weather prediction (NWP) model has been employed as a realistic atmospheric boundary layer flow model. In association with the newly proposed generalised two-scale momentum theory by Nishino and Dunstan [21] [102], the

NWP model is utilised to understand how the three environmental parameters in the farm-scale momentum equation tend to change in time. Under the same initial and boundary conditions, we have conduced two NWP simulations in parallel for 24 hours of simulation time. The only difference is that one of the simulations had a simple wind farm model integrated in the domain. The existence of additional streamwise pressure gradient, caused by the wind farm resistance, has been confirmed in our initial results. On the other hand, the added wind farm appeared to be less influential on the other two parameters. These simulated results if combined with the generalised two-scale momentum they, could help us better understand the wind farm blockage effects under realistic atmospheric flow conditions. However, since this a very new approach for wind energy study, these numerical results still require further investigation and validation, possible improvements and research directions are recommended later in this chapter.

6.2 Recommendations for future research

There are many valuable results have been obtained in the present study, however, there are still potential issues to be investigated in this research field. Some recommendations for possible future research are discussed below.

The bottom surface of all wind farm CFD simulations has been treated as ‘rough wall’ condition. The sea surface roughness is represented as a constant nominal ‘sand-grain’ type roughness height within the wall function embedded in FLUETN [44]. This assumption is valid if only calm sea surface was considered, but not for any other sea surface conditions such as large dynamic sea waves. Drennan, Taylor and Yelland (2005) [110] and Hersbach (2011) [141] have both separately reported that it is possible characterise sea surface roughness in relation to wind speed. It is possible to integrate bottom surface roughness height and drag coefficient as functions of wind flow velocity into CFD solvers in the future, therefore, a much more realistic sea surface condition could be modelled during simulations.

For simplification reason, we used the ‘porous-jump’ model (essentially the same as actuator disc model) to represent the turbine support structure in

Chapter 3. Since we are not comparing with any real wind turbine design, and only need to create additional drag in the flow field, this approach could be considered as appropriate in this case. However, it would require extensive validation if actual turbine support structure design was involved.

The Delayed Detached-Eddy simulation presented in Chapter 4 has not reached a statistically converged state. It is worth to extend the simulation for a long period of time, so that more valuable information could be extracted. Moreover, a mesh sensitivity analysis has not been conducted in this research, the mesh currently used is a relatively fine mesh with good accuracy level (according to the validation case presented in Chapter 4). However, a coarser mesh might also be suitable, in order to reduce computational costs. In addition, the relatively small domain size used for the DDES could be a limiting factor for capturing the correct large eddy structures. A domain size analysis would be a key research topic in the future.

We have found that the Coriolis force is affected by the strength of mixing inside and above the wind farm, which indicates that a more complex wind farm representation (instead of the roughness model in this study) would be required in the NWP model. It would also be interesting to conduct NWP simulations under different types of weather and seasonal conditions in the future to assess their effects on the farm-scale momentum balance and hence the wind farm blockage.

Last but not the least, during this research, there has not been any relatable experimental results from wind tunnels or measured data from real wind farms that is readily available to us. This is primarily because that this study is focused on fully developed wind farm flows, i.e., very large wind farm scenarios. Most of the large offshore wind farms are only recently built or still under construction, therefore, their measurements are not publicly available, or no measurements have been done yet. As for wind tunnel testing, the type of experiment required for this study would be very expensive to setup. It is essential to further validate the numerical wind farm models and results presented in this study, if

measurements data or experimental resources should become available in the future.

References

[1] B. Soren, “A history of renewable energy technology,” *Energy Policy,* vol. 19, no. 1, pp. 8-12, 1991.

[2] G. Agricola, “De re metallica,” *Dover Publications Inc.,* 1556.

[3] J. K. Kaldellis and D. Zafirakis, “The wind energy (r)evolution: A short review of a long history,” *Renewable Energy,* vol. 36, no. 7, pp. 1887-1901, 2011.

[4] Danish Wind Industry Association, “A Wind Energy Pioneer: Charles F. Brush,” 2003.

[5] V. J. Kurian, S. P. Narayanan and C. Ganapathy, “Towers for Offshore Wind Turbines,” in *The 10th Asian International Conference on Fluid Machinery* , Kuala Lumpur, 2010.

[6] M. D. Esteban, J. J. Diez, J. S. López and V. Negro, “Why offshore wind energy?,” *Renewable Energy,* vol. 32, no. 2, pp. 444-450, 2011.

[7] International Renewable Energy Agency, “RENEWABLE CAPACITY STATISTICS 2021,” International Renewable Energy Agency (IRENA), 2021.

[8] WindEurope, “Offshore Wind in Europe Key trends and statistics 2019,” WindEurope, 2020.

[9] Siemens Gamesa Renewable Energy, S.A., “Siemens Gamesa Renewable Energy, S.A.,” 2021. [Online]. Available: https://www.siemensgamesa.com/en-int/-/media/siemensgamesa/downloads/en/products-and-services/offshore/brochures/siemens-gamesa-offshore-wind-turbine-brouchure-sg-14-222-dd.pdf. [Accessed 21 07 2021].

[10] GE Renewable Energy, “GE Renewable Energy,” 2021. [Online]. Available: https://www.ge.com/renewableenergy/wind-energy/offshore-wind/haliade-x-offshore-turbine. [Accessed 21 07 2021].

[11] Vestas, “Vestas,” 2021. [Online]. Available: https://www.vestas.com/en/products/offshore%20platforms/v236_15_mw. [Accessed 21 07 2021].

[12] MingYang Smart Energy, “MingYang Smart Energy,” 20 8 2021. [Online]. Available: http://www.myse.com.cn/en/jtxw/info.aspx?itemid=825. [Accessed 21 8 2021].

[13] Ørsted, “Hornsea Projects,” 2021. [Online]. Available: https://hornseaprojects.co.uk/. [Accessed 21 7 2021].

[14] Dogger Bank WInd Farm, “Dogger Bank WInd Farm,” 2021. [Online]. Available: https://doggerbank.com/. [Accessed 21 7 2021].

[15] WindEurope, “Offshore Wind in Europe Key trends and statistics 2017,” WindEurope, 2018.

[16] O. Zolina and S. K. Gulev, “Synoptic Variability of Ocean–Atmosphere Turbulent Fluxes Associated with Atmospheric Cyclones,” *Journal of Climate,* vol. 16, no. 16, p. 2717–2734, 2003.

[17] F. Porté-Agel, M. Bastankhah and S. Shamsoddin, “Wind-Turbine andWind-Farm Flows: A Review,” *Bound.-Layer Meteorol.,* vol. 174, no. 1, pp. 1-59, 2020.

[18] F. W. Lanchester, “Contribution to the theory of propulsion and the screw propeller,” *Transactions of the Institution of Naval Architects,* vol. LVII, pp. 98-116, 1915.

[19] A. Betz, “Der Maximum der theoretisch mölichen Ausnützung des Windes durch Windmotoren,” *Zeitschrift für das Gesamte Turbinenwesen,* vol. 26,

pp. 307-309, 1920.

[20] H. Glauert, “Airplane propellers,” in *Aerodynamic Theory*, Berlin, Springer, 1935, p. 169–360.

[21] T. Nishino, “Generalisation of the two-scale momentum theory for coupled wind turbine/farm optimisation,” in *25th National Symposium on Wind Engineering*, Tokyo, Japan, December 2018, https://doi.org/10.14887/kazekosymp.25.0 , 97.

[22] T. Nishino, “Two-scale momentum theory for very large wind farms,” *Journal of Physics: Conference Series,* vol. 753, 2016.

[23] K. H. Bergey, “The Lanchester-Betz limit,” *J. ENERGY,* vol. 31, no. 6, pp. 382-384, 1979.

[24] C. Garrett and P. Cummins, “The efficiency of a turbine in a tidal channel,” *J. Fluid Mech.,* vol. 588, pp. 243-251, 2007.

[25] S. Antheaume, T. Maître and J.-L. Achard, “Hydraulic Darrieus turbines efficiency for free fluid flow conditions versus power farms conditions,” *Renewable Energy,* vol. 33, no. 10, pp. 2186-2198, 2008.

[26] T. Nishino and R. H. J. Willden, “Effects of 3-D channel blockage and turbulent wake mixing on the limit of power extraction by tidal turbines,” *Int. J. Heat Fluid Flow,* vol. 37, pp. 123-135, 2012.

[27] T. Nishino and R. H. J. Willden, “The efficiency of an array of tidal turbines partially blocking a wide channel,” *J. Fluid Mech.,* vol. 708, pp. 596-606, 2012.

[28] S. Frandsen, R. Barthelmie, S. Pryor, O. Rathmann, S. Larsen, J. Højstrup and M. Thøgersen, “Analytical modelling of wind speed deficit in large offshore wind farms,” *Wind Energy,* vol. 9, no. 1-2, pp. 39-53, 11 January 2006.

[29] M. Calaf, C. Meneveau and J. Meyers, “Large eddy simulation study of fully developed wind-turbine array boundary layers,” *Physics of Fluids,* vol. 22, no. 1, p. 015110, 2010.

[30] C. Meneveau, “The top-down model of wind farm boundary layers and its applications,” *Journal of Turbulence,* vol. 13, no. 7, 12 1 2012.

[31] I. Newton, Philosophiæ Naturalis Principia Mathematica, London, 1687.

[32] F. White and J. Majdalani, Viscous Fluid Flow (4th ed.), New York: McGraw-Hill Mechanical Engineering, 2021.

[33] G. G. Stokes, “On the effect of the internal friction of fluids on the motion of pendulums,” *Trans. Cambridge Phil. Soc.,* vol. 9, p. 8–106, 1851.

[34] J. D. Anderson, Computational Fluid Dynamics: The Basics with Applications, New York: McGraw-Hill Inc., 1995.

[35] O. Reynolds, “IV. On the dynamical theory of incompressible viscous fluids and the determination of the criterion,” *Philos. Trans. Royal Soc. A,* vol. 186, pp. 123-164, 1985.

[36] P. Kundu, I. Cohen and D. Dowling, Fluid Mechanics (6th ed.), London: Elsevier Science, 2015.

[37] P. R. Spalart and S. R. Allmaras, “A ONE-EQUATION TURBULENCE MODEL FOR AERODYNAMIC FLOWS,” AIAA 30th Aerospace sciences meeting and exhibit, Reno, 1992.

[38] D. C. Wilcox, Turbulence Modeling for CFD (3rd ed.), La Cañada: DCW Industries, Inc., 2006.

[39] A. Mittal, K. Sreenivas, L. K. Taylor, L. Hereth and C. B. Hilbert, “Blade-resolved simulations of a model wind turbi ne:effect of temporal convergence,” *Wind Energ,* vol. 19, p. 1761–1783, 2016.

[40] B. E. Launder and D. B. Spalding, Lectures in Mathematical Models of Turbulence, London: Academic Press, 1972.

[41] B. E. Launder and D. B. Spalding, “The Numerical Computation of Turbulent Flows,” *Comput. Methods Appl. Mech. Eng.,* vol. 3, no. 2, p. 269–289, 1974.

[42] D. C. Wilcox, “Reassessment of the Scale-Determining Equation for Advanced Turbulence Models,” *AIAA Journal,* vol. 26, no. 11, pp. 1299-1310, 1988.

[43] D. C. Wilcox, “Formulation of the k-omega Turbulence Model Revisited,” *AIAA Journal,* vol. 46, no. 11, pp. 2823-2838, 2008.

[44] ANSYS Inc., “ANSYS Fluent User’s Guide Release 17.2,” 2016.

[45] T. H. Shih, W. W. Liou, A. Shabbir, Z. Yang and J. Zhu, “A New - Eddy-Viscosity Model for High Reynolds Number Turbulent Flows - Model Development and Validation,” *Computers Fluids,* vol. 24, no. 3, pp. 227-238, 1995.

[46] F. R. Menter, “Zonal Two Equation k-ω Turbulence Models for Aerodynamic Flows,” in *23rd Fluid Dynamics, Plasmadynamics, and Lasers Conference*, Orlando, 1993.

[47] F. R. Menter, “Two-Equation Eddy-Viscosity Turbulence Models for Engineering Applications,” *AIAA Journal,* vol. 32, no. 8, pp. 1598-1605, 1994.

[48] S.-H. Peng and P. Eliasson, “Examination of the Shear Stress Transport Assumption with a Low-Reynolds Number k − ω Model for Aerodynamic Flows,” in *37th AIAA Fluid Dynamics Conference and Exhibit*, Miami, 2007.

[49] S. Rodriguez, Applied Computational Fluid Dynamics and Turbulence

Modeling, Cham: Springer, 2019.

[50] N. Sørensen and M. Hansen, “ROTOR PERFORMANCE PREDICTIONS USING A NAVIER-STOKES METHOD,” *AIAA-98-0025,* pp. 52-59, 1998.

[51] B. Dose, H. Rahimi, I. Herráez, B. Stoevesandt and J. Peinke, “Fluid-structure coupled computations of the NREL 5 MW wind turbine by means of CFD,” *Renewable Energy,* vol. 129, pp. 591-605, 2018.

[52] J. Jonkman, S. Butterfield, W. Musial and G. Scoot, “Definition of a 5-MW Reference Wind Turbine for Offshore System Development,” *Technical Report,* Vols. NREL/TP-500-38060, 2009.

[53] J. Boussinesq, “Théorie des ondes et des remous qui se propagent le long d’un canal rectangulaire horizontal, en communiquant au liquide contenu dans ce canal des vitesses sensiblement pareilles de la surface au fond,” *J. Mathématiques Pures et Appliquées. Deuxième Série ,* vol. 17, pp. 55-108, 1872.

[54] J. T. Kirby, “Boussinesq models and applications to nearshore wave propagation, surfzone processes and wave-induced currents,” *Elsevier Oceanography Series,* vol. 67, pp. 1-41, 2003.

[55] S. B. Pope, Turbulent Flows, Cambridge: Cambridge Univ. Press, 2000.

[56] Z. Yang, “Large-eddy simulation: Past, present and the future,” *Chinese J. Aeronaut.,* vol. 28, no. 1, pp. 11-24, 2015.

[57] P. Sagaut, Large Eddy Simulation for Incompressible Flows: An Introduction (3rd ed.), Berlin: Springer-Verlag Berlin Heidelberg, 2006.

[58] J. Smagorinsky , “General circulation experiments with the primitive equations I. the basic experiment,” *Mon. Weather Rev.,* vol. 91, no. 3, pp. 99-164, 1963.

[59] F. Nicoud and F. Ducros, “Subgrid-Scale Stress Modelling Based on the

Square of the Velocity Gradient Tensor.Flow," *Flow Turbul. Combust.,* vol. 62, no. 3, pp. 183-200, 1999.

[60] M. L. Shur, P. R. Spalart, M. K. Strelets and A. K. Travin, "A Hybrid RANS-LES Approach With Delayed-DES and Wall-Modelled LES Capabilities," *Int. J. Heat Fluid Flow,* vol. 29, no. 6, pp. 1638-1649, 2008.

[61] P. R. Spalart, W. H. Jou, M. K. Strelets and S. R. Allmaras, "Comments on the feasibility of LES for wings and on a hybrid RANS/LES approach," *Advances in DNS/LES,* vol. 1, no. JANUARY, pp. 4-8, 1997.

[62] P. R. Spalart, S. Deck, M. L. Shur, K. D. Squires, M. K. Strelets and A. Travin, "A new version of detached-eddy simulation, resistant to ambiguous grid densities," *Theoretical and Computational Fluid Dynamics,* vol. 20, no. 3, pp. 181-195, 2006.

[63] Rankine, W. J. M., "On the Mechanical Principles of the Action of Propellers," *Trans. Inst. Naval Architects,* vol. 6, pp. 13-39, 1865.

[64] R. E. Froude, "On the part played in propulsion by differences of fluid pressure," *Trans. Inst. Naval Architects,* vol. 30, p. 390–405, 1889.

[65] T. Burton, N. Jenkins, D. Sharpe and E. Bossanyi, "Aerodynamics of Horizontal Axis Wind Turbines," in *Wind Energy Handbook (2nd ed.)*, JohnWiley & Sons,, 2011, p. 39–136.

[66] N. E. Joukowsky, "Vortex theory of screw propeller, I," *Trudy Otdeleniya Fizicheskikh Nauk. Obshchestva Lubitelei Estestvoznaniya,* vol. 16, no. 1, pp. 1-31, 1912.

[67] J. N. Sørensen and A. Myken, "Unsteady actuator disc model for horizontal axis wind turbines," *J. Wind Eng. Ind. Aerodyn.,* vol. 39, pp. 139-149, 1992.

[68] R. Griffiths and M. Woollard, "Performance of the optimal wind turbine," *Applied Energy,* vol. 4, no. 4, pp. 261-272, 1978.

[69] S. L. Dixon and C. A. Hall, Fluid Mechanics and Thermodynamics of Turbomachinery, Oxford: Butterworth-Heinemann, 2014.

[70] J. Strickland, “Darrieus turbine: a performance prediction model using multiple streamtubes,” Technical Report for Sandia Nat. Labs., New Mexico, 1975.

[71] I. PARASCHIVOIU, “Double-multiple streamtube model for studying vertical-axis wind turbines,” *Journal of Propulsion and Power,* vol. 4, no. 4, pp. 370-377, 1988.

[72] D. P. Coiro, A. De Marco, F. Nicolosi, S. Melone and F. Montella, “Dynamic Behaviour of the Patented Kobold Tidal Current Turbine: Numerical and Experimental Aspects,” *Acta Polytechnica,* vol. 45, no. 3, pp. 77-84, 2005.

[73] A. Shires, “Development and Evaluation of an Aerodynamic Model for a Novel Vertical Axis Wind Turbine Concept,” *Energies,* vol. 6, no. 5, pp. 2501-2520, 2013.

[74] D. Grogan, S. Leen, C. Kennedy and C. Ó Brádaigh, “Design of composite tidal turbine blades,” *Renewable Energy,* vol. 57, pp. 151-162, 2013.

[75] C. M. J. C. C. P. M. R. W. P. C. M. &. J. A. C. O. P. I Masters PhD, “A robust blade element momentum theory model for tidal stream turbines including tip and hub loss corrections,” *Journal of Marine Engineering & Technology,* vol. 10, no. 1, pp. 25-35, 2011.

[76] D. Vandenberghe and E. Dick, “A free vortex simulation method for the straight bladed vertical axis wind turbine,” *Journal of Wind Engineering and Industrial Aerodynamics,* vol. 26, no. 3, pp. 307-324, 1987.

[77] F. L. Ponta and P. M. Jacovkis, “A vortex model for Darrieus turbine using finite element techniques,” *Renewable Energy,* vol. 24, no. 1, pp. 1-18, 2001.

[78] J. C. Murray and M. Barone, “The Development of CACTUS, a Wind and Marine Turbine Performance Simulation Code,” in *49th AIAA Aerospace Sciences Meeting including the New Horizons Forum and Aerospace Exposition*, Oriando, 2011.

[79] N. Troldborg, F. Zahle, P.-E. Réthoré and N. N. Sørensen, “Comparison of wind turbine wake properties in non-sheared inflow predicted by different computational fluid dynamics rotor models,” *Wind Energy,* vol. 17, pp. 657-669, 2014.

[80] K. M. Almohammadi, D. B. Ingham, L. Ma and M. Pourkashan, “Computational fluid dynamics (CFD) mesh independency techniques for a straight blade vertical axis wind turbine,” *Energy,* vol. 58, pp. 483-493, 2013.

[81] F. Zahle and N. N. Sørensen, “On the influence of far-wake resolution on wind turbine flow simulations,” *J. Phys.: Conf Series,* vol. 75, p. 012042, 2007.

[82] Ørsted, “Hornsea Project One & Two Offshore Wind Farms,” 2018.

[83] M. J. Churchfield, S. Lee and P. J. Moriarty, “A large-eddy simulation of wind-plant aerodynamics,” in *50th AIAA Aerospace Sciences Meeting*, Nashvile, TN, USA, 9-12 January 2012.

[84] A. Creech, W.-G. Früh and E. Maguire, “Simulations of an Offshore Wind Farm Using Large-Eddy Simulation and a Torque-Controlled Actuator Disc Model,” *Surveys in Geophysics,* vol. 36, no. 3, pp. 427-481, 2015.

[85] T. Chatterjee and J. Peet, “Exploring the benefits of vertically staggered wind farms: Understanding the power generation mechanisms of turbines operating at different scales,” *Wind Energy,* vol. 22, no. 2, pp. 283-301, 2019.

[86] M. Zhang, M. G. Arendshorst and R. J. A. M. Stevens, “Large eddy

simulations of the effect of vertical staggering in large wind farms," *Wind Energy,* vol. 22, no. 2, pp. 189-204, 2019.

[87] Y.-T. Wu and F. Porté-Agel, "Large-Eddy Simulation of Wind-Turbine Wakes: Evaluation of Turbine Parametrisations," *Boundary-Layer Meteorology,* vol. 138, no. 3, pp. 345-366, 2011.

[88] A. Mason-Jones, D. M. O'Doherty, C. E. Morris and T. O'Doherty, "Influence of a velocity profile & support structure on tidal stream turbine performance," *Renew. Energy,* vol. 52, pp. 23-30, 2013.

[89] P. Ouro, L. Ramírez and M. Harrold, "Analysis of array spacing on tidal stream turbine farm performance using Large-Eddy Simulation," *J. Fluids Struct.,* vol. 91, p. 102732, 2019.

[90] R. Vennell, "The energetics of large tidal turbine arrays," *Renew. Energy,* vol. 48, pp. 210-219, 2012.

[91] S. Muchala and R. H. J. Willden, "Impact of tidal turbine support structures on realizable turbine farm power," *Renew. Energy,* vol. 114, pp. 588-599, 2017.

[92] S. Frandsen, "On the wind speed reduction in the center of large clusters of wind turbines," *Journal of Wind Engineering and Industrial Aerodynamics,* vol. 39, no. 1-3, pp. 251-265, 1992.

[93] L. Ma and T. Nishino, "Preliminary estimate of the impact of support structures on the aerodynamic performance of very large wind farms," *J. Phys.: Conf. Ser.,* vol. 1037, no. 072036, 2018.

[94] T. Nishino and W. Hunter, "Tuning turbine rotor design for very large wind farms," *Proc. R. Soc. A,* vol. 474, no. 20180237, 2018, https://arxiv.org/abs/1803.03984.

[95] T. D. Dunstan, T. Muurai and T. Nishino, "Validation of a theoretical model for large turbine array performance under realistic atmospheric

conditions," in *AMS 23rd Symposium on Boundary Layers and Turbulence*, Oklahoma, OK, USA, 11-15 June 2018.

[96] A. Zapata, T. Nishino and P.-L. Delafin, "Theoretically optimal turbine resistance in very large wind farms," *Journal of Physics: Conference Series,* vol. 854, no. 012051, 2017.

[97] N. S. Ghaisas, A. S. Ghate and S. K. Lele, "Farm efficiency of large wind farms: evaluation using large eddy simulation," in *10th International Symposium on Turbulence and Shear Flow Phenomena*, Chicago, 2017.

[98] J. R. West and S. K. Lele, "Wind Turbine Performance in Very Large Wind Farms," in *71st Annual Meeting of the APS Division of Fluid Dynamics*, Atlanta, USA, 18-20 November 2018.

[99] T. Nishino and S. Draper, "Theoretical prediction of the efficiency of very large turbine arrays: combined effects of local blockage and wake mixing," in *7th Oxford Tidal Energy Workshop (OTE 2019)*, Oxford, UK, 8-9 April 2019.

[100] J. Bleeg, M. Purcell, R. Ruisi and E. Traiger, "Wind Farm Blockage and the Consequences of Neglecting Its Impact on Energy Production," *Energies,* vol. 11, no. 6, p. 1609, 2018.

[101] K. L. Wu and F. Porté-Agel, "Flow Adjustment Inside and Around Large Finite-Size Wind Farms," *Energies,* vol. 10, no. 12, p. 2164, 2017.

[102] T. Nishino and T. D. Dunstan, "Two-scale momentum theory for time-dependent modelling of large wind farms," *J. Fluid Mech.,* vol. 894, 2020.

[103] N. V. Nikitin, F. Nicoud, B. Wasistho and K. D. Squires, "An approach to wall modeling in large-eddy simulations," *Physics of Fluids,* vol. 12, no. 7, pp. 1629-1632, 2000.

[104] B. Blocken, T. Stathopoulos and J. Carmeliet, "CFD simulation of the atmospheric boundary layer: wall function problems," *Atmospheric*

Environment, vol. 41, no. 2, pp. 238-252, 2007.

[105] A. Zapata, “CFD STUDY ON THE EFFICIENCY OF A LARGE WIND FARM: EFFECT OF THE ARRAY LAYOUT AND GROUND ROUGHNESS,” Cranfield University, 2016.

[106] T. Nishino and S. Draper, “Local blockage effect for wind turbines,” *J. Phys.: Conf. Ser.,* vol. 625, pp. 1-10, 2015.

[107] P.-L. Delafin and T. Nishino, “Momentum balance in a fully developed boundary layer over a staggered array of NREL 5MW rotors,” *J. Phys.: Conf. Ser.,* vol. 854, pp. 0-10, 2017.

[108] C. Mockett and F. Thiele, “Progress in des for wall-modelled les of complex internal flows,” in *Computational Fluid Dynamics 2010 - Proceedings of the 6th International Conference on Computational Fluid Dynamics, ICCFD 2010*, 2011.

[109] J. Meyers and C. Meneveau, “Optimal turbine spacing in fully developed wind farm boundary layers,” *Wind Energy,* vol. 15, no. 2, pp. 305-217, 2012.

[110] W. M. Drennan, P. K. Taylor and M. J. Yelland, “Parameterizing the Sea Surface Roughness,” *Journal of Physical Oceanography,* vol. 35, no. 5, pp. 835-845, 2005.

[111] S. K. Kanev, F. J. Savenije and W. P. Engels, “Active wake control: An approach to optimize the lifetime operation of wind farms,” *Wind Energy,* vol. 21, no. 7, pp. 488-501, 2018.

[112] S. Bhattacharya, “Challenges in Design of Foundations for Offshore Wind Turbines,” *Engineering & Technology Reference,* 2014.

[113] D. J. Tritton, Physical fluid dynamics, 2nd ed., Oxford: Clarendon Press, 1988.

[114] T. Nishino and S. Draper, “Local blockage effect for wind turbines,” *J. Phys.: Conf. Ser.,* vol. 625, no. 012010, 2015.

[115] S. Naderi, S. Parvanehmasiha and F. Torabi, “Modeling of horizontal axis wind turbine wakes in Horns Rev offshore wind farm using an improved actuator disc model coupled with computational fluid dynamic,” *Energy Conversion and Management,* vol. 171, pp. 953-968, 2018.

[116] M. Richmond, A. Antoniadis, L. Wang, A. Kolios, S. Al-Sanad and J. Parol, “Evaluation of an offshore wind farm computational fluid dynamics model against operational site data,” *Ocean Engineering,* vol. 193, p. 106579, 2019.

[117] R. J. Stevens, L. A. Martínez-Tossas and C. Meneveau, “Comparison of wind farm large eddy simulations using actuator disk and actuator line models with wind tunnel experiments,” *Renewable Energy,* vol. 116, pp. 470-478, 2017.

[118] J. N. Sørensen, R. F. Mikkelsen, D. S. Henningson, S. Ivanell, S. Sarmast and S. J. Andersen, “Simulation of wind turbine wakes using the actuator line technique,” *Phil. Trans. R. Soc.,* vol. 373, no. 2035, 2015.

[119] S. Kalvig, E. Manger and B. Hjertager, “Comparing different CFD wind turbine modelling approaches with wind tunnel measurements,” *J. Phys.: Conf. Ser.,* vol. 555, p. 012056, 2014.

[120] M. H. A. Madsen, F. Zahle, N. N. Sørensen and J. R. R. A. Martins, “Multipoint high-fidelity CFD- based aerodynamic shape optimization of a 10 MW wind turbine,” *Wind Energ. Sci.,* vol. 4, no. 2, pp. 163-192, 2019.

[121] R. V. Rodrigues and C. Lengsfeld, “Development of a Computational System to Improve Wind Farm Layout, Part I: Model Validation and Near Wake Analysis,” *Energies,* vol. 12, no. 5, 2019.

[122] N. Stergiannis, C. Lacor, J. V. Beeck and R. Donnelly, “CFD modelling

approaches against single wind turbine wake measurements using RANS," *J. Phys.: Conf. Ser.,* vol. 753, p. 032062, 2016.

[123] T. Uchida, Y. Taniyama, Y. Fukatani, M. Nakano, Z. Bai, T. Yoshida and M. Inui, "A NewWind Turbine CFD Modeling Method Based on a Porous Disk Approach for Practical Wind Farm Design," *Energies,* vol. 13, no. 12, p. 3197, 2020.

[124] P. Weihing, C. Schulz, T. Lutz and E. Krämer, "Comparison of the Actuator Line Model with Fully Resolved Simulations in Complex Environmental Conditions," *J. Phys.: Conf. Ser.,* vol. 854, p. 012049, 2017.

[125] W. Miao, C. Li, G. Pavesi, J. Yang and X. Xie, "Investigation of wake characteristics of a yawed HAWT and its impactson the inline downstream wind turbine using unsteady CFD," *J. Wind. Eng. Ind. Aerodyn.,* vol. 168, pp. 60-71, 2017.

[126] J. M. Wilson, C. J. Davis, S. K. Venayagamoorthy and P. R. Heyliger, "Comparisons of Horizontal-Axis Wind Turbine Wake Interaction Models," *J. Sol. Energ. Eng.,* vol. 137, no. 3, p. 031001, 2015.

[127] F. Zahle, N. N. Sørensen and J. Johansen, "Wind Turbine Rotor-Tower Interaction Using an Incompressible Overset Grid Method," *Wind Energy,* vol. 12, no. 6, pp. 594-619, 2009.

[128] M. M. Hand, D. A. Simms, L. J. Fingersh, D. W. Jager, J. R. Cotrell, S. Schreck and S. M. Larwood, "Unsteady Aerodynamics Experiment Phase VI: Wind Tunnel Test Configurations and Available Data Campaigns," *Tech Rep,* Vols. NREL/TP-500-29955, 2001.

[129] B. Dose, H. Rahimi, B. Stoevesandt and J. Peinke, "Fluid-structure coupled investigations of the NREL 5 MW wind turbine for two downwind configurations," *Renewable Energy,* vol. 146, pp. 1113-1123, 2020.

[130] R. V. Rodrigues and C. Lengsfeld, “Development of a Computational System to Improve Wind Farm Layout, Part II: Wind Turbine Wakes Interaction,” *Energies,* vol. 12, no. 7, 2019.

[131] B. R. Resor, “Definition of a 5MW/61.5m wind turbine blade reference model,” *Tech Rep SAND2013-2569,* 2013.

[132] L. Ma, T. Nishino and A. Antoniadis, “Prediction of the impact of support structures on the aerodynamic performance of large wind farms,” *J. Renew. Sustain. Energy,* vol. 11, no. 6, 2019.

[133] D. Major, J. Palacios, M. Maufhumer and S. Schmitz, “A Numerical Model for the Analysis of Leading-Edge Protection Tapes for 465 Wind Turbine Blades,” *J. Phys.: Conf. Ser.,* p. 1452, 2020.

[134] G. Eitel-Amor, O. Flores and P. Schlatter, “Hairpin vortices in turbulent boundary layers,” *J. Phys.: Conf. Ser,* vol. 506, pp. 0-15, 2014.

[135] F. Viola, G. V. Iungo, S. Camarri, F. Porté-Agel and F. Gallaire, “Prediction of the hub vortex instability in a wind turbine wake: stability analysis with eddy-viscosity models calibrated on wind tunnel data,” *J. Fluid Mech,,* vol. 750, no. R1, 2014.

[136] R. Ashton, F. Viola, S. Camarri, F. Gallaire and G. V. Iungo, “Hub vortex instability within wind turbine wakes: Effects of wind turbulence, loading conditions, and blade aerodynamics,” *Phys. Rev. Fluids,* vol. 1, no. 7, 2016.

[137] E. Barlas, S. Buckingham and J. van Beeck, “Roughness effects on wind-turbinewake dynamics in a boundary- layer wind tunnel,” *Boundary-Layer Meteorol,* vol. 158, no. 1, pp. 27-42, 2016.

[138] N. Coudou, S. Buckingham and J. van Beeck, “Experimental study on the wind-turbine wake meandering inside a scale model wind farm placed in an atmospheric-boundary-layer wind tunnel,” *J. Phys.: Conf. Ser.,* vol.

854, no. 1, 2017.

[139] Walters et al., “The Met Office Unified Model Global Atmosphere 7.0/7.1 and JULES Global Land 7.0 configuration,” *Geosci. Model Dev.,* no. 12, pp. 1909-1963, 2019.

[140] M. Abkar and F. Porté-Agel, “A new wind-farm parameterization for large-scale atmospheric models,” *J. Renew. Sustain. Energy,* vol. 7, no. 1, p. 013121, 2015.

[141] H. Hersbach, “Sea Surface Roughness and Drag Coefficient as Functions of Neutral Wind Speed,” *J. Phys. Oceanogr.,* vol. 41, no. 1, pp. 247-251, 2011.